

CZECH TECHNICAL UNIVERSITY IN PRAGUE  
FACULTY OF NUCLEAR SCIENCES AND PHYSICAL ENGINEERING  
DEPARTMENT OF PHYSICAL ELECTRONICS



Development and applications of coherent XUV  
sources driven by ultrashort laser pulses

DOCTORAL THESIS

Krzysztof Jakubczak

Supervisor: Ladislav Píňa

Supervisor-specialist: Tomáš Mocek

Doctoral study program: Applications of Natural Sciences

Doctoral study subprogram: Physical Engineering

Prague, 12 August 2010



## Declaration

The thesis was worked out at the Department of Physical Electronics, Faculty of Nuclear Sciences and Physical Engineering of the Czech Technical University in Prague and at the Institute of Physics (IoP) and Prague Asterix Laser System (PALS) of the Academy of Sciences of the Czech Republic, from October 2006 to May 2010.

I hereby declare I have worked out the thesis independently while noting all the resources employed as well as co-authors. I consent to the publication of the thesis under Act No. 111/1998, Coll., on universities as amended by subsequent regulations.

Prague, August 12, 2010

Signature



## Acknowledgments

This work would never find its shape without constant help and guidance of my scientific supervisors: Doc. Ing. Ladislav Pína, DrSc and Ing. Tomáš Mocek, Ph.D. I would also like to address my gratitude for support and for being a great mentor to me to Ing. Bedřich Rus, Ph.D. and many other teachers I met during my whole education and who became examples for me to follow. Many thanks also to all team members and a visiting student who supported me either by their advices, experience, work in the laboratory or by help with processing experimental data. I would like to mention: Jan Hřebíček, Jiří Polan, Michaela Kozlová, Magdalena Sawicka, and Sikociński Paweł.

I would also like to thank all our collaborators who were eager to perform experiments in their laboratories. Special words of acknowledgments are expressed to prof. Chang Hee Nam and his students from Department of Physics and Coherent X-ray Research Center, KAIST, Korea, for experiments on two-color HHG and application experiments as well as to Dr. Stéphane Sebban from Laboratoire d'Optique Appliquée, France, for an experiment on amplification of harmonics.

In my acknowledgements I shall not forget about great administrative support from Mses. Radka Havlíková and Iva Ornová.

Finally, I would like to thank my wife Małgorzata for her constant support and patience especially during tiring experiments and for giving me strength to continue.

Special thanks are addressed to my parents for raising me and for their support (*pol. Szczególne podziękowania kieruję do swoich rodziców za trud wychowania i rodzicielskie wsparcie*).



**Title:** Development and applications of coherent XUV sources driven by ultrashort laser pulses

**Author:** Krzysztof Jakubczak, M.Sc.

**Department:** Department of Physical Electronics, Faculty of Nuclear Sciences and Physical Engineering, Czech Technical University in Prague

**Supervisor:** Doc. Ing. Ladislav Pína, DrSc.

**Supervisor-specialist:** Ing. Tomáš Mocek, Ph.D.

**Abstract:**

The dissertation is devoted to development and experimental implementation of 1-kHz, coherent extreme ultraviolet (XUV) radiation source based on high-order harmonic generation of the femtosecond near-infrared laser pulses generated by the titanium sapphire laser system (35 fs, 1.2 mJ, 810 nm) at the Institute of Physics AS CR, v.v.i./ PALS Centre. The source comprises a low-density gas cell filled with conversion medium, typically argon. Comprehensive optimization of the XUV harmonic source was performed with respect to major source parameters such as gas pressure in the gas cell, gas cell length, position of the focus of the driving laser field with respect to the gas cell position, size of the driving near-infrared laser beam, chirp of the femtosecond pulse and focal length of the lens deployed in the experimental setup. Harmonic spectra were recorded using a new XUV transmission grating spectrometer developed within this thesis. Detailed characterization of the XUV source has been performed including measurement of the XUV beam profile,  $M^2$  parameter of the harmonic beam, and spatial coherence of the harmonic beam. Energy of the XUV harmonic source was estimated. The XUV source was successfully utilized in application experiments on structuring and surface processing of various materials, multilayer XUV optics metrology, and absolute calibration of XUV-sensitive CMOS camera. Finally, results on development of strong harmonic source by means of two-color method, and amplification of harmonics in XUV plasma amplifier are presented.

**Keywords:**

High-order harmonic generation, gas cell, two-color high-order harmonic generation, high-order harmonics amplification, surface structuring, absolute calibration, multilayer optics metrology.



## Contents

Chapter 1. Preface .....	3
Chapter 2. Physical mechanisms of high-order harmonic generation .....	7
2.1 Background to nonlinear optics in the strong field regime .....	7
2.2 High-order harmonic generation in gaseous media .....	12
2.2.1 Microscopic analysis .....	12
2.2.2 Macroscopic analysis - phase-matching considerations .....	15
2.2.3 Generic properties of high-order harmonics spectrum .....	18
2.2.4 HHG geometries involving gaseous media .....	20
2.3 High-order Harmonic Generation by molecules .....	22
2.4 High-order Harmonic Generation from solid targets.....	24
Chapter 3. Development of HHG source at IoP/PALS .....	27
3.1 Laser system .....	27
3.2 Experimental infrastructure .....	29
3.3 Diagnostic methods and techniques.....	31
Chapter 4. HHG source characterization .....	35
4.1 Optimization of the source parameters.....	35
4.1.1 Chirp of the NIR femtosecond laser pulse.....	35
4.1.2 Size of the NIR driving beam.....	48
4.1.3 Focal length of the lens .....	54
4.1.4 Gas cell length.....	55
4.1.5 Gas pressure .....	57
4.1.6 Cell position .....	62
4.2 HHG beam profile.....	69
4.3 $M^2$ of HHG beam .....	72

---

4.4	HHG beam spatial coherence.....	81
4.5	Estimation of absolute HHG signal.....	85
Chapter 5.	Applications of HHG source .....	87
5.1	Materials surface processing .....	87
5.2	Multilayer optics metrology .....	95
5.3	Absolute calibration of XUV-sensitive CMOS camera.....	98
Chapter 6.	Development of advanced XUV sources based on HHG .....	101
6.1	Two-color HHG .....	101
6.2	Amplification of high-order harmonics in OFI laser amplifier .....	108
Chapter 7.	Conclusion .....	113
Chapter 8.	References .....	117
Chapter 9.	Index.....	127
Chapter 10.	List of figures.....	129
Chapter 11.	List of graphs.....	135
Chapter 12.	List of tables .....	139

## Chapter 1. Preface

The discovery of X-rays by Wilhelm Conrad Röntgen in 1895 [1] has been one of the most important driving forces to push forward understanding and knowledge in all kinds of scientific areas. Their applications range from structure analysis in solid-state as well as atomic physics and molecular chemistry via imaging applications in medicine and life sciences to the discovery of the basic building blocks of life, in particular the DNA, and more generally, the structure of proteins and other macromolecules. Having an access to the spatial resolution of molecular structure and electron orbitals is; however, only one side of the coin to be explored by X-rays. It took about one century to flip the coin to the other side showing the temporal resolution of the atomic and molecular motion, making it possible to monitor the dynamics of molecules and electrons on their natural time scale, which is in the femtosecond to even attosecond range. However, early X-ray generation devices and techniques such as X-ray tubes, electrical discharges or the first synchrotron sources have not been able to deliver X-ray pulses that had duration of less than several nanoseconds and thus could not be used to gather both types of information: spatial and temporal simultaneously. An insight into temporal dynamics of quantum systems was first gained by using probes of much larger wavelength than the one of X-rays: infrared (IR), visible (VIS) and ultraviolet laser (UV) pulses. Today, the fundamental limit of ultrashort laser pulses is one single optical cycle, lasting about 1 femtosecond ( $1 \text{ fs} = 10^{-15} \text{ s}$ ) in the near UV to several femtoseconds in the IR spectral region [3], [4]. Even though lasers provide the possibility of monitoring molecular and electronic motion, they are not able to directly image molecular structure at atomic resolution due to the large wavelength of the emitted radiation. The solution to this problem is to combine X-rays and lasers to take advantage of both short wavelength and coherence properties to create ultrashort pulses of X-ray radiation.



Figure 1.1. Ms. Röntgen's hand. First medical imaging with X-rays (December 22 1895) [2].

One possibility of how to obtain ultrashort bursts of coherent extreme ultraviolet (abbreviated XUV or EUV; wavelength spectral range between 10-100 nm), soft X-ray (1-10 nm) and/or X-ray radiation (< 1 nm) is by High-order Harmonic Generation (HHG) process. It involves the interaction of laser light at a given frequency during which it is being converted into integer multiples of this fundamental frequency through a highly nonlinear interaction with a conversion medium (typically a noble gas) [5]. The laser-driven HHG uses acceleration of electrons on time-scales that are of the order of an optical cycle of the laser field. Currently this technique gives rise to the shortest flashes of light ever generated in a laboratory which are of the order of a few hundreds of attoseconds (1 as =  $10^{-18}$  s) [6]-[8]. When laser field of intensity of about  $10^{14}$  -  $10^{15}$  W/cm<sup>2</sup> is applied to the gas, a plateau of equally intense harmonics of very high order can be observed. In fact, the atom is ionized when the absolute electric field of the laser is close to its crest during an optical cycle and is pulled away from the parent ion. Since the laser electric field changes its sign about a quarter of a period later, the electron will slow down, stop at a position far from the ion and start to accelerate back towards it [10]. When it returns to the ion, it can possess a significant amount of kinetic energy, much larger than the photon energy but being its multiple. This energy plus the ionization potential is transferred into photon energy as soon as the electron recombines with its parent ion, which gives rise to very high harmonic orders observed in experiments [11]. Thus HHG represents a practical source of coherent X-rays bursts of ultrashort time duration. Additionally, the HHG source features spectral tunability from UV to hard X-rays. Moreover, advantage of particular importance is a very high



Figure 1.2. Typical spectrum of high-order harmonic XUV source developed at IoP/PALS (conversion medium: argon).

repetition rate of HHG which is given by the repetition rate of the driving laser only and can be easily as much as few kHz [8] up to MHz!

It has been shown that high-order harmonic pulse comprises train of attosecond pulses [12]. As a great advantage this constituted a stimulus for further development of high-order harmonic sources, especially of the techniques leading to generation of single attosecond pulses. Nowadays, well explored and most frequently deployed are:

- usage of very short IR laser pulses ( $< 5$  fs) [13]-[14],
- a technique called *polarization gating* [15].

The details of the afore mentioned techniques will not be discussed in detail here; however, it is worth noting that the intension of improvement of high-order harmonic sources has become a boost for laser technology progress leading to development of laser systems emitting laser pulses with duration in the range of single optical cycle ( $\sim 3.3$  fs at  $\sim 810$  nm central wavelength) and shifting the laser pulse central wavelength to the mid-infrared spectral range (MIR) in around  $2\text{-}3\ \mu\text{m}$ . Besides, the lasers repetition rates have been significantly increased to few kHz (and energy  $\sim$ mJ per pulse; e.g. [8]). Another recent achievement of particular interest is carrier-envelope absolute phase stabilization (CEP).

State-of-the-art HHG sources require not only development of the high-harmonic source itself but also sophisticated metrology techniques and methods for measurements of femtosecond and attosecond XUV/X-ray pulses [16]-[21].

Due to unusual combination of all properties that high-order harmonics possess they immediately found vast number of unprecedented applications. For example, a number of experimental results have been recently published related to time-resolved investigation of atomic processes. For example manipulation of drift energy of photoelectron wave packets (so called "steering of wave packets") and imaging of electron wave packets (e.g. [22]), measurement of relaxation and lifetime dynamics in an atom by the direct measurement in time domain with attosecond resolution (e.g. [14], [18]; in contrary to thus far frequency-domain measurements of transition

linewidths [23]), spectroscopy of bound electron dynamics in atoms and molecules [24], observation of interference of coherent electron wave packets [25], probing molecular dynamics [26] and real-time tomography of molecular orbitals [27].

Moreover, novel and very promising schemes for HHG have been recently demonstrated, e.g., generation of harmonics during reflection of super intense ultrashort IR laser pulses ( $I > 10^{17}$  W/cm<sup>2</sup>) from plasma mirror oscillating at relativistic velocities on the surface of a solid state target [28], or generation of HHG from interaction of IR femtosecond laser pulses with molecules (N<sub>2</sub>, H<sup>2+</sup>) [29].

The first objective of the doctoral thesis was to build, optimize and characterize the high-order harmonic source based on interaction of near-infrared femtosecond laser pulses with a conversion medium contained in a gas cell. The results on the source implementation, optimization and characterization are presented in Chapter 3 and Chapter 4 after comprehensive discussion in Chapter 2 on the physical mechanisms involved in the process of high-order harmonic generation as well as the possible experimental arrangements of this type of source of coherent XUV radiation.

Secondly, the thesis covers the first applications of the HHG sources (Chapter 5). The source was successfully applied to structuring of the surface of the materials, multilayer X-ray optics metrology and absolute calibration of XUV-sensitive CMOS camera.

Finally, further development of harmonic sources by means of two-color scheme as well as by amplification of harmonics in laser plasma amplifiers is discussed and the relevant experimental results are presented in Chapter 6.

## Chapter 2. Physical mechanisms of high-order harmonic generation

### 2.1 Background to nonlinear optics in the strong field regime

When material is subjected to a strong electric field nonlinear polarization of the material is induced. The magnitude of the arisen polarization strongly depends on the intensity of the incident radiation. At moderate and low intensity values the external electric field does not influence significantly the electronic structure of the irradiated atoms. The potential barriers can be just slightly modified and Stark effect can be observed. To great probability the atoms remain in its ground state and extension of their ground state wave function is of the order of Bohr radius ( $5.2917 \cdot 10^{-11}$  m). All nonlinear phenomena taking place in this regime are well described by the perturbation theory. Thus it is referred as *the perturbative regime* of nonlinear optics. Comprehensive discussion on phenomena and related theory in the perturbative regime can be found e.g. in Ref. [30]. Some of nonlinear optical phenomena in this regime are:

- harmonics generation (second, third, etc.),
- optical parametric amplification,
- optical rectification,
- stimulated Raman scattering,
- self-phase modulation,
- self-focusing.

However, when the electric field strength of the incident radiation is comparable to (or higher than) atomic electric field strength ( $5.142 \cdot 10^{11}$  V/m [5]), the potential barriers are strongly modified. With high probability the electrons from the most-outer atomic shells may be liberated either through the tunnel ionization or the above barrier ionization (depending on the external field strength; see Figure 2.1 and Figure 2.2). Subsequently, if the field is linearly polarized electron wave packets will start oscillatory

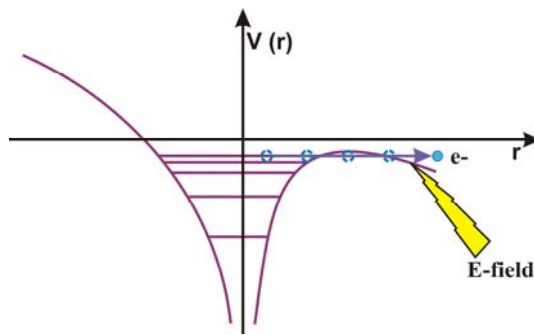


Figure 2.1. Tunnel ionization. The atomic potential affected by the external electric field which the field strength is comparable to the atomic fields. It is plausible that the electrons from the most-outer atomic shell will be unbound. This transition is often referred as Optical Field Ionization (OFI).

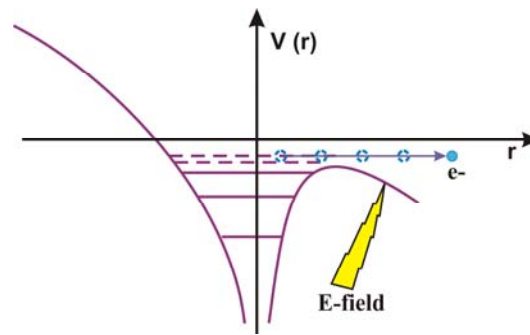


Figure 2.2. In this case, the applied electric field is even higher than the atomic field strength. The atomic potential barrier is suppressed and electrons from most-outer shells are liberated through above barrier ionization.

motion. The amplitude of oscillations exceeds Bohr radius and cycle-averaged kinetic energy of electron wave packet surpasses binding energy [5].

Range of intensities implying these phenomena defines *the strong field nonlinear optics regime*. In contrary to the perturbative regime, here, the nonlinear response of the polarization of the medium is affected by the ionization process. The nonlinear treatment can be only applied to an electron which is in very close vicinity of a parent ion. As soon as it is released by optical field, its respond is linear to the electric field and may be treated by classical laws of motion [9]-[10].

Very interesting phenomena are present in the intermediate range of parameters, in the so called *intermediate regime*, i.e. between the perturbative and the strong field regimes. They include long-distance self-channeling when nonlinear Kerr effect causes beam focusing, on the one hand, and free electrons cause its defocusing, on the other. This interplay leads to the channeling of the propagating intense pulse (even at distances as long as a few meters).

Another interesting phenomenon in this regime is multiphoton ionization, where the total amount of absorbed energy exceeds the ionization potential (Figure 2.3).

When electric field strengths are even higher the nonlinearities become stronger. Electric field is able to optically liberate electrons from inner shells of the atom and the

wiggling energy of an electron is comparable with its rest energy  $mc^2$ . This is a launch of *relativistic regime*.

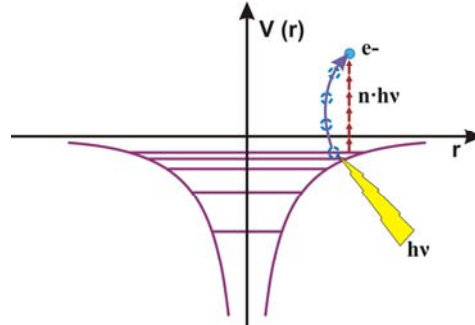


Figure 2.3. Multiphoton ionization process:  $n$ -photons is absorbed. The total energy of absorbed photons ( $n \cdot h\nu$ ;  $n$  - number of absorbed photons,  $h$  - Planck's constant,  $\nu$  - light frequency) exceeds ionization potential.

Publications of crucial importance related to the intermediate to strong-field nonlinear optics regimes were made by Keldysh [31] and Ammonsov, Delone and Krainov [32]. Keldysh defined a parameter, named later after him, which allows to determine whether tunneling or multiphoton process is dominant for particular experimental conditions. It reads:

$$\gamma = \sqrt{\frac{I_p}{2 \cdot U_p}}$$

Eq. 2.1

Where:

$I_p$  - is ionization potential of a nonlinear medium,

$U_p$  - is ponderomotive potential, which is cycle-averaged quivering energy of an electron in the external laser field. It is defined as:

$$U_p = \frac{e^2 \cdot E_0^2}{4m_e \cdot \omega^2}$$

Eq. 2.2

Where:

$e$  - stands for charge of electron,

$m_e$  - is mass of electron,

$E_0$  - external field amplitude oscillating at frequency  $\omega$ .

Substitution of the constants leads to simplified relation:

$$U_p [eV] = 0.97 \cdot 10^{-13} I [W/cm^2] \lambda^2 [\mu m]$$

Eq. 2.3

The laser field amplitude can be estimated from relation:

$$E_0^2 [V/cm] = \frac{I [W/cm^2]}{\frac{1}{2} Z_0}$$

Eq. 2.4

Where:

$I$  - is laser intensity [ $V/cm^2$ ],

$Z_0$  - is vacuum impedance.

$$Z_0 = \sqrt{\mu_0 \varepsilon_0} = 377 [V/A]$$

Eq. 2.5

Where:

$\mu_0$  - is vacuum permeability,  $\mu_0 = 1.26 \cdot 10^{-6}$  [H/m] ,

$\varepsilon_0$  - is vacuum permittivity,  $\varepsilon_0 = 8.85 \cdot 10^{-12}$  [F/m] .

If  $\gamma \gg 1$ , multiphoton ionization dominates. However, if  $\gamma \ll 1$ , tunneling ionization takes over. By these simple formulas it is possible to divide regimes of nonlinear optics in intensity domain as depicted in the Figure 2.4.

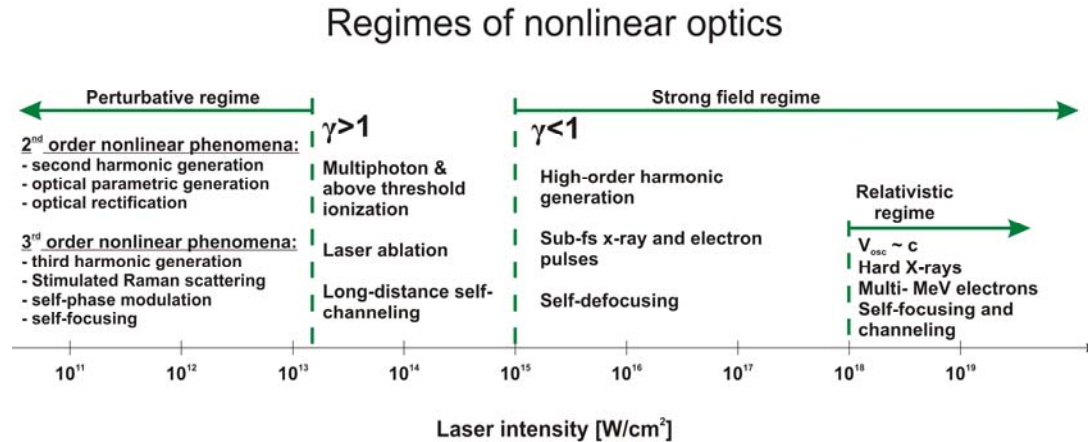


Figure 2.4. Regimes of nonlinear optics.

Of core importance in the interaction of intense laser pulses with matter is the possibility of estimation of ionization rates. This was done within quastistic field approximation. The first approach was proposed by Keldysh. The second was developed by Ammonsov, Delone and Krainov (also known as ADK theory named after the acronyms of the names). Additionally, the ionization rate calculation could be performed by an exact numerical solution of the time-dependent Schrödinger equation. The Keldysh theory possesses a source of a discrepancy between the other theories which comes from the fact that it neglects Coulomb potential in an atom. The difference leads to lower ionization rates compared to other approaches (e.g. in case of He and H by about 1-2 orders of magnitude) [5]. The discrepancies between theories increase with the electric field strength. For example, for He there is no difference between ionization rates obtained from ADK theory and solution of the time-dependent Schrödinger equation as long as the field strength does not exceed 0.2 atomic unit.

## 2.2 High-order harmonic generation in gaseous media

### 2.2.1 Microscopic analysis

As mentioned in Chapter 1, the high-order harmonic generation process takes place when linearly polarized ultrashort laser pulses of intensity of a few times  $10^{13} \text{ W/cm}^2$  to  $< 10^{16} \text{ W/cm}^2$ , and time duration from picoseconds to a few femtoseconds [33], are applied to a nonlinear medium (atoms, atom clusters, molecules and plasmas).

HHG process can be understood using semi-classical *three-step model* [10]:

**Step I - Ionization.** When an atom is exposed to external electric field the potential of the atom is modified by a factor of  $e \vec{E}(t) \vec{r}$ . Then, the resulting potential is equal to:

$$V(\vec{r}, t) = -\frac{e^2}{4\pi\epsilon_0 r} + e \vec{E}(t) \vec{r}$$

Eq. 2.6

With increasing strength of the external field  $\vec{E}(t)$  the probability of tunnel-ionization by the low-frequency laser field of most-outer-shell electrons increases significantly (the natural potential of atom is being cancelled).

**Step II - Propagation.** When an electron wave function undergoes tunnel-ionization from its parent atom the free electron wave packet is affected primarily by the external electric field (and not by the field of the parent atom) and is accelerated by this field. When the laser field reverses its sign the electrons slow down and are re-accelerated back towards the atom. The free electron motion can be described by laws of classical physics [33]:

$$v(t) = \int_0^t -\frac{e}{m} E(t') dt' + v_0 = -\frac{E_0 e}{m\omega} \sin(\omega t) + v_0$$

Eq. 2.7

where:  $v(t)$  - is instant velocity of an electron,  $v_0$  - is electron drift velocity.

If we consider an initially bound electron ( $x=0$ ), with zero drift velocity, its velocity can be described by [33]:

$$v(t) = \int_0^t -\frac{e}{m} E(t') dt' + v_0 = -\frac{E_0 e}{m\omega} [\sin(\omega t + \varphi) - \sin(\varphi)]$$

Eq. 2.8

and its position [33]:

$$x(t) = \int_0^t v(t') dt' = \frac{E_0 e}{m\omega^2} [\cos(\omega t + \varphi) - \cos(\varphi)] + \sin(\varphi)t$$

Eq. 2.9

Where:  $\varphi$  is phase of electric field at which atom is ionized (often referred as: "electron is born").

Dependence of the electrons paths as a function of time, where the electric field phase is a parameter, reveals that just a fraction of the electrons are probable to return to the parent ion and re-collide (contributing to emission of radiation). The problem is addressed in more detail in Ref. [33]. This is the reason of the optimization of the electric field phase.

**Step III - Recombination.** After re-acceleration of the electron wave packet towards the ion it is plausible that electron will collide with the ion and will recombine. The excess of kinetic energy is transferred to the momentum of the emitted photon. The electrons which recombine with ions will emit harmonic radiation with energy of spectral lines defined as follows:

$$\hbar \nu = E_{kin} + I_p$$

Eq. 2.10

Where  $E_{\text{kin}}$  - is kinetic energy of an electron acquired by absorption of  $n$ -photons of driving field,  $I_p$  - is ionization potential corresponding to the shell from which the electron has been ripped off by the field.

There is a limit on the maximum emitted energy. It is given by maximum kinetic energy that electron has gained during acceleration. It was claimed that the path and kinetic energy of the electron is controlled by the phase of the electric field (Eq. 2.7 - Eq. 2.9). If phase is  $\sim 18^\circ$  the kinetic energy of electron is maximized and its value is  $\sim 3.17 \cdot U_p$  [33]<sup>1</sup>. Thus the energy of the highest harmonic order is given by:

$$\hbar \nu = 3.17 U_p + I_p$$

Eq. 2.11

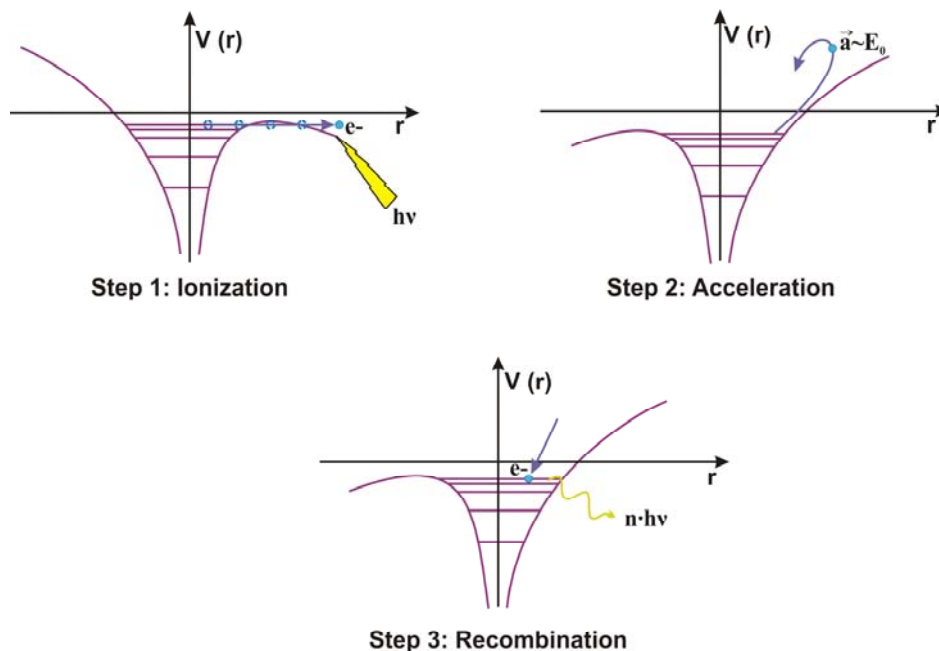


Figure 2.5. Summary of the 3-step model of HHG. The first step is tunnel-ionization of an atom. Next, an electron is driven away from its parent ion in the external electric field of an intense laser pulse. When the oscillating laser field reverses its sign the particle is re-accelerated back towards the atom and, finally, recombines. The last step leads to emission of a photon.

The HHG process can be also explained in the formalism of quantum mechanics [27]. The returning electron wave packet overlaps remaining portion of initial wave

<sup>1</sup>  $18^\circ = \sim 314$  mrad.

function. The coherent addition of the two wave functions induces a dipole as asymmetric displacement of the electron wave packet. The dipole oscillates as continuum wave function (of free electron packet) propagates. The oscillating dipole is a source of harmonic radiation and harmonic spectrum is given by Fourier transform of dipole acceleration. Instantaneous frequency of the dipole is determined by kinetic energy of the recombining electrons (i.e. electron wave packet and emitted photons are linked by the energy conservation:  $\hbar\nu = E_k$ , where the ionization potential is omitted due to the fact that  $E_k$  of electrons is seen by bound-state electron wave function, compare to Eq. 2.11). It is worth noting that the electron wave packet and the emitted photons are mutually coherent.

It is important to point the influence of tunnel-ionization process on HHG. The ionization rate increases with the amplitude of the electric field [31], [32] leading to generation of free electrons what results in their increasingly stronger contribution to HHG. Most energetic electrons are produced at  $18^\circ$ -phase of the electric field. On the other hand, multiphoton ionization produces constant number of electrons depending only on the intensity of the laser pulses and not the field phase. From cut-off law (Eq. 2.11) it is also known that energy of photons may be increased by increasing the ponderomotive potential  $U_p$  (when  $\gamma \ll 1$ ), thus shifting more into the strong-field regime.

### 2.2.2 Macroscopic analysis - phase-matching considerations

In most generic sense HHG process analysis is divided into two logical constituents: micro- and macroscopic. The three-step model deals only with atomic-scale phenomena leading to emission of a photon, thus, this part of the process is assigned to microscopic analysis of HHG. However, there are also macroscopic issues to be concerned. The crucial problem in this sense for HHG process is a phase-matching of the two propagating beams: XUV from HHG and of the driving laser. If we consider mismatch between  $m^{\text{th}}$  harmonic order and driving laser field oscillating at fundamental frequency  $\omega_f$  the wave vector of the mismatch could be written as [33]:

$$\Delta k = mk(\omega_f) - k(m\omega_f)$$

Eq. 2.12

In general there are three major components of total  $\Delta k$  that may be written as:

$$\Delta k = \Delta k_{natural} + \Delta k_{plasma} + \Delta k_{foc}$$

Eq. 2.13

1. Refractive index is a function of frequency. Since the phase velocity of radiation at given wavelength depends on refractive index, in general, radiation of different wavelengths propagates with different velocities what leads do de-phasing of particular spectral components. This input to total phase mismatch is called natural dispersion.
2. Because only little fraction of free electrons that had been generated by the laser field recombines with parent ion free-electron clouds are created. These free electrons give raise to additional component of refractive index [5]:

$$n_{plasma} = \sqrt{1 - \frac{N_e}{N_c(\omega_f)}}$$

Eq. 2.14

$$N_c(\omega) = \frac{\epsilon_0 m_e \omega^2}{e^2}$$

Eq. 2.15

Where:

$N_e$  - is free-electron density,

$N_c$  - is critical plasma density.

This leads to phase mismatch wave vector component [33]:

$$\Delta k_{plasma} = mk_{plasma}(\omega_f) - k_{plasma}(m\omega_f) = \frac{\omega_p^2(1-m^2)}{2mc\omega_f}$$

Eq. 2.16

3. HHG requires peak intensities in range of  $10^{13}$  -  $10^{16}$  W/cm<sup>2</sup>. In order to obtain such high intensities one has to focus driving laser beam. However, focusing involves phase-shift of the driving field along beam propagation direction 'z' (so called *Gouy phase shift*) [34]:

$$\varphi_{geo}(z) = -\arctan\left(\frac{2z}{b}\right)$$

Eq. 2.17

Where "b" is confocal parameter defined as follows [34]:

$$b = \frac{2\pi a^2}{\lambda}$$

Eq. 2.18

Where "a" is beam radius in the focal spot.

Gouy phase shift leads to the phase mismatch wave vector component [33]:

$$\Delta k_{foc} = mk_{foc}(\omega_f) - k_{foc}(m\omega_f) = \frac{2(m-1)}{b}$$

Eq. 2.19

If the HHG process takes place in hollow fiber the  $\Delta k_{foc}$  component is replaced by:

$$\Delta k_{cap} = mk_{cap}(\omega_f) - k_{cap}(m\omega_f) = \frac{u_{nl}^2 c(1-m^2)}{2md^2\omega_f}$$

Eq. 2.20

Where:

$u_{nl}$  - is  $l^{\text{th}}$  zero of Bessel function, and

d - is capillary inner radius.

There is also a component to phase mismatch originating from the fact that when the driving field pulse propagates in a gas it is defocused by the free electrons density gradient what leads to drop of intensity. Since the dipole moment is roughly linearly proportional to  $\propto -U_p / \omega_f$  with propagation resulting in de-phasing. However, this contribution is negligible compared to the de-phasing due to focusing and free-electrons generated index of refraction.

Phase-matching condition can be fulfilled by:

- tuning gas density (modification of gas density leads to modification of the index of refraction),
- changing position of the focus with respect to the gas resulting in minimization of Gouy phase-shift influence (gradient of function defined by Eq. 2.17 is highest at the beam waist),
- in the hollow-fiber geometry modification of the fiber parameters can develop perfect phase-matching,
- free electron density may be controlled by intensity and time duration of laser pulses.

### 2.2.3 Generic properties of high-order harmonics spectrum

An important feature of the harmonic spectrum is its universal shape. As already mentioned there is a spectral region of roughly equally intense spectral lines, so called *plateau*. The plateau is preceded by increase of spectral lines intensity in longer wavelengths which is subsequently followed by abrupt intensity drop-off. The short-wavelength part of spectrum extends to the limit defined by cut-off law. From this formula (Eq. 2.11) one can infer how to extend the wavelength range of HHG, e.g., by increasing ionization potential (proper choose of conversion medium or by working with ions for subsequent shells have higher ionization potential). Another way of doing so is by raising intensity or increasing wavelength of driving laser field (revoke Eq. 2.2 or Eq. 2.3).

It has been shown that intensity of intensity of  $m^{\text{th}}$  harmonic order is proportional to square of phase-matching factor ( $m^{\text{th}} \propto |Fq|^2$ ) [34]. This factor rapidly decreases with  $m$  leading to drop of intensity of spectral lines in the long-wavelength part of harmonic spectrum.

Additionally, in the plateau region the scaling law has been observed [34]:

$$I_m \propto b^3 \cdot \Delta t$$

Eq. 2.21

Where,  $I_m$  - is intensity of  $m^{\text{th}}$  harmonic order,  $b$  is confocal parameter,  $\Delta t$  is driving laser pulse duration. The dependence from  $b^3$  comes from the fact that total number of photons is spatially integrated. The dependence from duration of the pulse comes from temporal integration of the HHG process.

In most common scheme of HHG when only one-wavelength driving laser field is used (in gaseous media) the HHG spectra contain only odd harmonic orders. This could be understood by formalism presented, e.g., in Ref. [30]. This approach originates from perturbative theory of description of nonlinear optical phenomena and is followed here.

When low-strength external field  $\vec{E}(t) (\ll \sim 10^9 \text{ W/cm}^2)$  interacts with matter the material polarization  $\vec{P}(t)$  (or dipole moment per unit volume) is responding to excitation in linear fashion to the applied field. This relation is linked by linear susceptibility and reads:

$$\vec{P}(t) = \chi^{(1)} \vec{E}(t)$$

Eq. 2.22

However, if the field increases the nonlinear response of the harmonic oscillator appears. If the field is not too strong (for intensities smaller than  $\sim 10^{14} \text{ W/cm}^2$ )  $\vec{P}(t)$  can be expanded in Taylor series:

$$\vec{P}(t) = \chi^{(1)} \vec{E}(t) + \chi^{(2)} \vec{E}^2(t) + \chi^{(3)} \vec{E}^3(t) + \chi^{(4)} \vec{E}^4(t) + \dots$$

Eq. 2.23

If any arbitrary medium features e.g. third order nonlinearity ( $\chi^{(3)}$  does not vanish) the medium polarization is capable of being a source of nonlinearities of the third order (e.g. third-harmonic generation, nonlinear index of refraction and secondary phenomena having their origin in the dependence of  $n = f(I)$ , etc.). In general, there is a strong dependence between type of symmetries of media and their nonlinear properties. For instance, if a medium is centrosymmetric all its even-order susceptibilities vanish and thus those media are not able to give rise to any of even-order nonlinear phenomena. This is also the case of gasses (as well as e.g. liquids and amorphous solids). Since gases display inversion symmetry it is possible to obtain odd-order HHG only.

It ought to be stressed; however, that propagation effects can severely affect the resulting shape of the harmonic spectrum. This applies to both spectral content and the intensity of particular harmonic orders. This remark is of special importance when HHG scheme utilizes self-channeling (or, equivalently, long propagation distances in the conversion medium of the harmonic radiation).

#### 2.2.4 HHG geometries involving gaseous media

The most common experimental setup of HHG comprises (apart from laser system and diagnostic apparatus) *gas puff* target [35]. Such a target is basically a gas valve injecting a portion of a gas at desired pressure. The valve is repetitively open and laser pulses interact in proximity of valve exhaust. Typical repetition rate of the gas puffs is  $< 100$  Hz. The valves may have either circular symmetry or could be elongated. Elongated valves provide higher XUV beam outputs but limiting factor is re-absorption in a gas thus long valves are used for wavelengths  $> \sim 20$  nm (also because of the longer coherence length for longer wavelengths). On the other hand, circular (e.g. 0.5 mm diameter) gas puff valves are used in shorter-wavelength HHG.

High-order harmonics are also generated in gas cells. A gas cell is a simple container filled with a noble gas at moderate pressure (few tens of mbar). Arrangements with gas cells are very comfortable to work with because, compared to the gas puff targets, there are fewer parameters to optimize to obtain phase matching. In this case the phase matching is obtained by tuning only longitudinal position of a cell and gas pressure in a cell. For gas cells can be as long as desired (due to technical ease of construction compared to gas puff valves) this setup is also favorable when maximization of interaction length is wanted. Due to the above advantages HHG source developed at the Institute of Physics (IoP) and Prague Asterix Laser System (PALS) of the Academy of Sciences of the Czech Republic follows this setup.

Another possible geometry of HHG involves hollow fibers filled with a conversion gas [36]. In such a fiber laser pulses are propagating even meters long resulting in efficient transfer of driving field energy into XUV beam. This geometry is also popular due to ease of control of phase-matching by fiber parameters (Eq. 2.20).

### 2.3 High-order Harmonic Generation by molecules

Essentially, the physical mechanism of HHG in molecules is the same as in atomic gases (see paragraph 2.2) and can be understood by the same 3-step model. However, orbital structure of molecules and thus the description of the mechanism of HHG in this case is significantly different from the case when atomic conversion media are involved.

There has been many molecules proven to be capable of HHG:

- $N_2$  [27],[37],
- $CS_2$ , hexane,  $N_2$  [38],
- $O_2$ ,  $CO_2$  and  $N_2$  [39].

Very interesting feature of HHG in molecules is that the signal yield of particular harmonic order depends on laser light polarization ellipticity and its orientation with the respect to the direction of molecular axis. In general, the signal yield is highest for linearly polarized light perpendicularly oriented to the axis of molecule (Figure 2.6) [39].

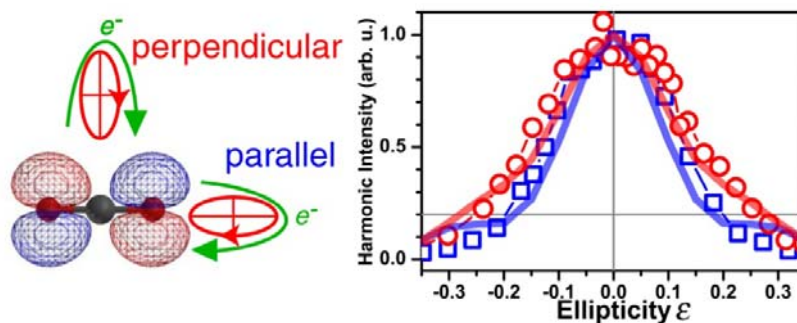


Figure 2.6. Dependence of HHG in molecules from the ellipticity and orientation of the molecular axis with the respect to laser polarization orientation. The molecule of interest is  $CO_2$  and curve on the right is a signal yield for 25<sup>th</sup> harmonic order [39].

The fact that the yield of HHG depends on orientation of the molecule with the respect to light polarization direction suggests that the HHG process (especially in molecules) is strongly affected by the shape of orbitals of the molecule. This idea has been motivation to Itatani et al. [27]. Finding the relation between orientation of the molecule and spectral intensities of high-order harmonics they succeeded to perform inverse calculation and obtained tomographic reconstruction of the most-outer orbital

of the  $N_2$  molecule. Since these orbitals are responsible for chemical properties of the molecules the results have a great impact on the state of our knowledge. Such direct measurement of orbitals is a first step to the "molecular movie", e.g., showing time-resolved process of creation of chemical bonds.

Another very interesting feature of HHG from molecules was unveiled during experiments in which the influence of molecular structure complexity on HHG efficiency was investigated. It turned out that the increasing complexity of the molecule is unfavorable for efficient HHG. When dissociating pre-pulse was applied the HHG yields were higher compared to case with unaffected molecules [38], [40]. It has been suggested [34] that the origin of the higher conversion efficiency in atomic media relies in fact that dipole phase depends on the angle between molecular axis and the pump laser polarization. An additional de-phasing mechanism would exist between the emitters in randomly aligned molecular media and it could imply worse phase matching compared with the monomers [40].

## 2.4 High-order Harmonic Generation from solid targets

HHG process can also take place at the interface between vacuum and solid targets. The physical process leading to HHG is different here and is explained in terms of resonant absorption. Let us now introduce reference system presented in Figure 2.7.

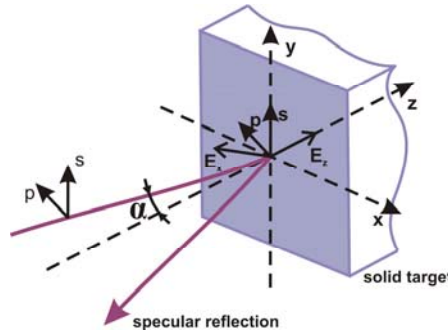


Figure 2.7. HHG from solid target surface geometry.

From electromagnetic analysis of reflection of radiation at an interface between two media it is known that in case of specular reflection at oblique angles ( $\alpha > 0^\circ$ ) "s" polarization is reflected according to Snell's law, or, alternatively, this polarization, does not propagate in z direction (due to the boundary conditions). On the other hand, "p" polarization can propagate in z direction into the medium. When a very intense laser pulse impinges upon the target, the plasma is created. In such a plasma light propagates to the layer of free-electron density equal to plasma critical density (Eq. 2.24). The laser radiation cannot propagate any farther, but, instead, the free-electron plasma wave (plasmon) is induced by "p" polarized light at frequency equal to light frequency (*resonant absorption*) and directionality of propagation along z axis.

$$N_c = \frac{4\pi^2 c^2 \epsilon_0 m_e}{e^2 \lambda_L^2} \approx \frac{1.1 \cdot 10^{21}}{\lambda_L^2 [\mu m]} [cm^{-3}]$$

Eq. 2.24

When laser light at frequency  $\omega_L$  mixes with the induced plasmon at frequency  $\omega_p$  the light at frequency of  $2\omega_L$  is generated. The  $2\omega_L$ -electromagnetic wave may propagate further into plasma since plasma critical density for  $2\omega_L$  is higher ( $4N_c$ ). Then, light at  $2\omega_L$  mixes with that at  $\omega_p$  generating  $3\omega_L$  component. This frequency radiation

can propagate until it reaches density of  $9N_c$ , and so on (up to some upper-limit density  $N_u$ ). This cascaded phenomenon leads to generation of harmonics of the order limited by plasma frequency and its maximum value is given by [34]:

$$q_{\max} \approx \frac{N_u}{N_c}$$

Eq. 2.25

The approximate relation for  $N_u$  is given by [34]:

$$N_u = \frac{E_0^2}{8\pi T_b}$$

Eq. 2.26

$T_b$  is background temperature [41].

Very important parameter is the product of  $I \cdot \lambda^2 [\mu m^2 W / cm^2]$ . For  $\lambda=1 \mu m$  and intensities below  $10^{18} W/cm^2$  Lorentz force can be approximated only by component coming from electric field, i.e. by  $e \cdot E_z$ . However, if intensity becomes comparable to  $10^{18} W/cm^2$  the relativistic effects bring increasingly significant input to Lorentz force from magnetic field component. For laser pulse intensities below the mentioned value (or for  $I\lambda^2 < 10^{18} \mu m^2 W/cm^2$ ) the only polarization that may induce harmonic generation is "p" polarization. However, above this value HHG may take place due to nonlinear mixing between longitudinal and transverse oscillations resulting in possibility of HHG from "s" polarized light [34].

Another way of describing of HHG from solid-vacuum interface involves an the oscillating plasma mirror. It could be shown by mathematical analysis that light reflected at critical surface oscillating at relativistic velocities contains harmonics of the incident beam (see [34]). This approach; however, will not be discussed in more detail here. Instead, some general properties of HHG from solids are shall be discussed. Probably the most interesting feature of HHG from solids is that all-order harmonic radiation is obtained. Additionally, it has been observed that the emission cone changes with the

intensity of driving laser field [34]. In general the emission cone is larger compared to the laser beam. When  $I\lambda^2$  reaches values of  $10^{15}$  -  $10^{16}$   $\mu\text{m}^2\text{W}/\text{cm}^2$  the emission solid angle strongly increases; for values above  $10^{17}$   $\mu\text{m}^2\text{W}/\text{cm}^2$  it is found to be isotropic (no angular distribution of HHG has been found [34]). Moreover, HHG efficiency and signal yield from solids drop above  $10^{16}$   $\mu\text{m}^2\text{W}/\text{cm}^2$ . The two phenomena are attributed to the transition from specular reflection regime of HHG to diffusion reflection regime.

The key parameters of HHG from solid-vacuum interfaces sources are:

- Intensity of the driving field (or more exactly the product of  $I\lambda^2$ ), which is basically the only limiting factor to the order of generated harmonics,
- angle of incidence of the driving field upon the target,
- contrast of the driving laser pulse.

Nowadays, this type of HHG source is drawing lots of attention in scientific world. This is due to huge potential capabilities of this type of source (e.g. odd and even harmonic orders generation and their number limited only by available intensity of the driving laser fields, conversion efficiency increasing with  $I\lambda^2$ ). For more detailed discussion on HHG from solids see, e.g., Refs [41]-[47].

## Chapter 3. Development of HHG source at IoP/PALS

The existing Ne-like zinc X-ray laser (XRL) at Department of X-ray Lasers (Institute of Physics, the Academy of Sciences of the Czech Republic) and Prague Asterix Laser System (PALS) emits coherent radiation at 21 nm and is capable of delivering energy of few-mJ in a single shot [48]. However, practical use of this X-ray laser is limited by the driving laser system which is able to shoot every 0.5 hour. In case of HHG source, the low single-shot energy ( $\sim$ nJ) is compensated by the repetitive operation of the source (up to  $\sim$ MHz). It is also possible to easily tune the HHG source parameters to obtain coherent spectral line at 21 nm. Thus this source is complementary to the existing X-ray laser in wide range of applications.

### 3.1 Laser system

The source of high-order harmonics built at the Institute of Physics (IoP) and at PALS is based on the commercial titanium-sapphire laser system (Coherent Inc). The system comprises Micra master oscillator and Legend regenerative amplifier (together with pumping laser Evolution-15). The scheme of the laser is presented in Figure 3.1. The system is built based on CPA (chirped pulse amplification) technique. Micra is a mode-locked oscillator providing train of seed pulses of duration of 20 fs and at repetition rate of 76 MHz. These pulses are stretched by a pair of gratings to about 200 ps in duration

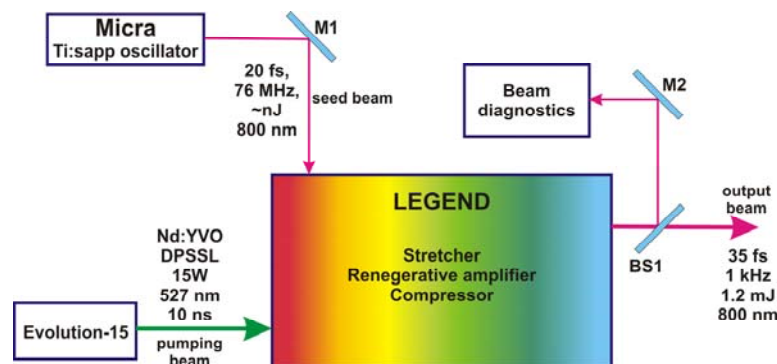


Figure 3.1. Laser system used for HHG at IoP/PALS.

and subsequently amplified. In the amplifier a pair of Pockels cells (pulse slicer) picks only some of the seed pulses resulting in output repetition rate of 1 kHz. The Evolution-15 pumping laser is a frequency-doubled Nd:YVO laser ( $P=15$  W,  $\Delta t=10$  ns,  $\lambda_c=527$  nm, 1 kHz). The amplified beam is compressed by dual-grating compressor (in air) to the pulse duration of  $\Delta t < 40$  fs. The amplified pulse (after compressor) has energy over 1.2 mJ. Central wavelength is 810 nm and repetition rate is 1 kHz. The beam size is 10 mm FWHM.



Figure 3.2. Picture showing the table-top femtosecond laser system deployed in the HHG source. The system comprises Micra oscillator and Legend regenerative amplifier pumped by Evolution laser (visible in Figure 3.3).



Figure 3.3. Evolution Nd:YVO laser system provides pumping energy at its second harmonic for regenerative amplifier (Legend). The system is controlled using a notebook through two control boxes visible in the upper part of the picture.

### 3.2 Experimental infrastructure

The experimental setup of the HHG source is presented in Figure 3.4. The source has been built in a gas cell arrangement. The near infrared (NIR) femtosecond laser pulses of the system described in Section 3.1 are focused with a dispersion-corrected lens (from fused silica or  $\text{MgF}_2$ ) in a cell filled with a noble gas at moderate pressure (tens of mbar). Additionally, the lens is preceded by input iris for defining the driving beam size. The interaction of the very intense ultrashort NIR pulses leads to generation of high-order harmonics as described in Section 2.2. The gas cell and all diagnostics are placed in a vacuum system. The real photo of the experimental infrastructure may be seen in Figure 3.5.

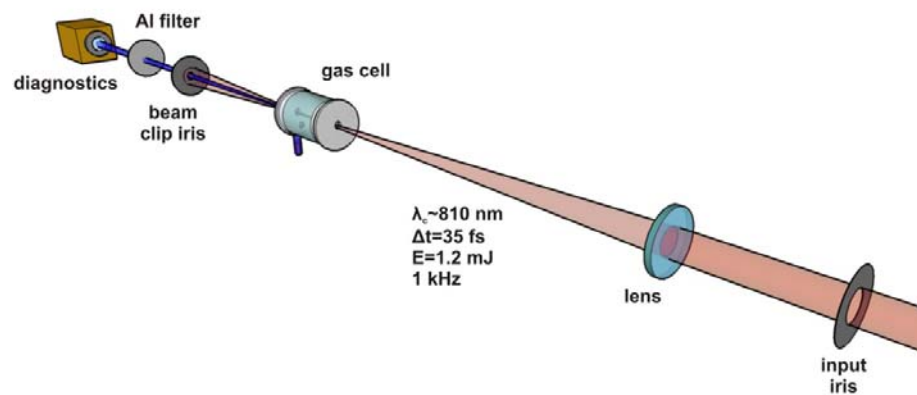


Figure 3.4. Schematic experimental drawing of HHG source at the IoP/PALS.



Figure 3.5. HHG experimental beamline at IoP/PALS. The beamline comprises titanium-doped sapphire laser system, HHG source placed in the source vacuum chamber (the blue in the picture) and application chamber (grey in the picture, downstream beam propagation direction).

The main component of the beamline is a gas cell (Figure 3.6 and Figure 3.7). The design of the cell allows changing gas cell length. It is mounted on XYZ motorized stage for easy manipulation during the experiment. The inner part of the cell is made of a transparent material for ease of viewing. The gas cell is linked to the pressure controller (P-602CV-AGD-33-V-350A Bronkhorst High-Tech BV) which supplies the cell with the gas at desired constant pressure. In HHG source optimization argon gas as a conversion medium was used.

The beamline comprises also diagnostics preceded by an Al filter and an iris for partial NIR beam clip.

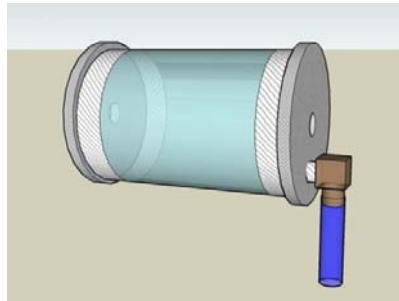


Figure 3.6. Conceptual design of a gas cell.



Figure 3.7. Picture of the gas cell used in the experiments.

### 3.3 Diagnostic methods and techniques

The main two diagnostics for the characterization of the HHG source were camera for  $M^2$  parameter measurement and transmission grating spectrometer (TGS) for spectral characterization. The camera (Pixelink PL-A781) is based on CMOS technology chip featuring size of 2/3" and resolution of 3000 x 2200 pixels (3.57 x 3.57  $\mu\text{m}$  pixel size). The chip covering glass has been removed and the sensor has been covered with 5  $\mu\text{m}$  layer of P43 phosphor. The camera has been enclosed in stainless steel housing for vacuum compatible operation [49].



Figure 3.8. Pixelink XUV CMOS camera.

For very precise spectral measurements TGS was used [50]. The spectrometer, as displays Figure 3.9, comprises relay flat mirror and imaging spherical mirror (both Au-coated for grazing incidence geometry). Both mirrors size is 2". The dispersion element is a free-standing transmission grating (2500 lines/mm;  $\text{nm}^2$  LLC). Spectrum was detected with an X-ray CCD camera (Andor DX440-DN). The real picture of the TGS is shown in Figure 3.10.

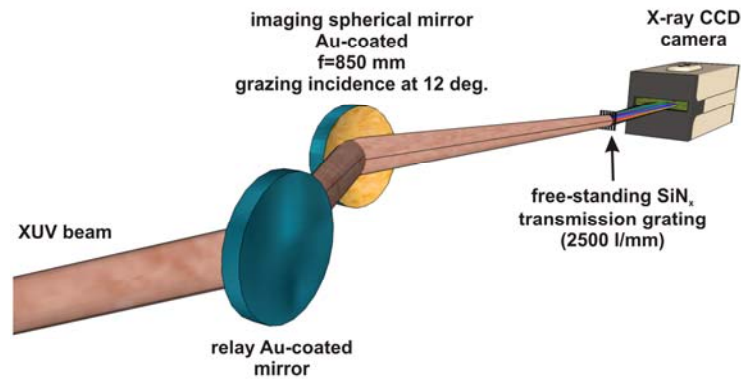


Figure 3.9. Schematic of the transmission grating spectrometer.



Figure 3.10. Real photo of TGS (the CCD portal is at the right hand side of the spectrometer in the photo).

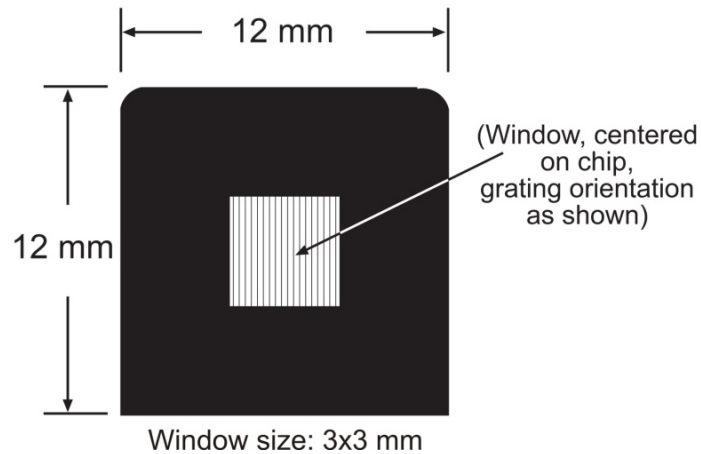


Figure 3.11. Schematic drawing of the  $\text{SiN}_x$  grating used in TGS [51].

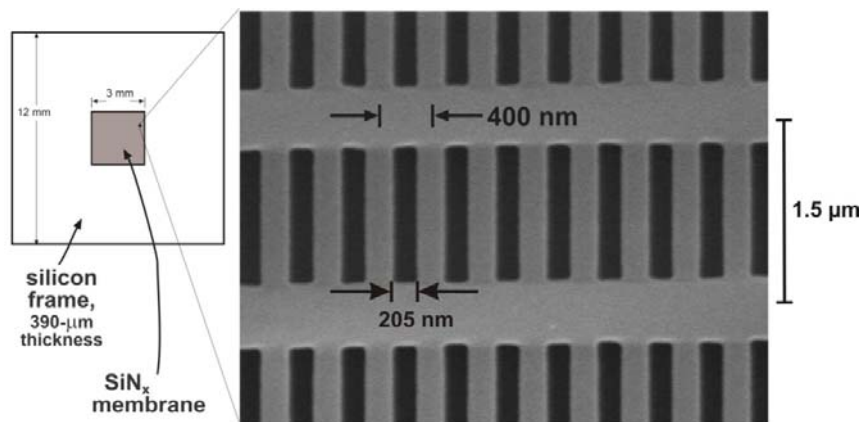


Figure 3.12. SEM image of the grating. The grating period was 400 nm and the linewidth was 205 nm. The window size (the size of the grating) was 3 x 3 mm [51].

Special calibration software has been coded (in Delphi 6 programming language).

The print screen of the program is shown in Figure 3.13. The software is capable of:

- computation of geometrical arrangement of the spectrometer in the experiment (e.g. distances between TGS components and source),
- evaluation of TGS properties (e.g. for given grating, CCD and distances it is able to evaluate spectral range and resolution);
- it also possesses some optimization features (e.g. as functional dependences between parameters of choice).

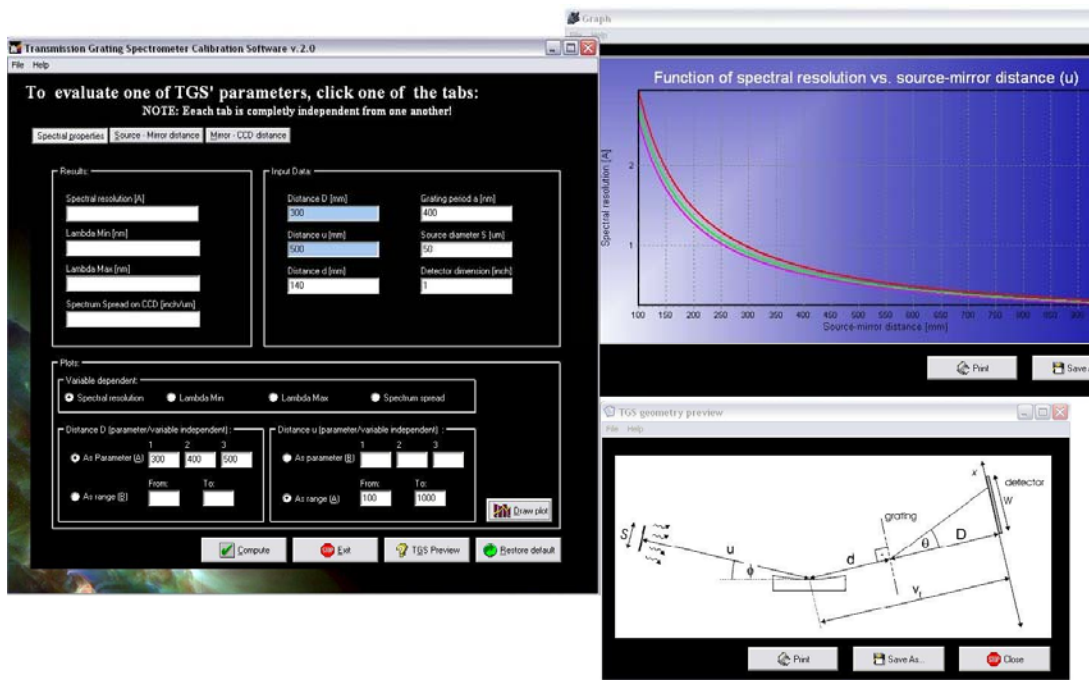


Figure 3.13. TGS calibration software.

In the measurements spectrometer was set up to measure spectrum in range below  $\sim 60$  nm with resolution  $< 1$  Å (distance between spherical mirror and the source  $\sim 1$  m, distance between spherical mirror and grating 140 mm, distance between grating and detector 300 mm, the source size was assumed to be 100  $\mu\text{m}$ , and transmission grating period was 400 nm with line width of 205 nm, radius of spherical mirror  $R=1700$  mm, grazing incidence angle onto spherical mirror  $\phi=12^\circ$ ). The theoretical estimation of TGS resolution has been confirmed by experimental results.

Absolutely calibrated X-ray CCD camera Andor DX440-DN has been also used alone for absolute estimation of the total HHG signal (preceded only with beam clip and an Al filter) and for the XUV beam profile measurements. The camera has 2048 x 512 pixel matrix. The pixel size is 13.5 x 13.5  $\mu\text{m}$  resulting in matrix dimensions of 27.6 x 6.9 mm.

## Chapter 4. HHG source characterization

### 4.1 Optimization of the source parameters

The first experimental campaign performed at IoP/PALS involving HHG source was related to comprehensive characterization of the HHG source and its optimization.

The parameters under investigation were:

- chirp of NIR femtosecond laser pulse,
- NIR beam size,
- focal length of the lens used in setup,
- gas cell length,
- gas pressure,
- cell position.

In the experiment, lenses of three focal lengths were sequentially deployed:  $f=750$ ,  $1000$  and  $1500$  mm. The experimental conditions for our laser system ( $\lambda_c=810$  nm,  $\Delta t=35$  fs,  $1.2$  mJ,  $1$  kHz,  $10$  mm FWHM beam size) and argon gas (most outer shell ionization potential  $I_p=15.759$  eV) in the interaction region are presented in Table 4.1.

	<b>f=750 mm</b>	<b>f=1000 mm</b>	<b>f=1500 mm</b>
Radius of diffraction limited NIR focal spot [ $\mu\text{m}$ ]	146.4	195.2	292.8
Confocal parameter $b$ [mm]	168.33	299.26	673.34
Intensity $I$ [ $\text{W}/\text{cm}^2$ ]	$5.092 \cdot 10^{13}$	$2.864 \cdot 10^{13}$	$1.273 \cdot 10^{13}$
Electric field strength $E_0$ [ $\text{V}/\text{cm}$ ]	$1.959 \cdot 10^8$	$1.469 \cdot 10^8$	$9.794 \cdot 10^7$
Ponderomotive potential $U_p$ [eV]	3.043	1.712	0.761
Keldysh parameter $\gamma$ [.]	1.609	2.146	3.218

Table 4.1. Estimation of the experimental conditions in the interaction region.

#### 4.1.1 Chirp of the NIR femtosecond laser pulse

One of the parameters of great practical usefulness is a source tunability. In case of high-order harmonics it can be accomplished by changing the conversion medium, which predominates the wavelength range of generated harmonics. For example,

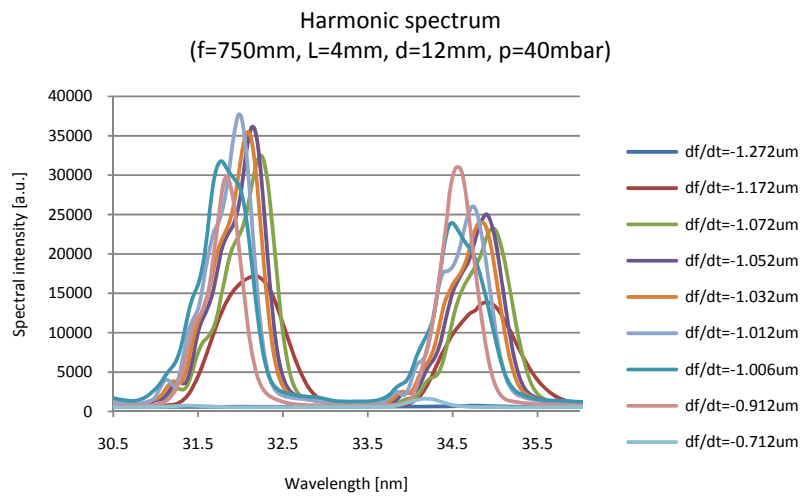
harmonics from argon are centered around 30 nm, from neon ~13 nm. Even shorter wavelengths could be obtained from helium (~10 nm), which in general depends on ionization potential of the medium. Additionally, very fine tuning in range of up to a few nm could be performed by tuning chirp of NIR femtosecond pulse. Physically, this originates from the fact that kinetic energy of a tunnel-ionized electron depends on the phase of the driving electric field according to the formula [34]:

$$\left\langle \frac{1}{2} m V^2 \right\rangle = \frac{e^2 E^2}{4m\omega^2} (1 + 2\cos^2 \omega t_0) = U_p (1 + 2\cos^2 \omega t_0)$$

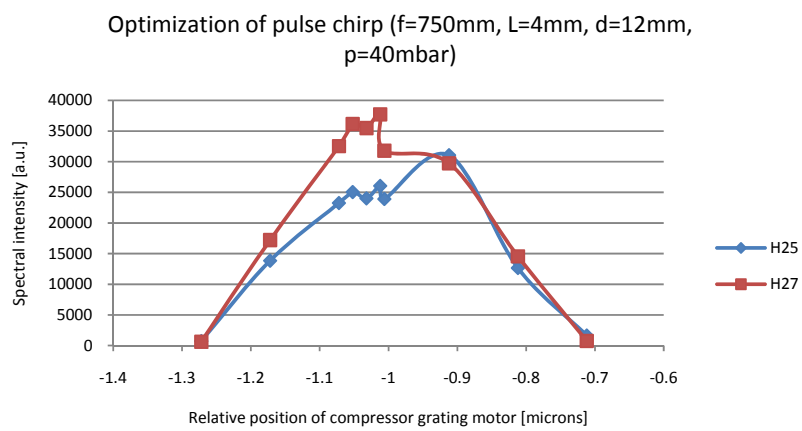
Eq. 4.1

Optimization of the source chirp has been performed in the setup presented in Figure 3.4. The TGS (Section 3.3) was used as a main diagnostic device. Selected experimental results are presented in Graph 4.1 - Graph 4.23. Experimental conditions are embedded in each graph. The two strongest spectral lines: for f=750 mm and f=1000 mm: 27<sup>th</sup> and 25<sup>th</sup> harmonic, for f=1500 mm: 19<sup>th</sup> and 21<sup>st</sup> were used in analysis of the results. All graphs are normalized to 0.5 s integration time and 0.8 μm thickness of Al filter. As a conversion medium argon gas was used. The denotations used are:

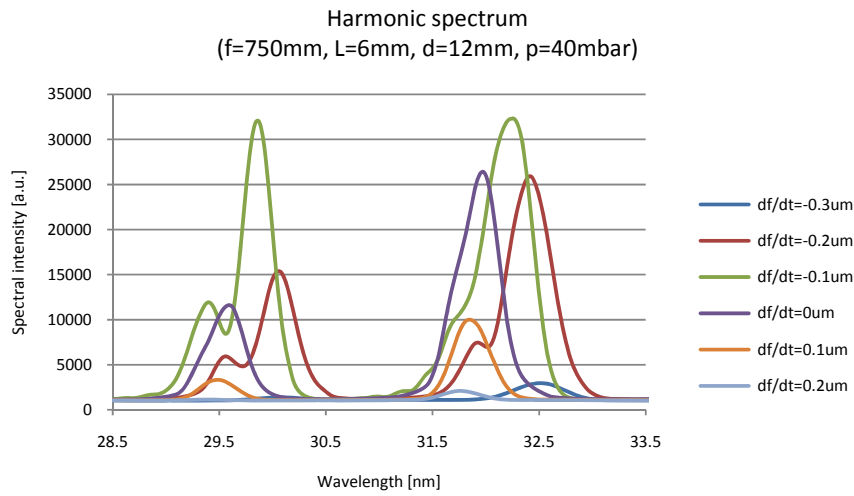
- L - gas cell length,
- p - pressure inside the gas cell,
- f - focal length of the lens,
- d - diameter of the opening of the entrance iris (before lens, as in Figure 3.4),
- df/dt (parameter in the graphs) is the position of the motor of one of the gratings inside the compressor. Movement of the grating position changes the chirp of the pulse,
- H25 stands for 25<sup>th</sup> harmonic order, H27 for 27<sup>th</sup>, etc.



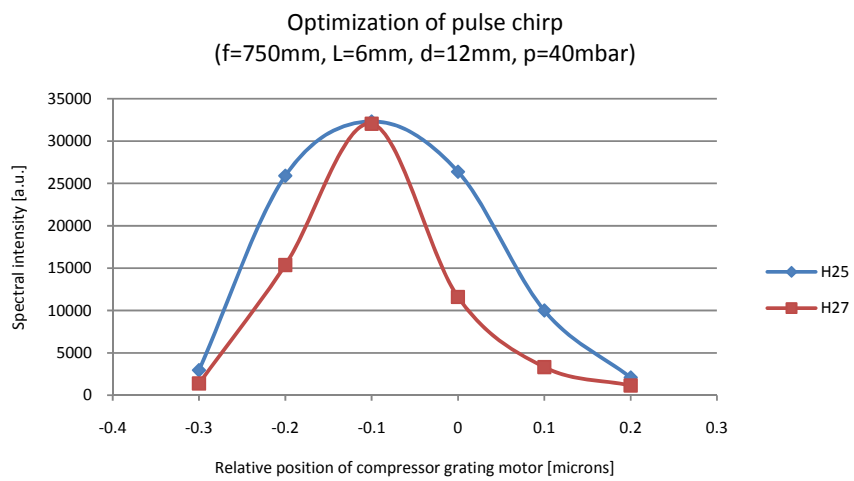
Graph 4.1. Tunability of HHG.



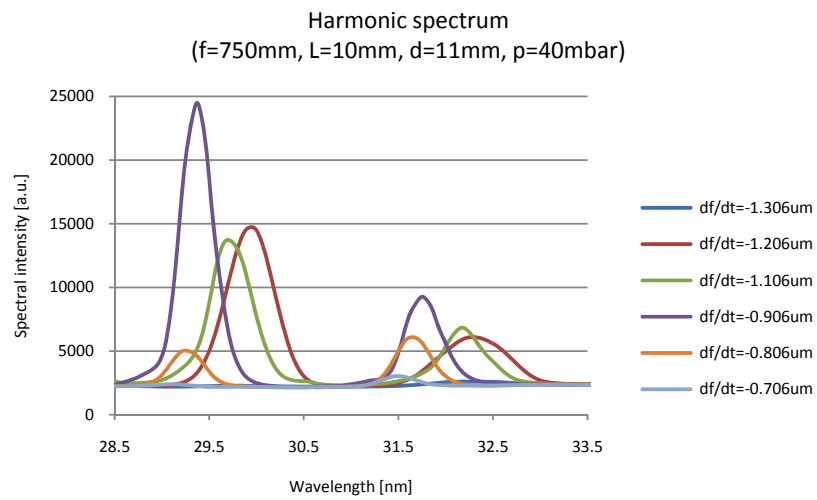
Graph 4.2. Optimization of chirp of NIR laser pulse.



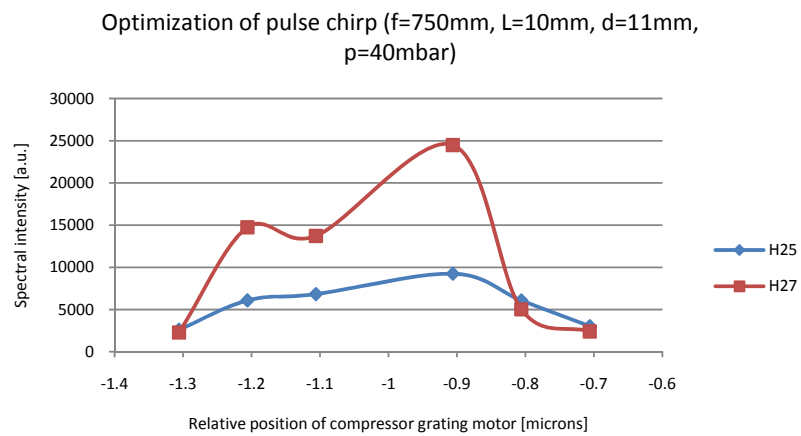
Graph 4.3. Tunability of HHG.



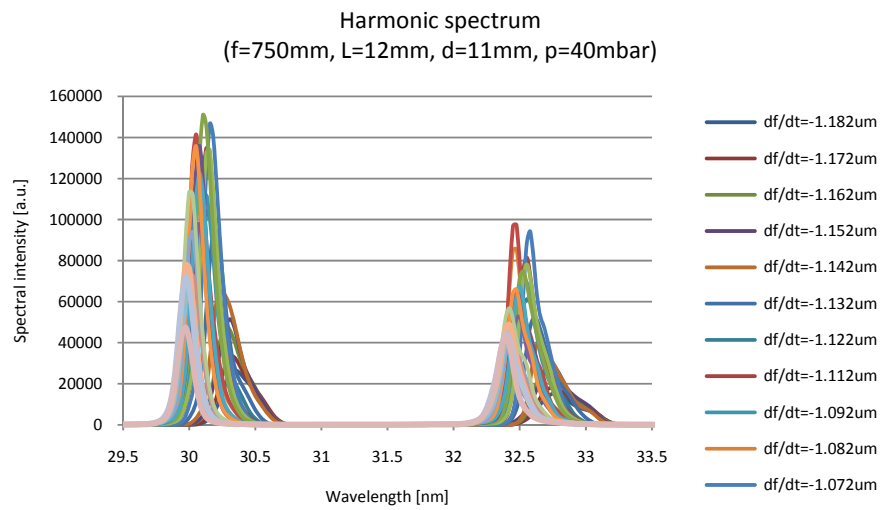
Graph 4.4. Optimization of chirp of NIR laser pulse.



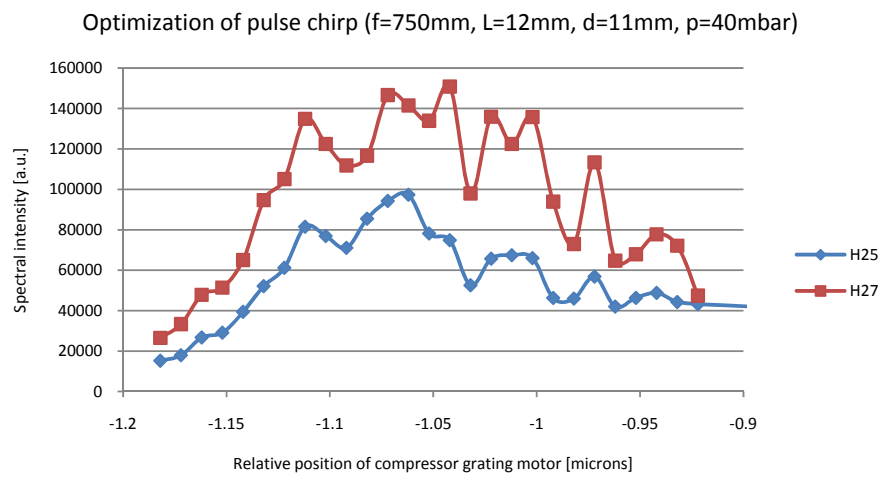
Graph 4.5. Tunability of HHG.



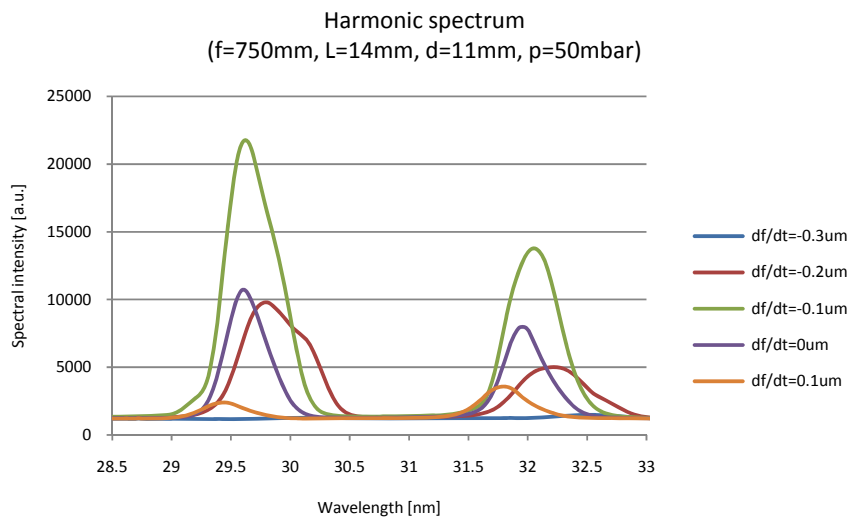
Graph 4.6. Optimization of chirp of NIR laser pulse.



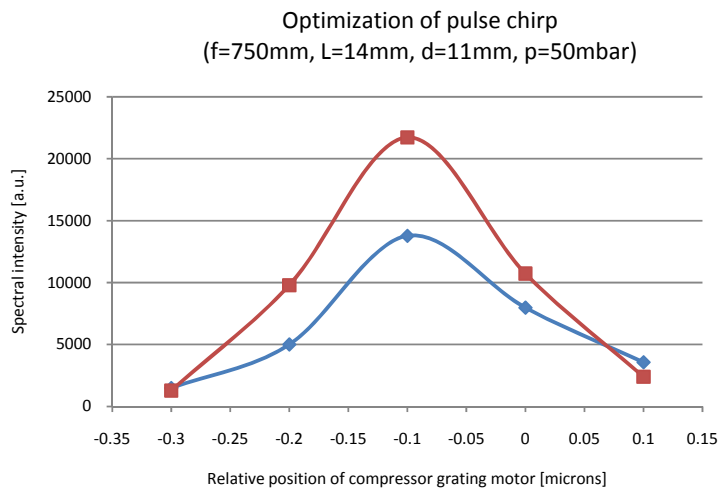
Graph 4.7. Tunability of HHG.



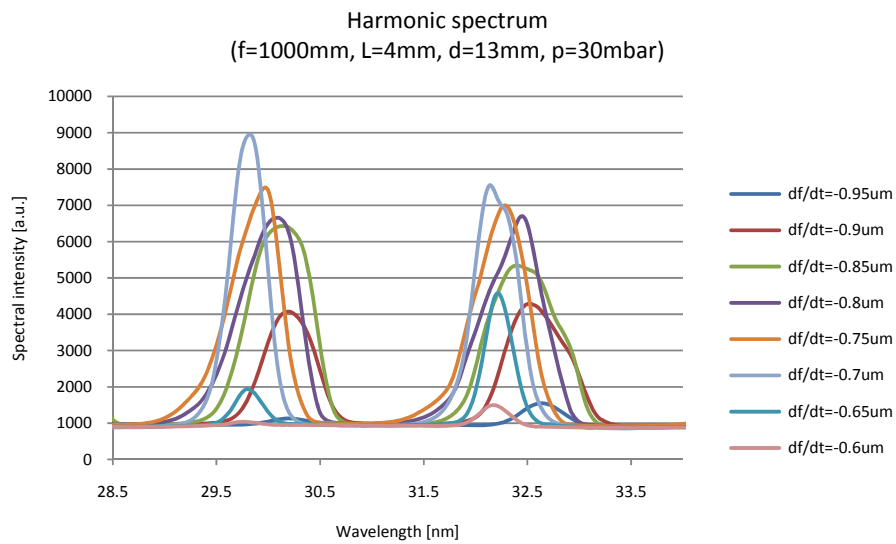
Graph 4.8. Optimization of chirp of NIR laser pulse.



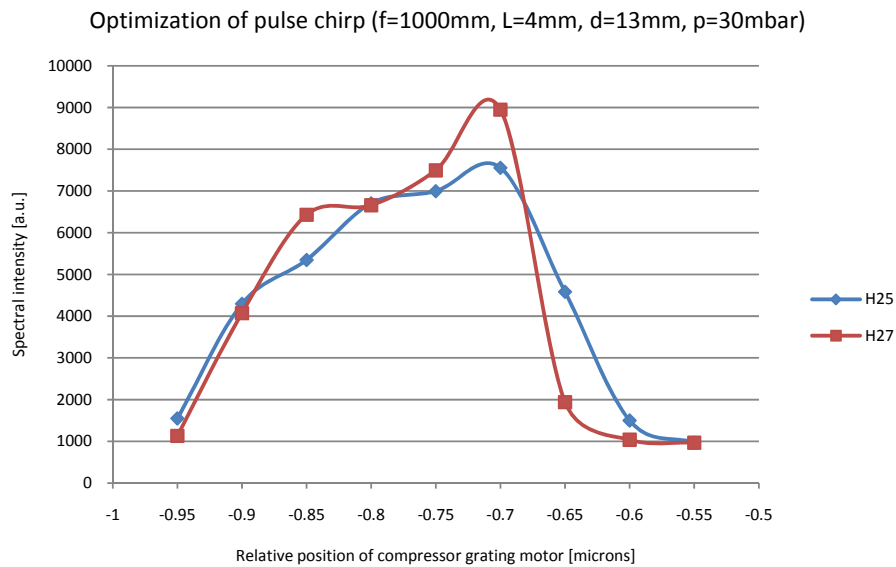
Graph 4.9. Tunability of HHG.



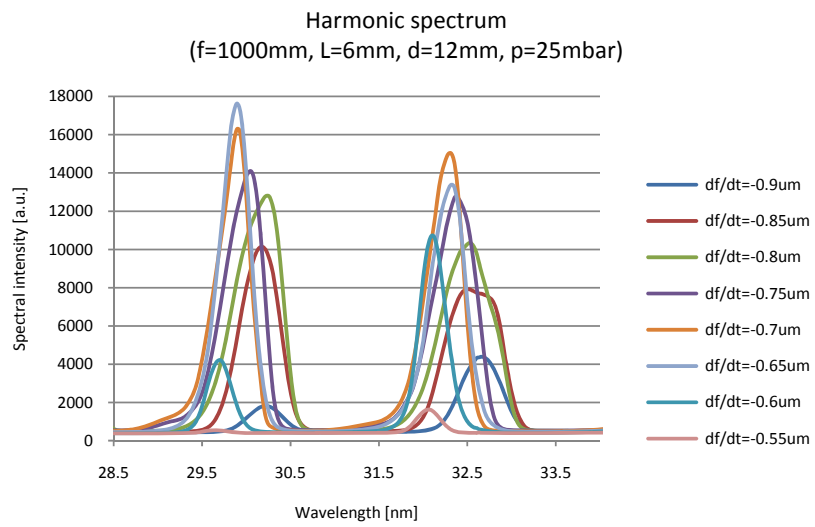
Graph 4.10. Optimization of chirp of NIR laser pulse.



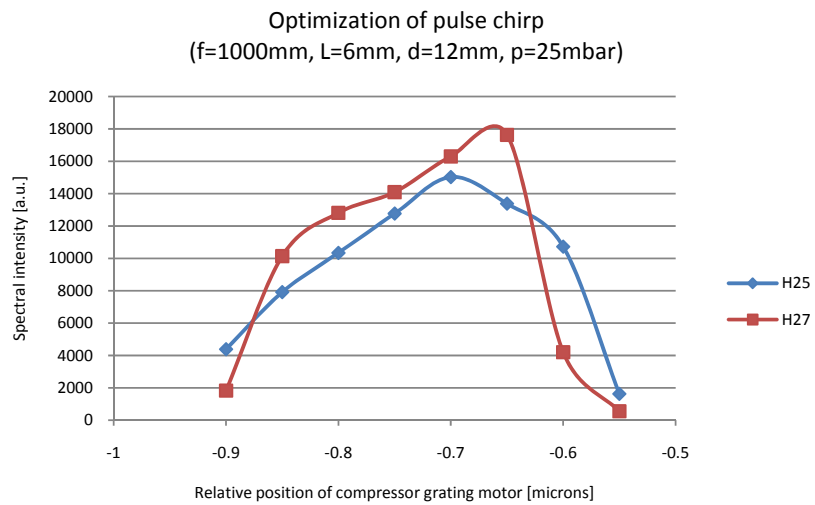
Graph 4.11. Tunability of HHG.



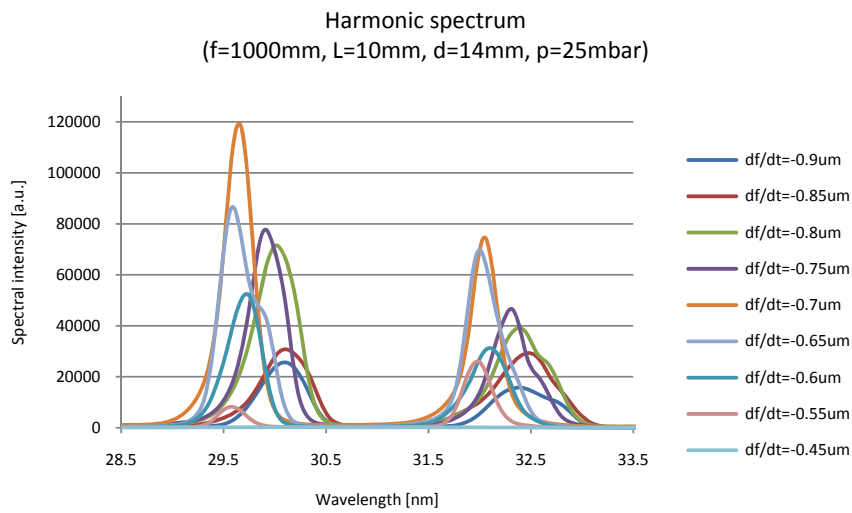
Graph 4.12. Optimization of chirp of NIR laser pulse.



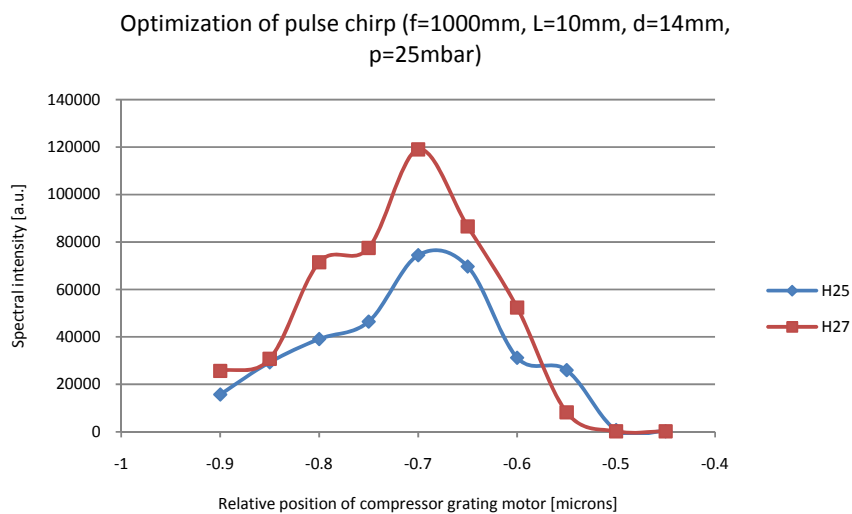
Graph 4.13. Tunability of HHG.



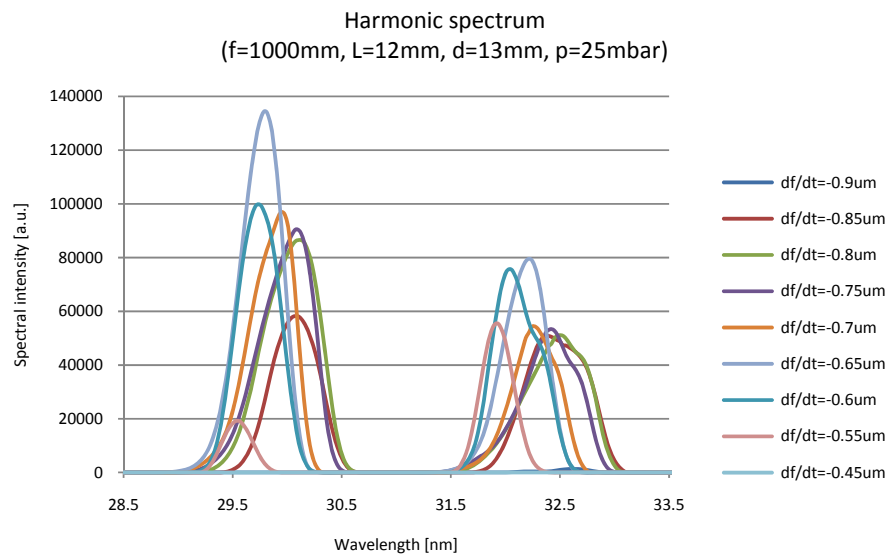
Graph 4.14. Optimization of chirp of NIR laser pulse.



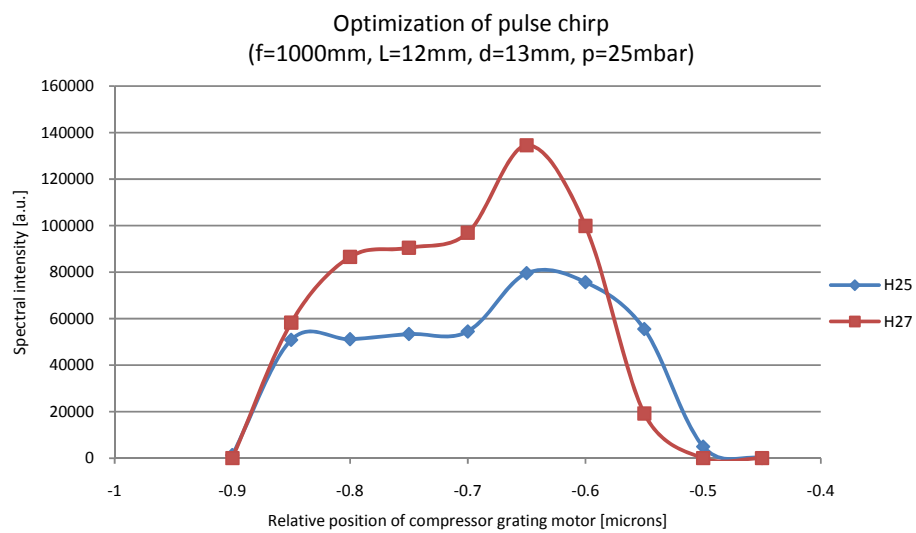
Graph 4.15. Tunability of HHG.



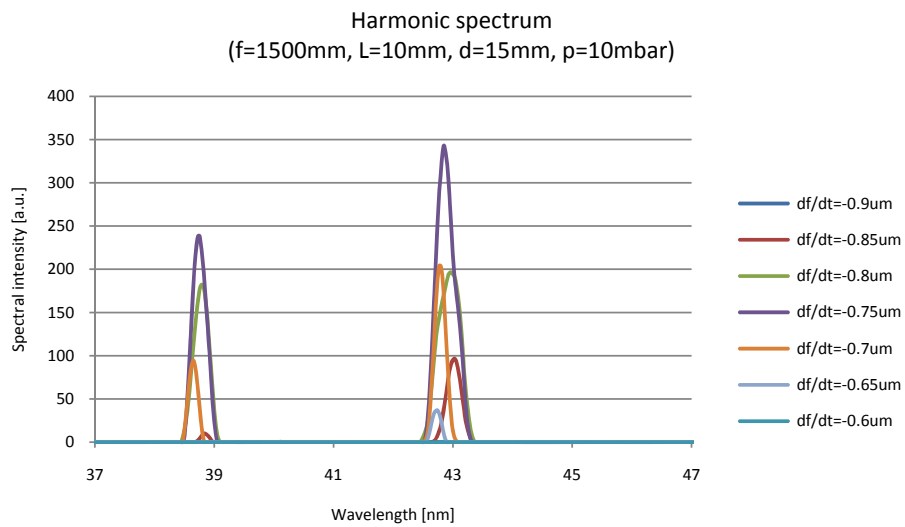
Graph 4.16. Optimization of chirp of NIR laser pulse.



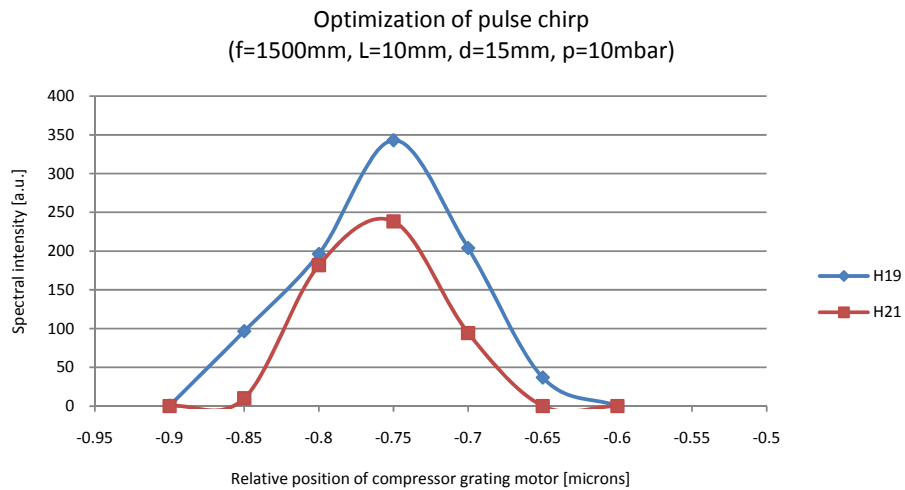
Graph 4.17. Tunability of HHG.



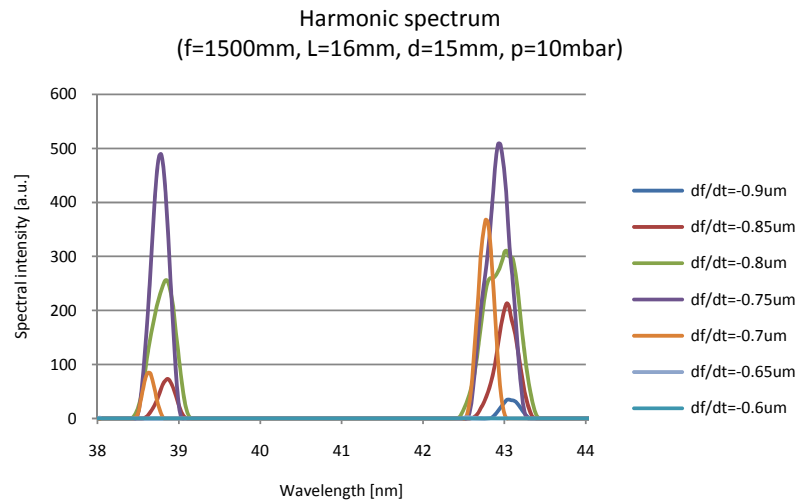
Graph 4.18. Optimization of chirp of NIR laser pulse.



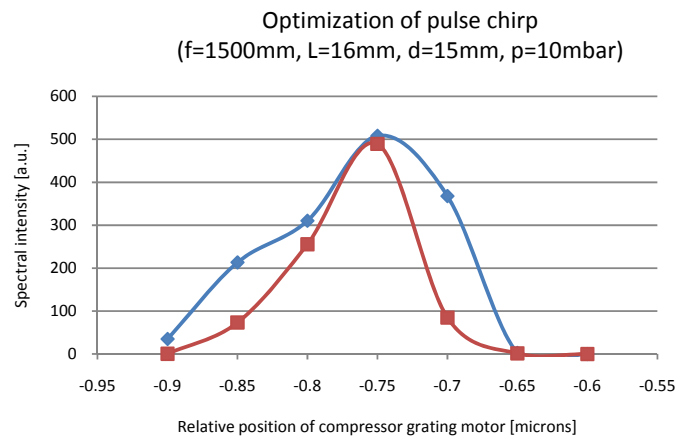
Graph 4.19. Tunability of HHG.



Graph 4.20. Optimization of chirp of NIR laser pulse.



Graph 4.21. Tunability of HHG.

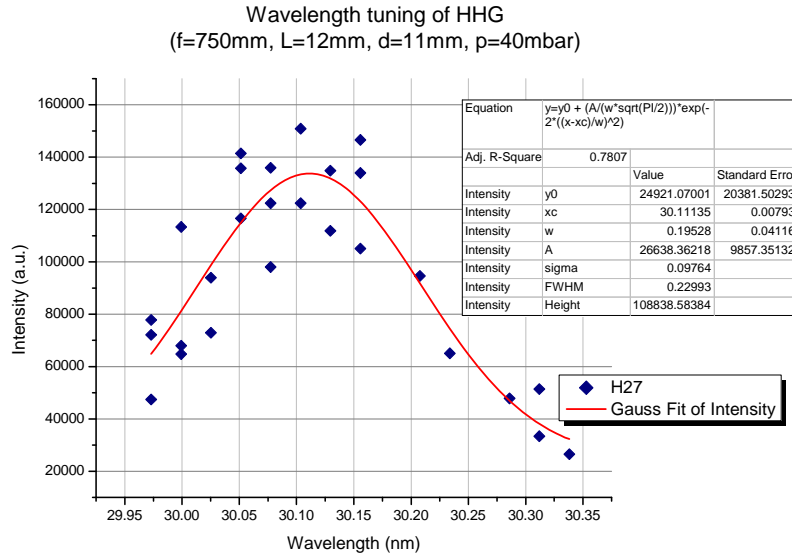


Graph 4.22. Optimization of chirp of NIR laser pulse.

The ability of HHG sources to the fine wavelength tuning is used e.g. during HHG beam amplification experiments to match absorption line of X-ray laser plasma amplifiers (see Section 6.2). However, in such a case one has to keep in mind that tuning of HHG features a drawback which is an intensity drop when departing from optimal conditions. The phenomenon is displayed in Graph 4.23. In this case the shift in wavelength only by 0.23 nm from optimal conditions (at 30.1 nm) caused signal drop by 83 %!

The presented experimental results display the existence of the optimal phase of the driving laser field during the HHG process. It is also worth mentioning that optimal

conditions are the same for all harmonic orders at a time, which are difficult to quantify absolutely since during the experimental campaign the laser needed to be a few times realigned. This was caused by air turbulences resulting in the beam walk-off, and change of moisture in the laboratory. Each, even very minor realignment led to new optimal distance between the gratings which had to be found.



Graph 4.23. Intensity drop during wavelength tuning of 27<sup>th</sup> harmonic order.

#### 4.1.2 Size of the NIR driving beam

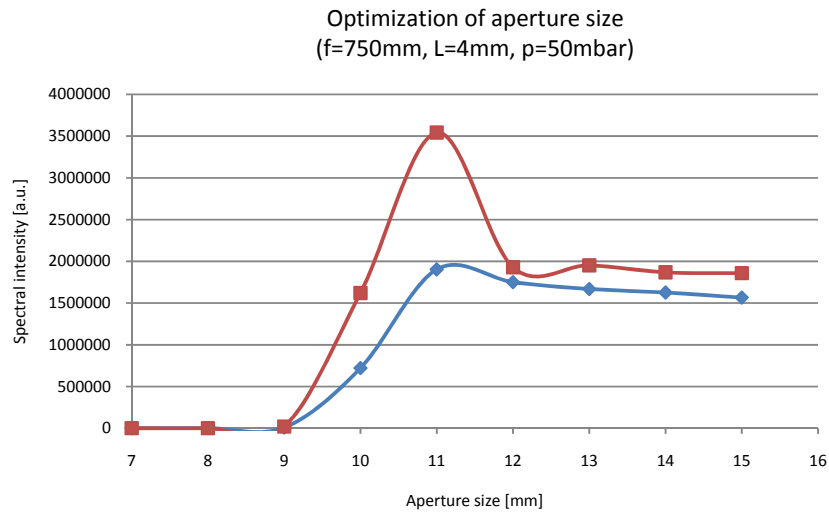
In order to maximize source total output one has to tackle the phase matching issue. The geometrical component to the phase mismatch vector finding its origin in the Gouy phase shift in the region of the focus can be minimized by changing confocal parameter  $b$  which was defined by Eq. 2.18. Confocal parameter  $b$  is related to Rayleigh length  $z_R$ :

$$b = 2 \cdot z_R$$

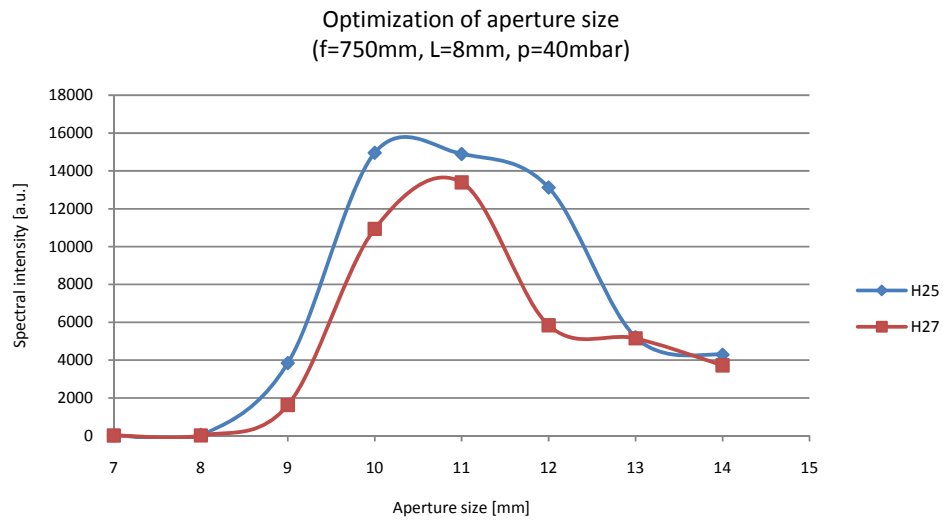
Eq. 4.2

Since focal spot size is a function of the beam diameter, experimentally, changes of  $b$  parameter are obtained by changing driving field beam size.

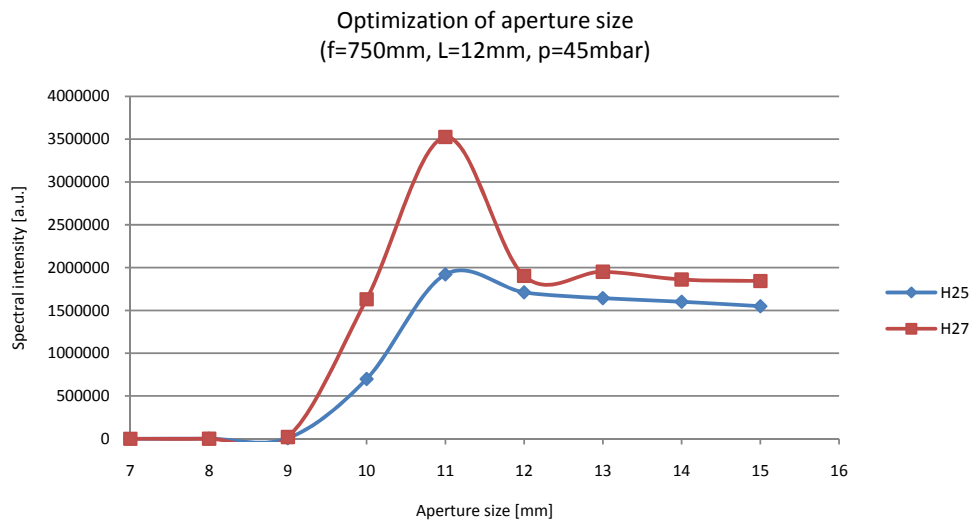
The experimental results are shown in Graph 4.24 - Graph 4.32. The graphs present spectral intensity of the selected harmonic orders as a function of aperture size of the iris at the entrance of the experimental setup. The meaning of the symbols in the graphs is the same as in previous section.



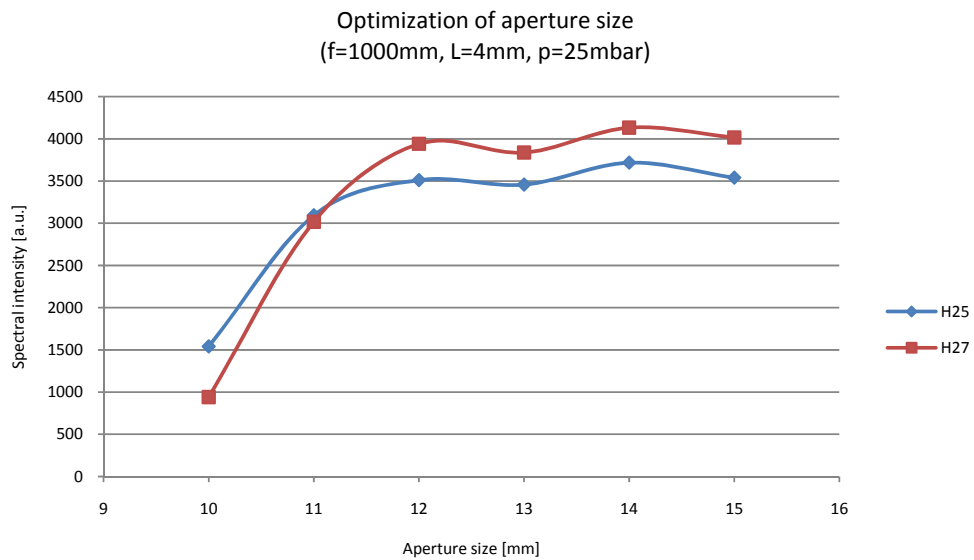
Graph 4.24. Optimization of NIR beam size.



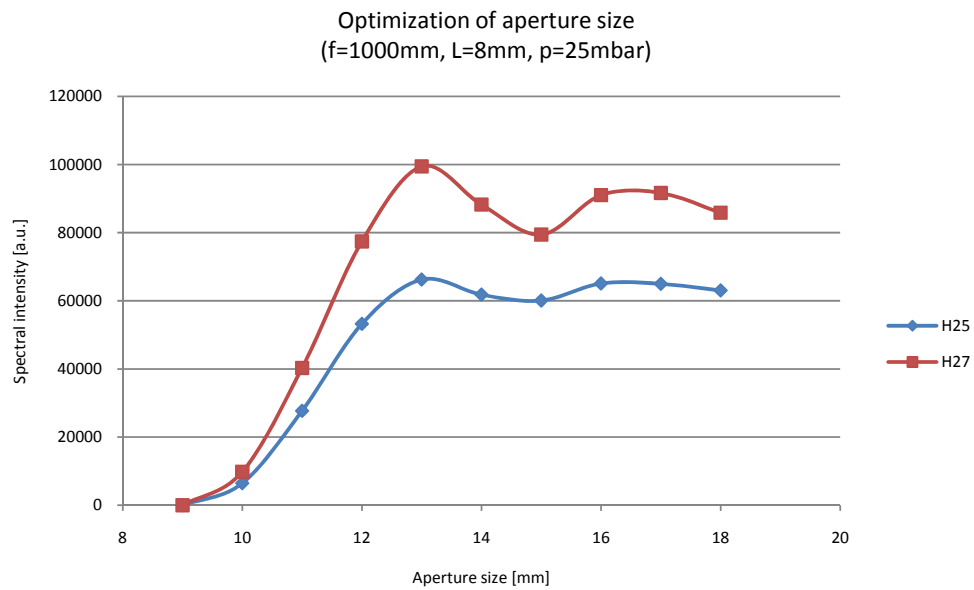
Graph 4.25. Optimization of NIR beam size.



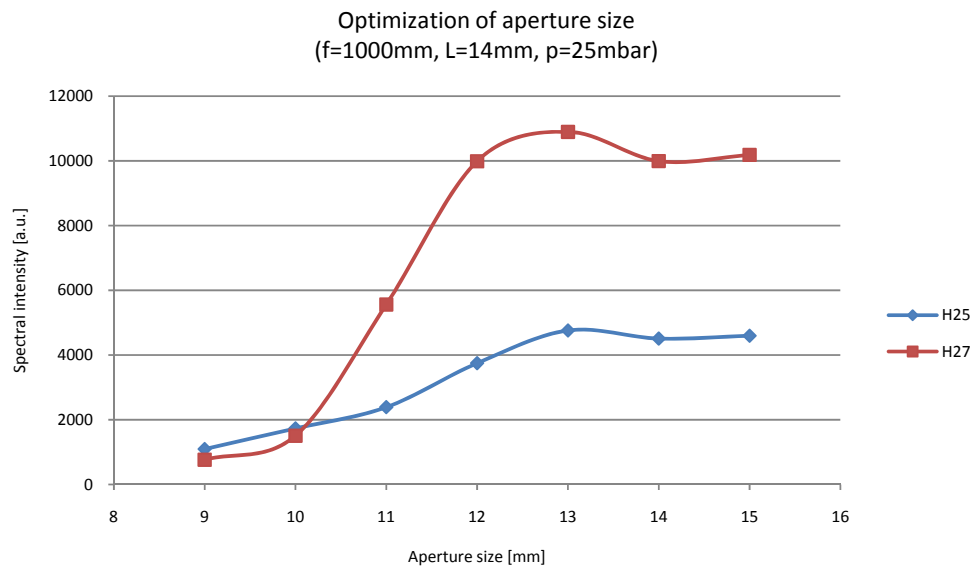
Graph 4.26. Optimization of NIR beam size.



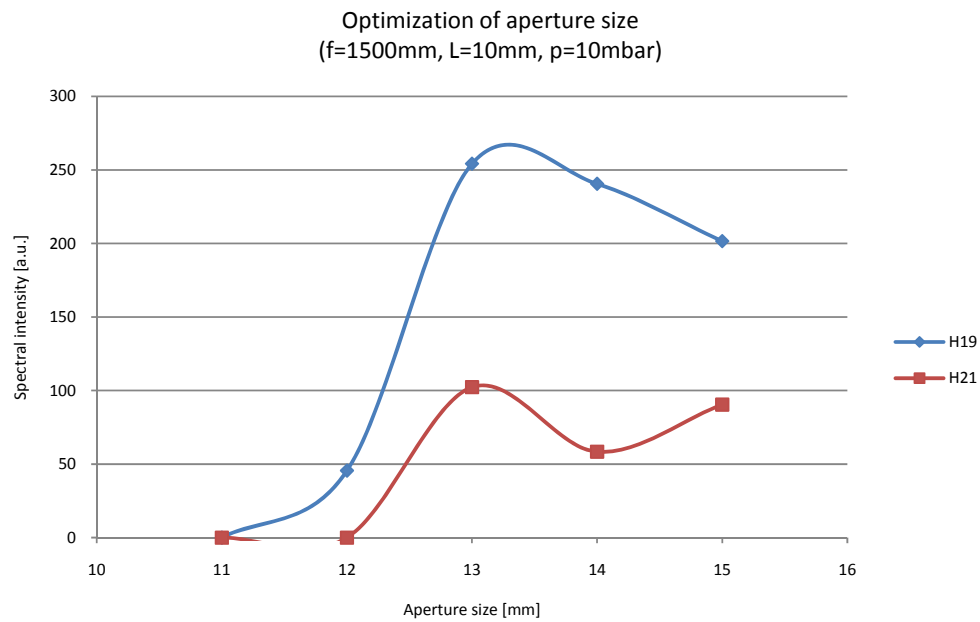
Graph 4.27. Optimization of NIR beam size.



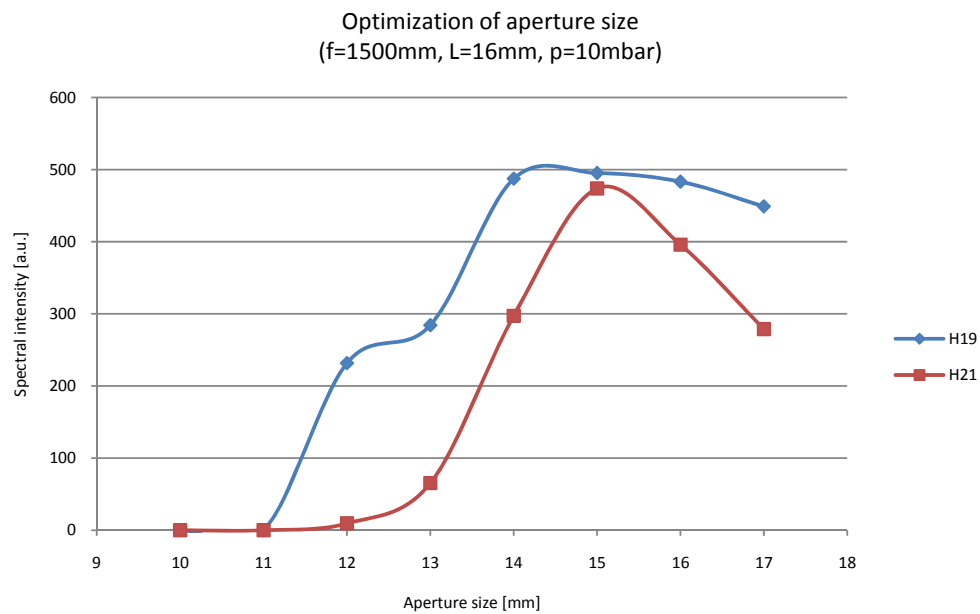
Graph 4.28. Optimization of NIR beam size.



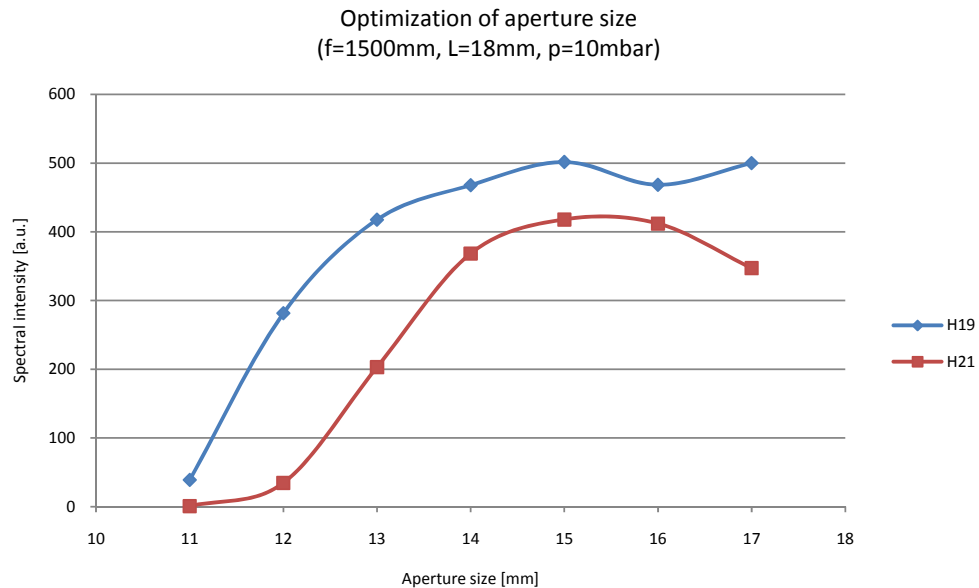
Graph 4.29. Optimization of NIR beam size.



Graph 4.30. Optimization of NIR beam size.



Graph 4.31. Optimization of NIR beam size.



Graph 4.32. Optimization of NIR beam size.

Optimal iris size of the aperture was found to be 11 mm for  $f=750$  mm lens and 13 mm for  $f=1000$  mm lens. To keep intensity constant in the interaction region while increasing focal length of the lens the increase of laser intensity is required (because focal spot increases). This was found to be an issue in the experimental setup (due to limits of the available laser system).

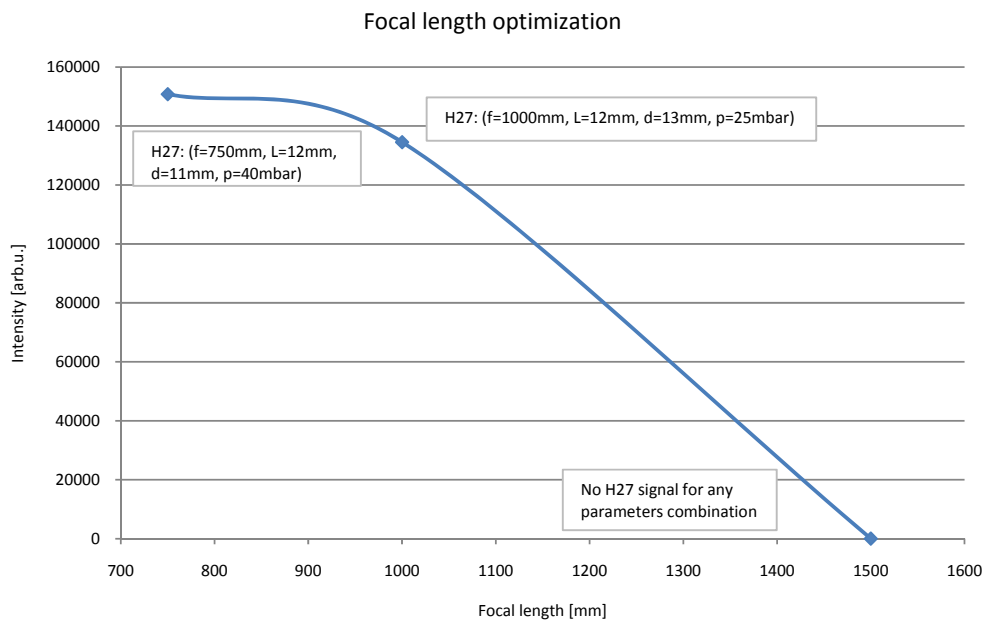
Typical dependence of the harmonic signal vs. the aperture size [34] was observed (e.g. Graph 4.24). For small iris opening (in this case below 9 mm) the signal is very low. Then, the signal rapidly raises and reaches its maximum (at 11 mm iris opening). Finally, a drop of the spectral intensity is observed. Out of the optimum, for higher beam sizes, the spectral intensity is preserved at moderate level and does not change any further.

#### 4.1.3 Focal length of the lens

Intensity of the driving beam in the interaction region is a very important factor since in HHG from gases it is desired to adjust intensity level in such a way so as to create favorable conditions for tunneling of most outer electrons of the atomic gas ( $\gamma \ll 1$ ). If the intensity is too low very low number of electrons will be tunnel-ionized

providing low contribution to XUV signal. On the other hand, if the intensity is too high very high density of the free electrons will be created. These electrons defocus NIR beam and become a source of de-phasing of NIR and XUV beams. Additionally, in the gas cell arrangement, for efficient HHG self-channeling is desired. It is achieved by the proper choice of intensity and the gas pressure leading to interplay between intensity-induced self focusing and free-electron-induced defocusing of the driving laser beam.

The experimental results on optimization of focal length for 27<sup>th</sup> harmonic order are presented in Graph 4.33. The detailed experimental conditions are presented in the insets of the graph. The strongest signal yield was recorded for  $f=750$  mm.



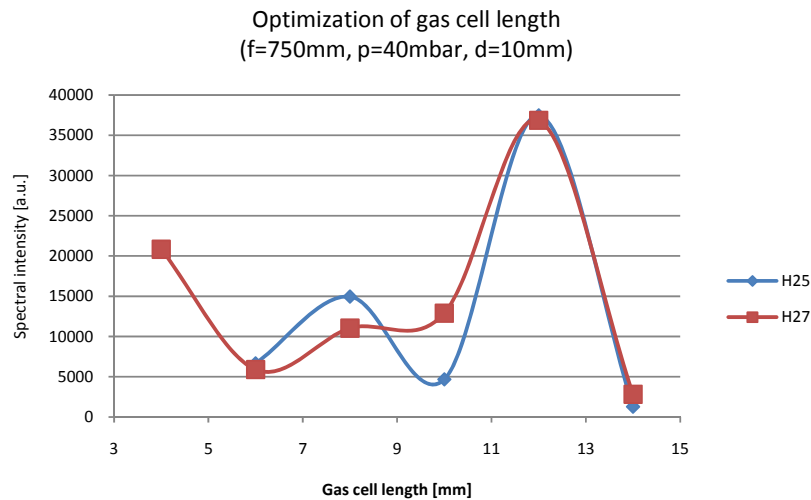
Graph 4.33. Optimization of the focal length of the lens in the HHG setup. The optimization has been performed for 27<sup>th</sup> harmonic order.

#### 4.1.4 Gas cell length

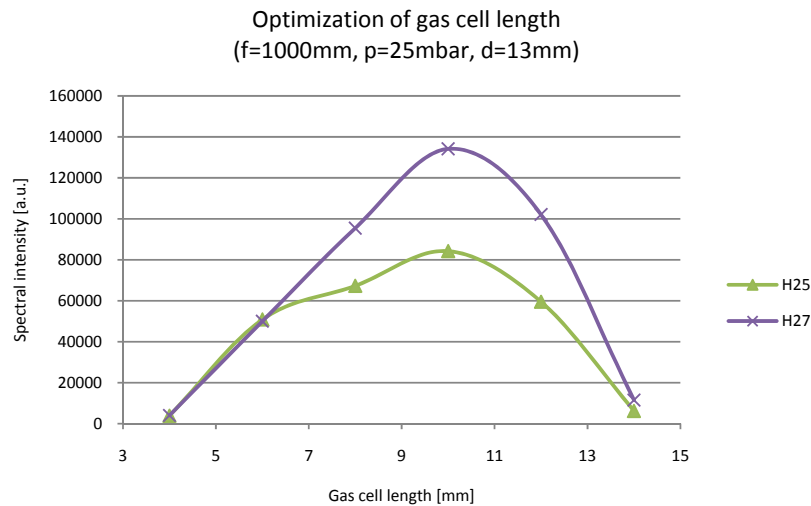
The optimization of the gas cell length aims at maximization of interaction length between the NIR beam and conversion medium up to the length values where signal decays due to re-absorption of the XUV radiation by neutral gas.

Moreover, tuning gas cell length at constant pressure of nonlinear medium allows investigation of effects limiting the efficiency which are not pressure dependent (phase matching) [34].

The measurement results are presented in Graph 4.34 and in Graph 4.35.



Graph 4.34. Optimization of gas cell length ( $f=750\text{ mm}$ ).



Graph 4.35. Optimization of gas cell length ( $f=1000\text{ mm}$ ).

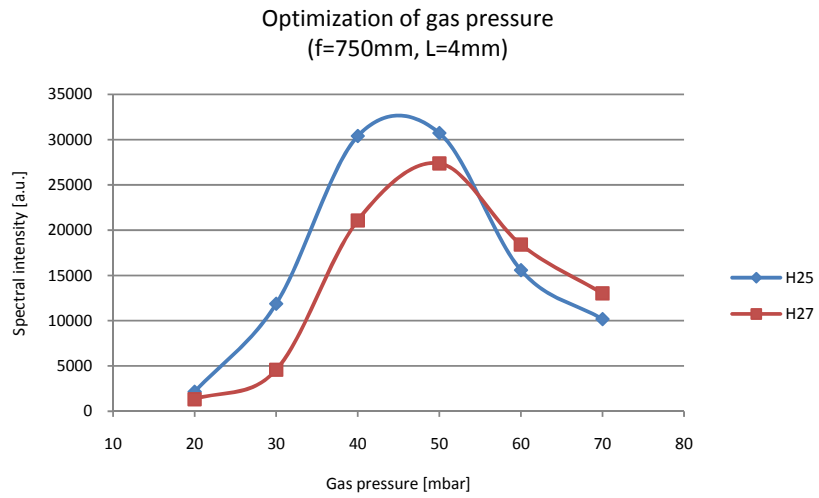
The curves feature shapes which well agree with the literature and exhibit typical optimal experimental conditions. The optimal gas cell length for  $f=750\text{ mm}$  was found to be  $12\text{ mm}$  while for  $f=1000\text{ mm}$   $10\text{ mm}$ . The discrepancy of the H27 signal yield in Graph

4.34 for  $L=4$  mm and for H25 with gas cell length of  $L=10$  mm is attributed to driving laser instability (the data were obtained in the long time interval of 1 month).

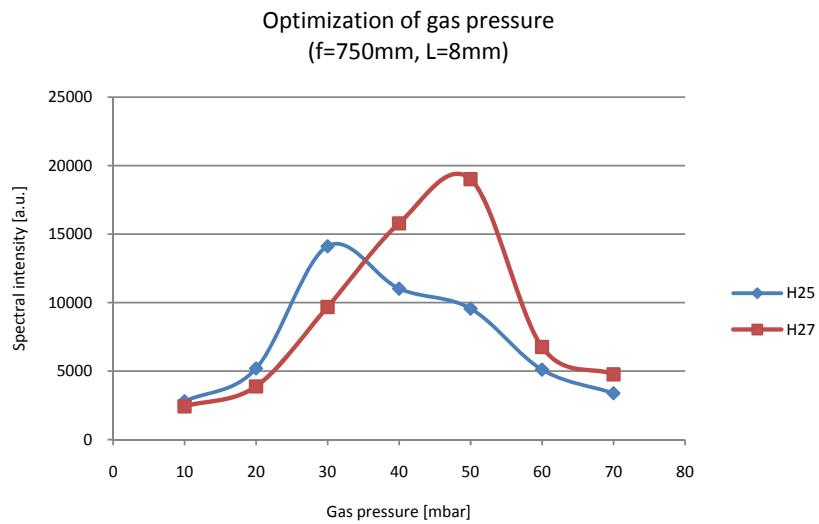
#### 4.1.5 Gas pressure

It has been experimentally confirmed [53] that intensity of  $m^{\text{th}}$  harmonic order is proportional to square root of atomic density ( $I_m \propto N^2$ ) accounting for the coherent character of HHG. On the other hand, it has to be noted that  $I_m \propto |F_m|^2$ , where  $F_m$  is so called phase matching factor rapidly decreasing with  $m$  [34]. This is the reason of rapid decrease of spectral intensities in the long-wavelength part of the harmonic spectrum. Thus a proper choice of the gas pressure is crucial for the efficient process of high-order harmonic generation.

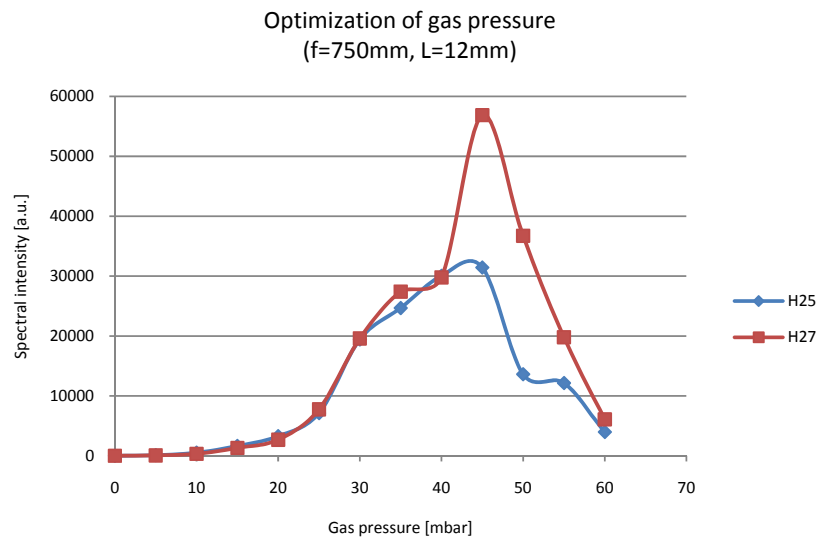
The selected experimental results are presented in Graph 4.36 - Graph 4.45. The optimal pressure for lens  $f=750$  mm was  $\sim 45$  mbar, for  $f=1000$  mm was  $\sim 25$  mbar, and for  $f=1500$  mm was  $\sim 10$  mbar. The shift of optimal pressure to lower values when increasing focal length of the lens can be attributed to the increasing phase mismatch factor and reduced intensity in the interaction region. The dependence of the spectral intensity vs. pressure is typical and does not present any discrepancies between results known from the literature.



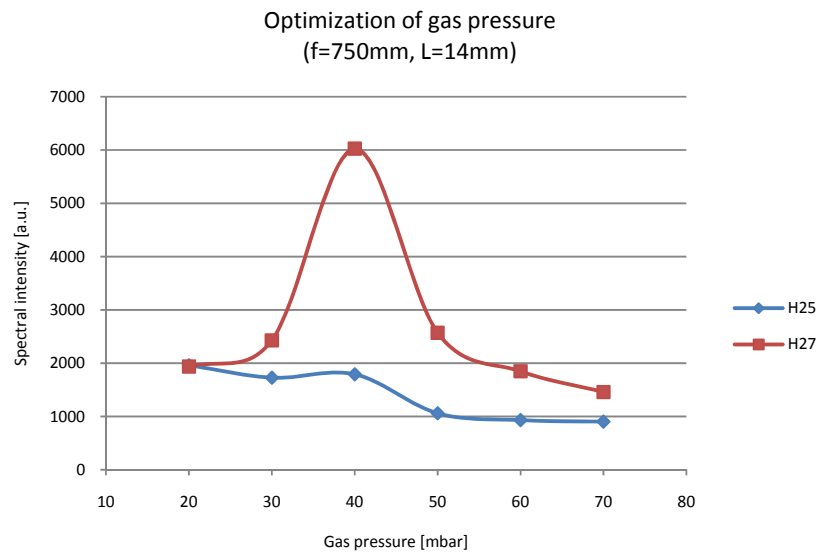
Graph 4.36. Optimization of gas pressure (Ar).



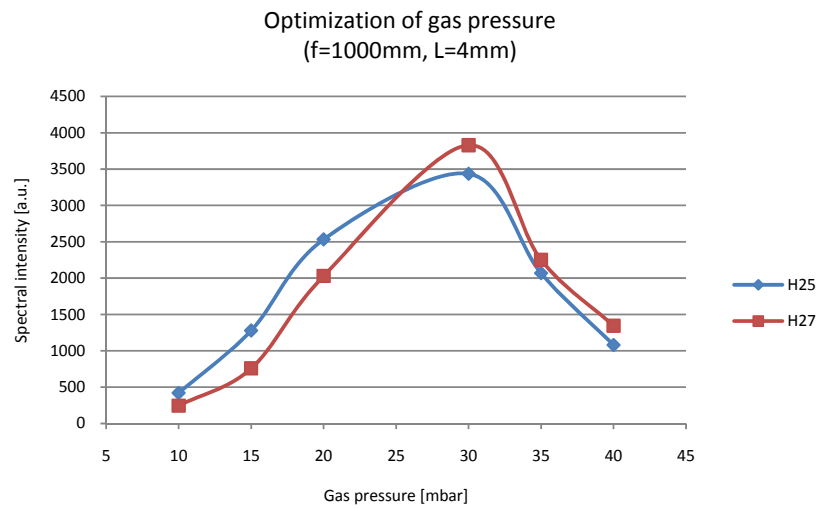
Graph 4.37. Optimization of gas pressure (Ar).



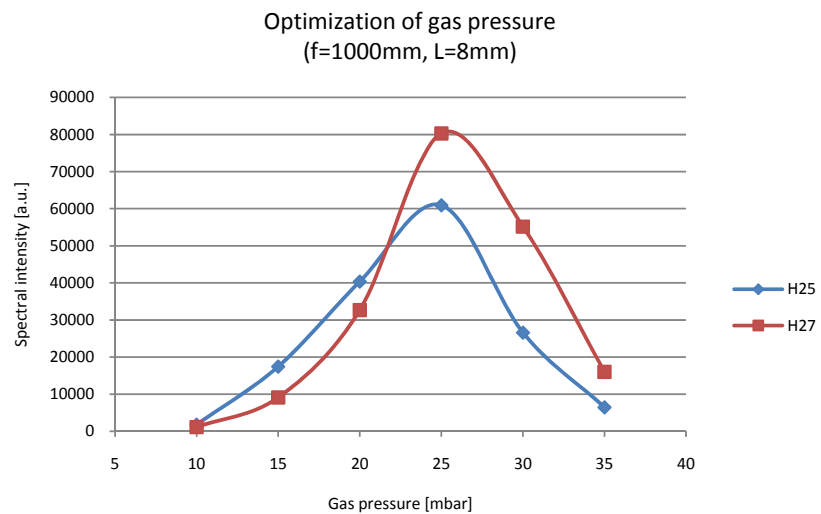
Graph 4.38. Optimization of gas pressure (Ar).



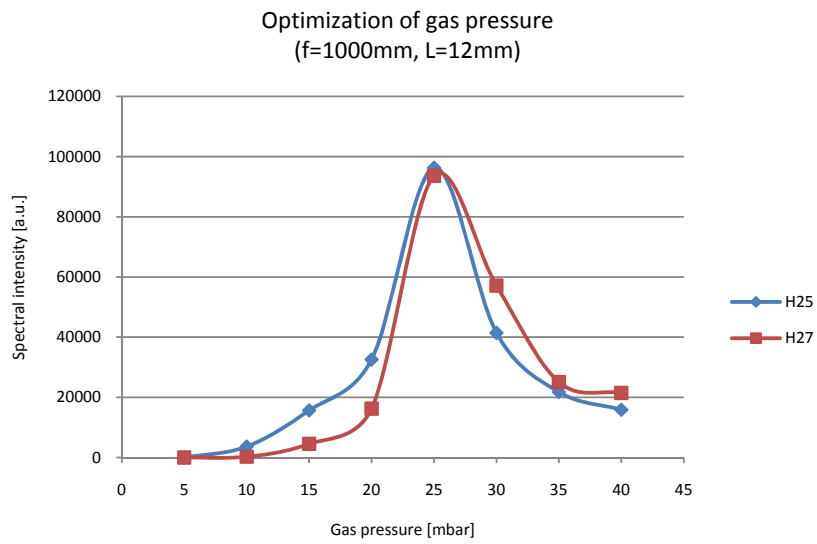
Graph 4.39. Optimization of gas pressure (Ar).



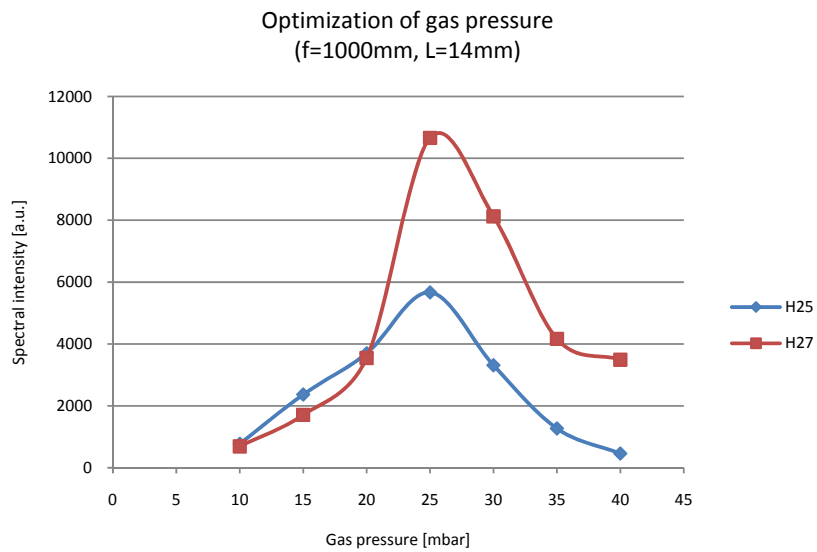
Graph 4.40. Optimization of gas pressure (Ar).



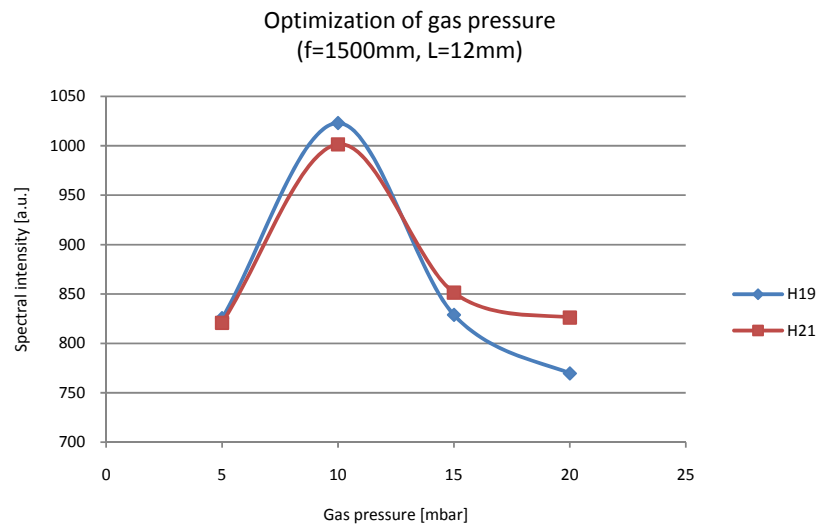
Graph 4.41. Optimization of gas pressure (Ar).



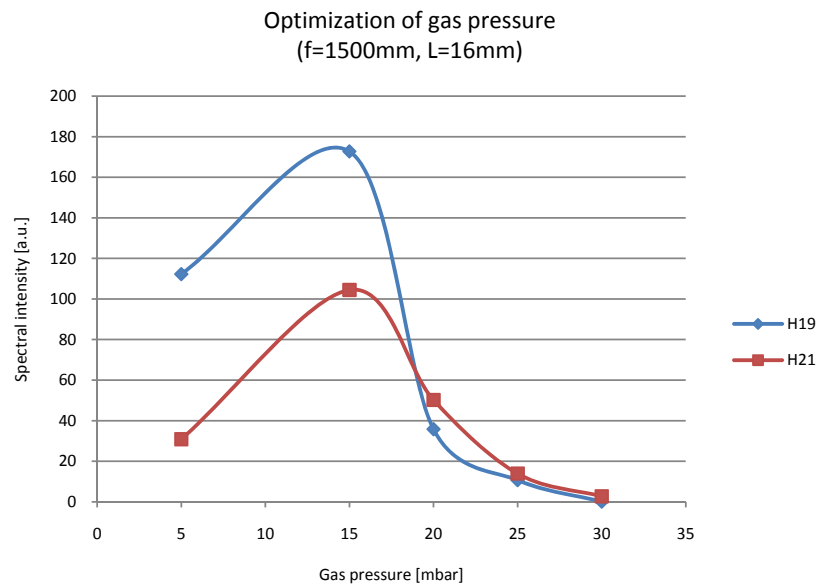
Graph 4.42. Optimization of gas pressure (Ar).



Graph 4.43. Optimization of gas pressure (Ar).



Graph 4.44. Optimization of gas pressure (Ar).



Graph 4.45. Optimization of gas pressure (Ar).

#### 4.1.6 Cell position

The optimization of the position of the gas cell along the driving beam caustics was performed in order to minimize geometrical component of phase mismatch vector. The geometry of the experiment is presented in Figure 4.1. The "0" position of the motorized stage for  $f=750\text{ mm}$  and  $1000\text{ mm}$  corresponds to the beam waist location

close to the entrance to the cell. For 1500 mm beam waist was aligned to be located at the back face of the cell (due to the setup realignment).

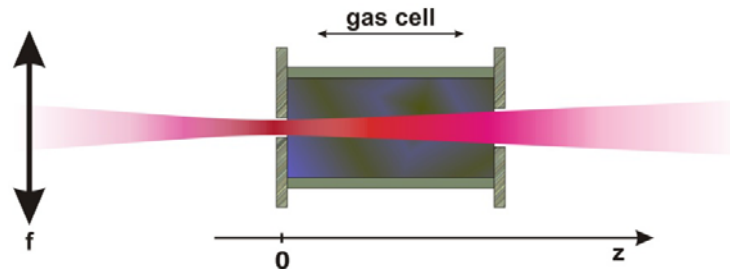
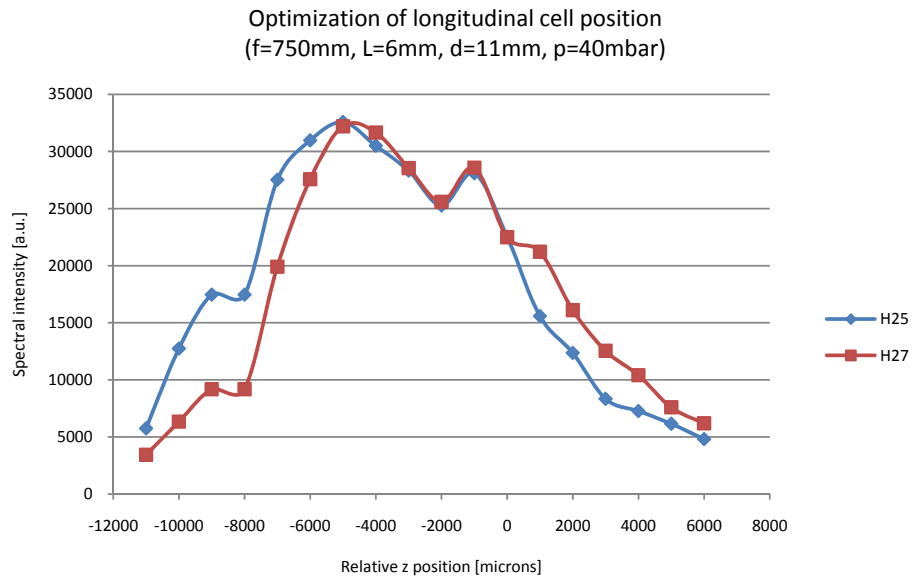


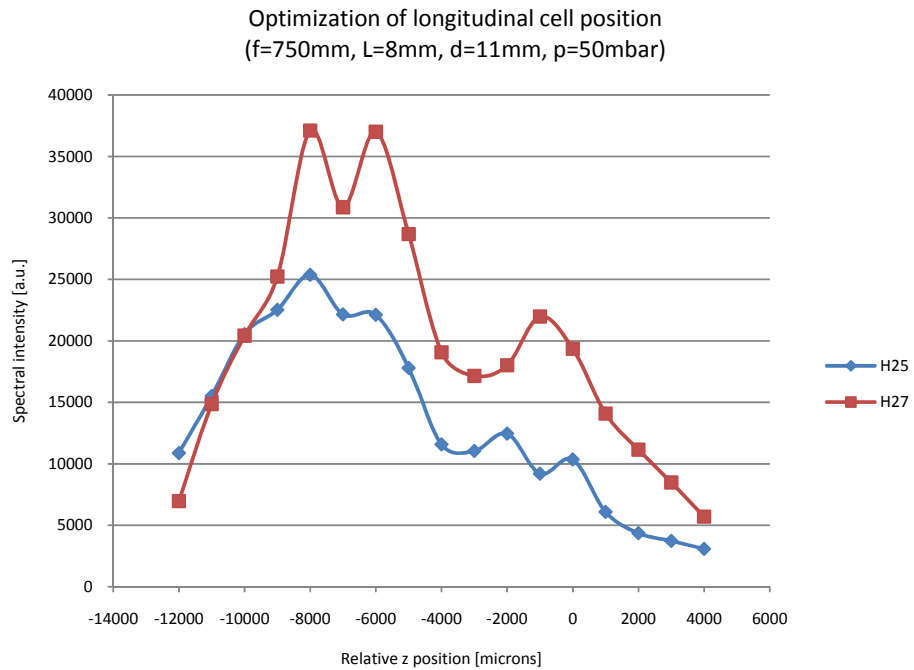
Figure 4.1. Geometry of optimization of the position of the gas cell along beam propagation path. "0" position of the motorized stage corresponds to the beam waist location close to entrance to the cell.

The experimental results are presented in Graph 4.46 - Graph 4.54. Experimental conditions are embedded in the graphs.

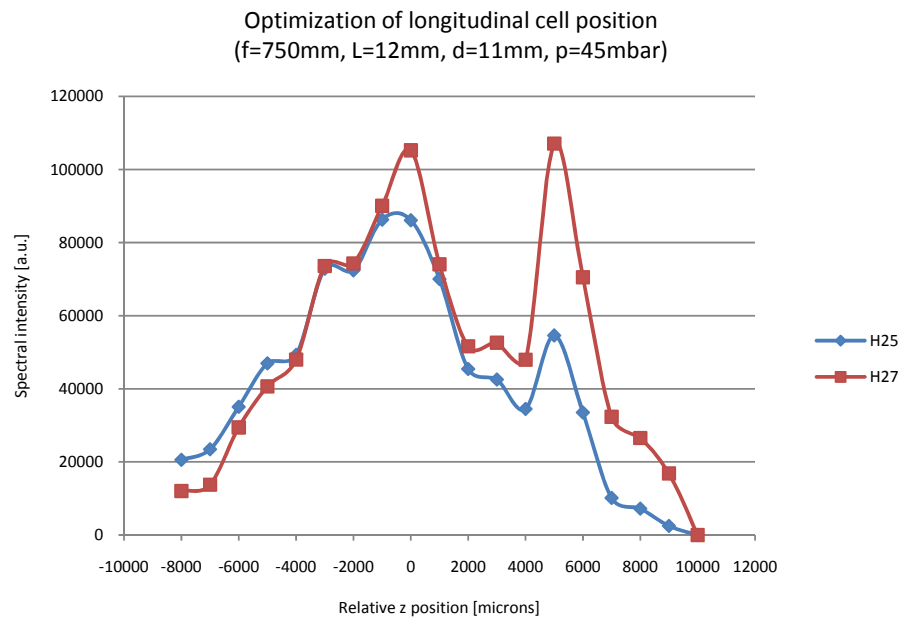
It could be observed that in general two maxima exist: when beam waist was close to both ends of the cell. However, the more favorable conditions are with focus located at the end face of the cell.



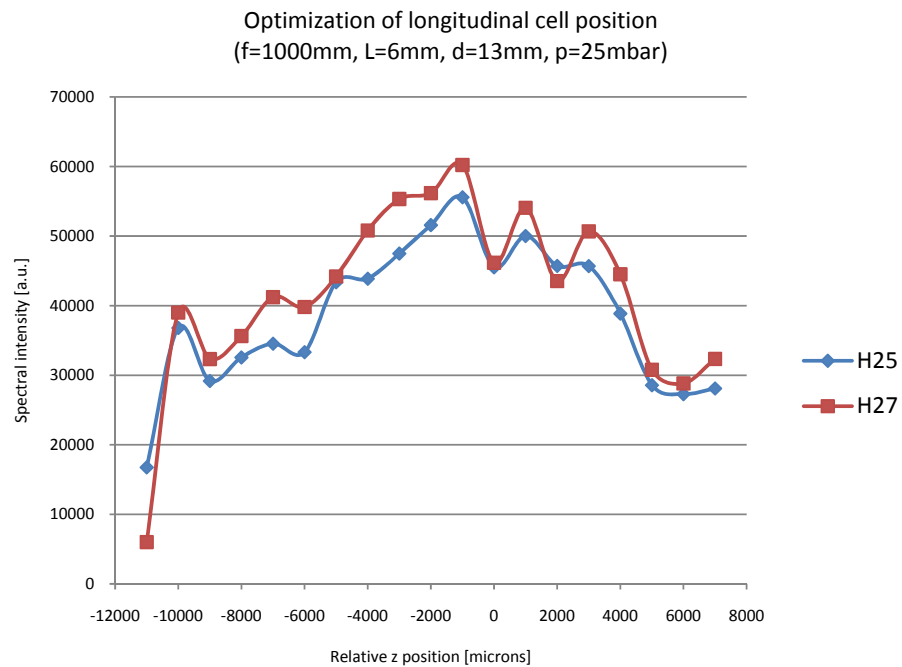
Graph 4.46. Optimization of longitudinal gas cell position.



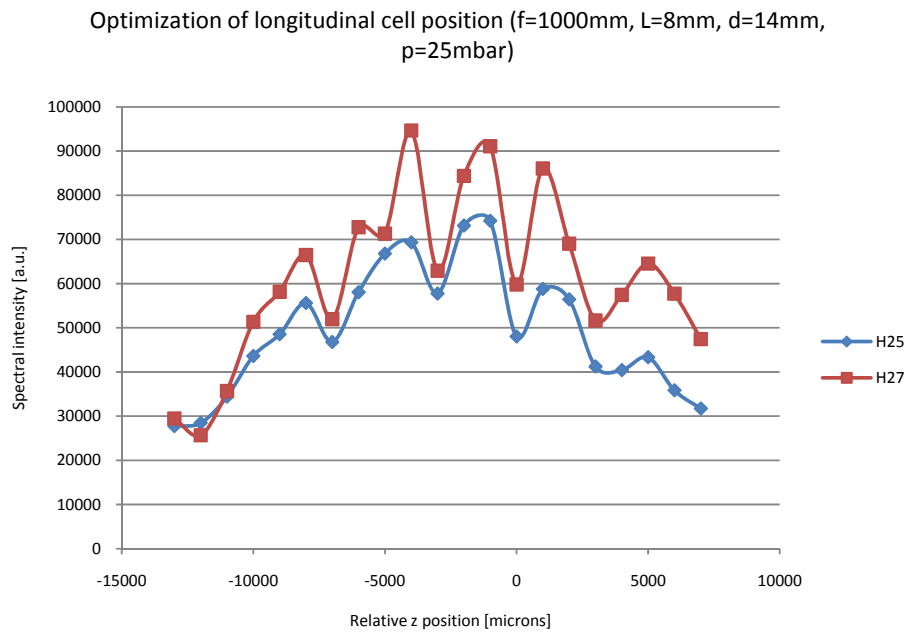
Graph 4.47. Optimization of longitudinal gas cell position.



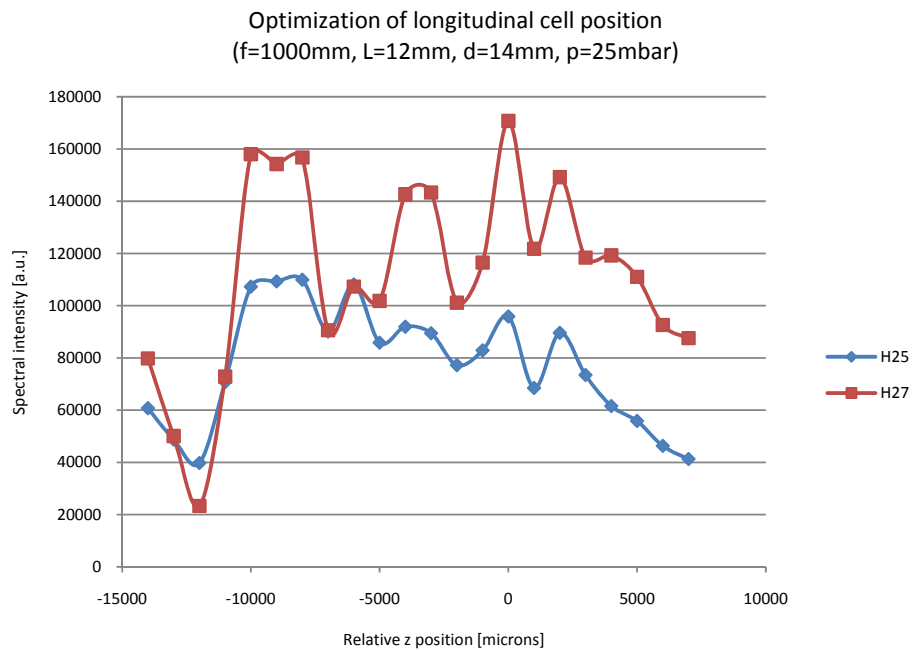
Graph 4.48. Optimization of longitudinal gas cell position.



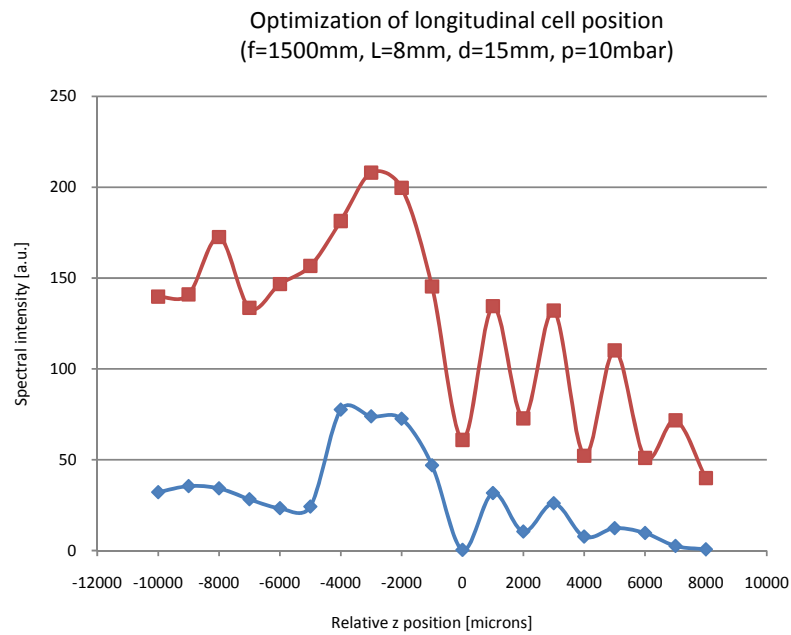
Graph 4.49. Optimization of longitudinal gas cell position.



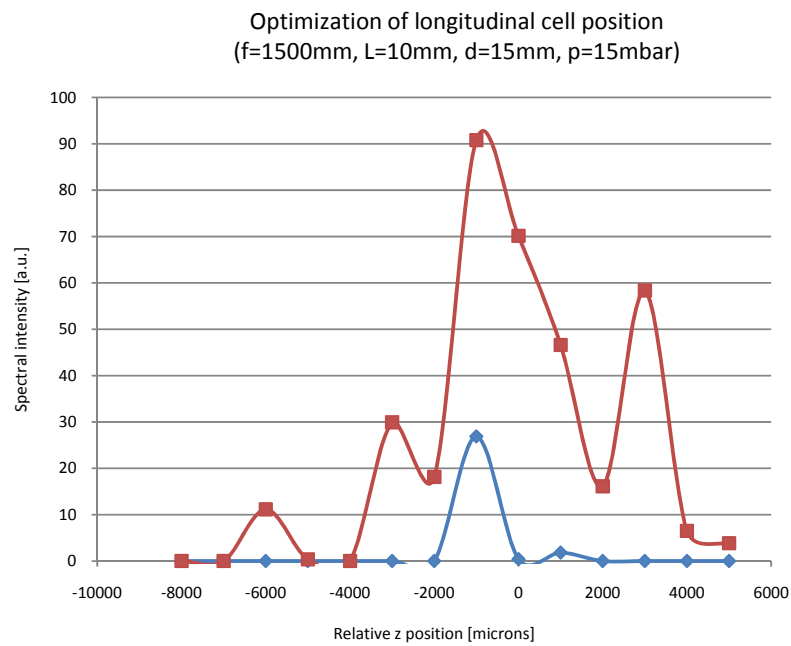
Graph 4.50. Optimization of longitudinal gas cell position.



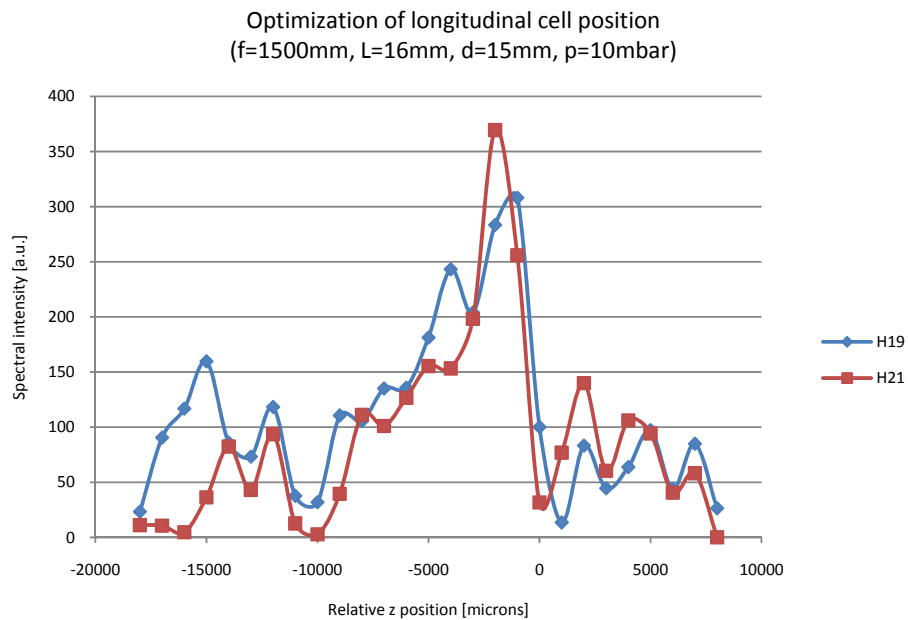
Graph 4.51. Optimization of longitudinal gas cell position.



Graph 4.52. Optimization of longitudinal gas cell position.



Graph 4.53. Optimization of longitudinal gas cell position.



Graph 4.54. Optimization of longitudinal gas cell position.

A very interesting feature of the obtained results is the oscillatory shape of spectral intensity. The intensity fringes are related to coherence length which defines the distance over which the harmonic signal can build-up constructively. If the conversion medium becomes longer than coherence length ( $l_{coh}$ ), destructive interferences occur and lead to appearance of fringes, also called Maker fringes [54], which are a direct means to investigate coherent effects during HHG process.

Maker fringes from harmonic radiation of orders up to 13<sup>th</sup> were firstly reported by L'Huillier et al. The experimental setup involved 40-ps, Nd:YAG laser system [55]. The beam was focused ( $f=200\text{ mm}$ ) into a xenon gas jet. The gas jet position was scanned. Later, Maker fringes were obtained using a Ti:sapphire laser system and an Ar-filled gas cell by Kazamias et al. [56], [57]. The latter referenced results were obtained in a very similar experimental setup as at the IoP/PALS; however, in the referenced case gas cell length was varied while in the reported results most prominent (but not exclusive) modulations were obtained during the cell position scan. For example, the fringes contrast in Graph 4.52 is  $\sim 37.7\%$  and  $l_{coh} = 2\text{mm}$ .

## 4.2 HHG beam profile

The experimental setup for the measurement of beam profile of the optimized harmonic source is shown in Figure 4.2. The experimental conditions were: diameter of the aperture limiting the IR beam size  $d=11$  mm, focal length of the lens in the setup  $f=750$  mm, gas cell length  $L=12$  mm, gas pressure (Ar)  $p=45$  mbar, and the laser parameters were:  $\Delta t=35$  fs,  $\lambda_c=810$  nm, 1.2 mJ at 91 Hz. Integration time was 3 s. The measurement was performed using Andor DX440-DN X-ray CCD camera. The distance between Andor camera and the front face of the gas cell was 2157 mm. 400 nm Al filter (Luxel) was placed in front of the camera.

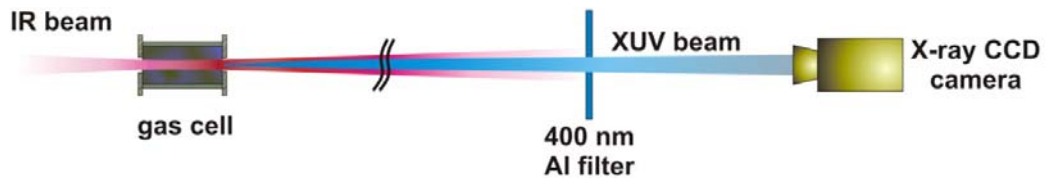


Figure 4.2. Experimental setup of the harmonic beam profile measurements.

The beam footprint is shown in Graph 4.55 and in Graph 4.56. For both profiles Gaussian fit was done with fit coefficient higher than 99 % in both directions (detailed fitting results are embedded in the graphs). The beam size at the distance given by camera position was (FWHM) 2.86 mm and 2.49 mm in horizontal and vertical directions, respectively.

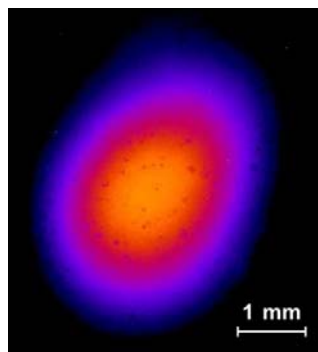


Figure 4.3. High-order harmonic beam profile.

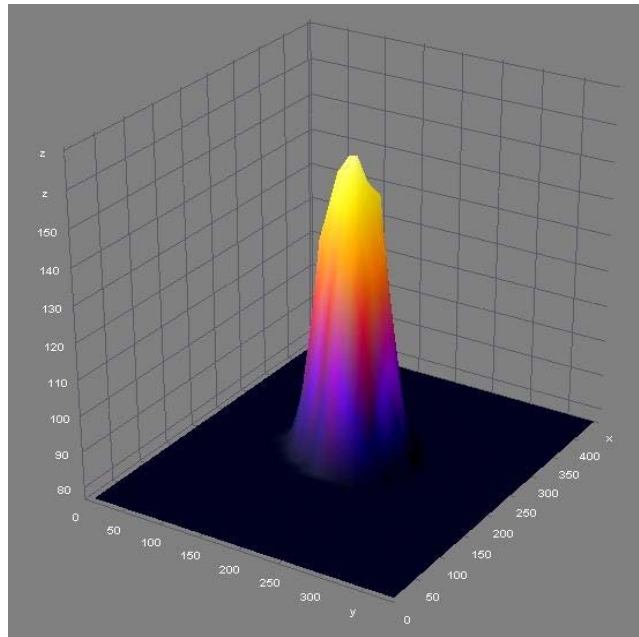
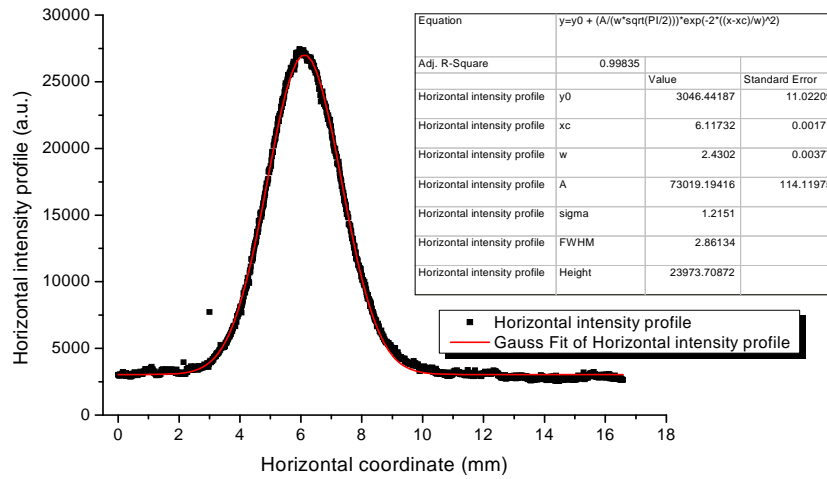


Figure 4.4. 3D beam profile plot.

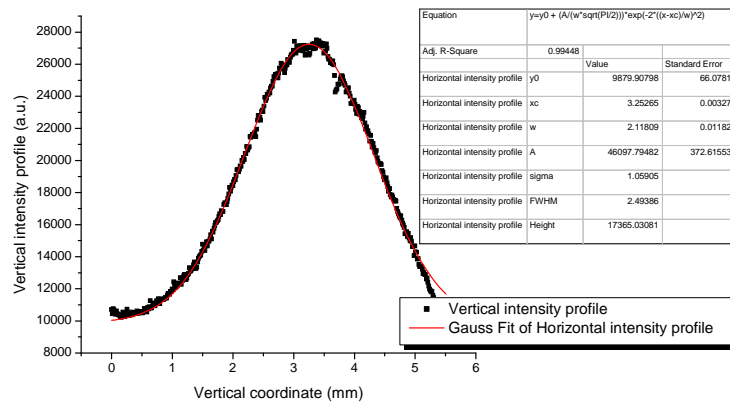
The beam profile is very close to perfect Gaussian shape. The intensity changes very smoothly and does not feature any significant asymmetry or non-uniformities like in a case most of X-ray lasers (c.f. Ne-like Zn soft XRL [48] or capillary discharge soft XRL [58]). The spots visible Figure 4.3 are attributed to impurities in the beam path (most probably on the phosphor layer).

Profile of the harmonic beam in the horizontal direction



Graph 4.55. Harmonic beam profile in the horizontal direction together with its Gaussian fit. The beam width (FWHM) is 2.86 mm.

Profile of the harmonic beam in the vertical direction



Graph 4.56. Harmonic beam profile in the vertical direction together with its Gaussian fit. The beam width (FWHM) is 2.49 mm.

### 4.3 $M^2$ of HHG beam

One of the crucial parameters defining the beam quality is  $M^2$  factor (also called *beam quality factor* or *beam propagation factor*). According to ISO 11146 Standard it is defined as [59]:

$$M^2 = \Theta \cdot w_0 \cdot \frac{\pi}{\lambda}$$

Eq. 4.3

Where:  $\Theta$  is far-field beam divergence half-angle,  $w_0$  – beam waist radius, and  $\lambda$  – is the radiation wavelength. If the beam intensity distribution pattern is elliptical  $M^2$  factor is usually estimated along major and minor axes of the ellipse resulting in two values of  $M^2$  parameter:  $M_x^2$  and  $M_y^2$ .

The measurement of  $M^2$  of the XUV harmonic beam was performed in the standard scheme when caustic of focused beam is measured. In laser physics, when  $M^2$  is measured in optical spectral range the beam is focused by a high-quality lens of long focal length and large  $F^\#$ . The size of the beam waist should roughly match the size of the detector array [60]. Here, instead of transmission optics, reflective optics was used. In the experimental setup the NIR beam was filtered out by 400 nm Al filter (Luxel) and the XUV beam was focused by a spherical multilayer (ML) C/Si mirror ( $R=30\%$  at 30 nm,  $\beta=6^\circ$ ,  $f=250$  mm,  $N=20$ ,  $d=16.6$  nm) which has been designed at the Institute of Physics in Prague (Graph 4.57), and prototyped at the Institute of Scientific Instruments in Brno.

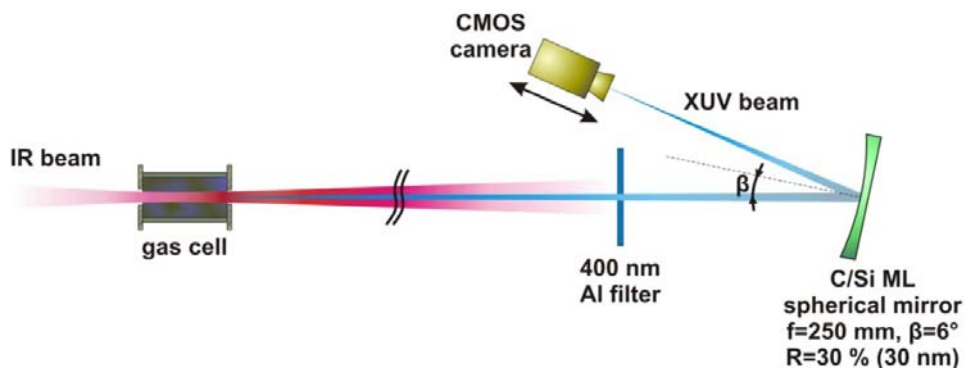
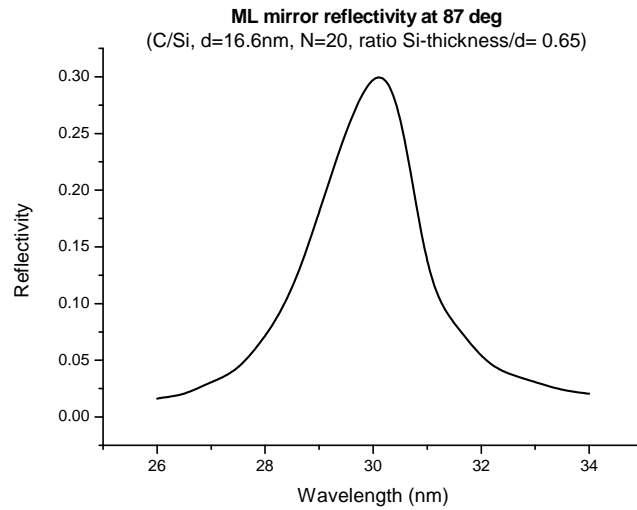


Figure 4.5. Experimental setup for measurement of  $M^2$  parameter of high-order harmonic beam.



Graph 4.57. Simulated reflectivity of the multilayer mirror used in the experiment [61].

Distance from the gas cell back end to the ML mirror was 2295 mm. The caustics was directly measured with a CMOS PixelINK camera (Section 3.3). The initial "0" position of the camera was at the distance of  $\sim 280$  mm from the mirror along beam propagation path. Signal acquisition time was 50 ms. The camera relative position was varied from -12.5 mm to +12.5 mm with a step of 0.5 mm. Positive values in the camera position coordinate mean moving away from focusing ML mirror. The experimental conditions for the HHG source were: Ar pressure  $p=45$  mbar, NIR beam aperture diameter  $d=11$  mm, gas cell length  $L=12$  mm, focal length of the lens  $f=750$  mm, and driving beam parameters:  $\lambda_c=810$  nm,  $\Delta t=35$  fs,  $E=1.2$  mJ at repetition rate of 1 kHz.

The examples of the beam footprints are presented in Figure 4.6 - Figure 4.15. All images are of the same dimension of 264 x 354 pixels (1.769 x 2.372 mm ).

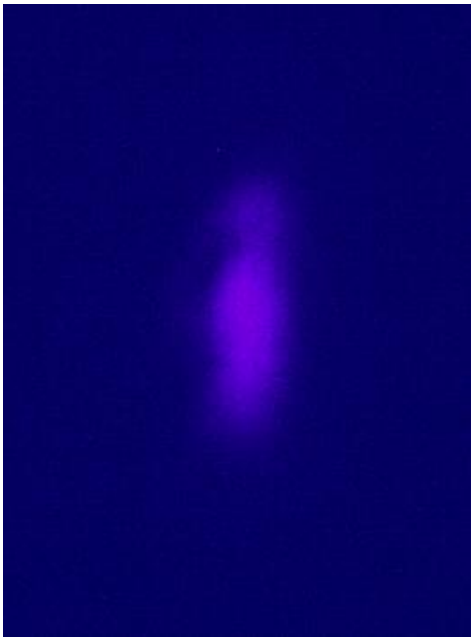


Figure 4.6. XUV beam profile at relative position along beam propagation direction: -12 mm (FWHM size: 281 x 871  $\mu\text{m}$ ).

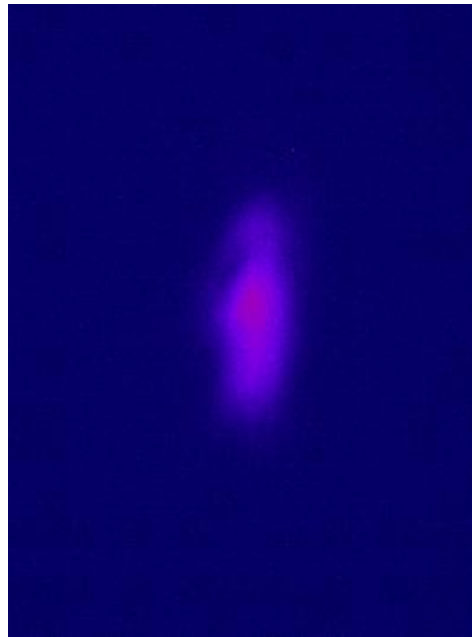


Figure 4.7. XUV beam profile at relative position along beam propagation direction: -9 mm (FWHM size: 288 x 703  $\mu\text{m}$ ).

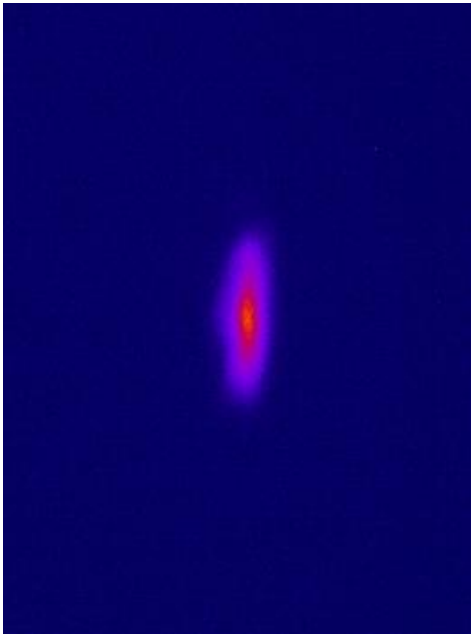


Figure 4.8. XUV beam profile at relative position along beam propagation direction: -5 mm (FWHM size: 100 x 382  $\mu\text{m}$ ).

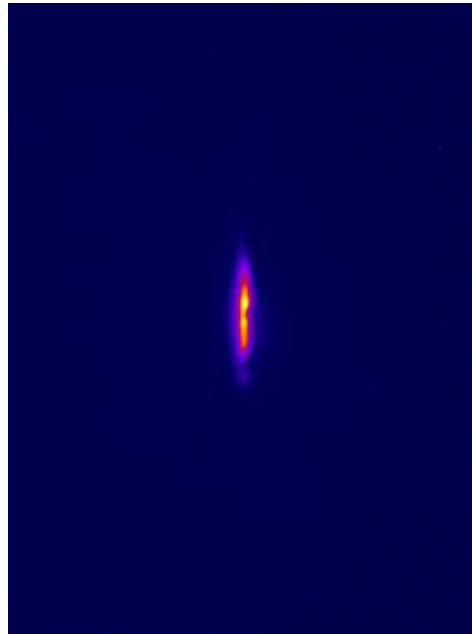


Figure 4.9. XUV beam profile at relative position along beam propagation direction: -2 mm (FWHM size: 34 x 221  $\mu\text{m}$ ).

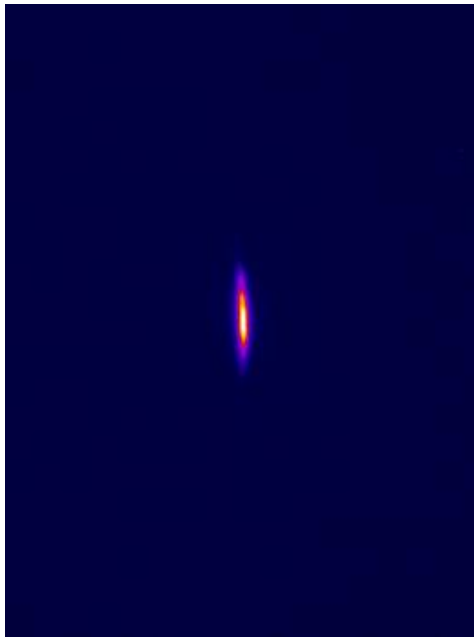


Figure 4.10. XUV beam profile at relative position along beam propagation direction: -1 mm (FWHM size: 27 x 161  $\mu\text{m}$ ). Sagittal focus position.

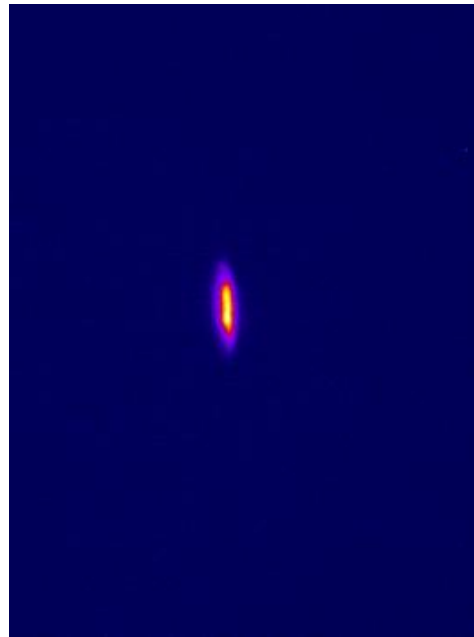


Figure 4.11. XUV beam profile at relative position along beam propagation direction: 0 mm (FWHM size: 40 x 154  $\mu\text{m}$ ).

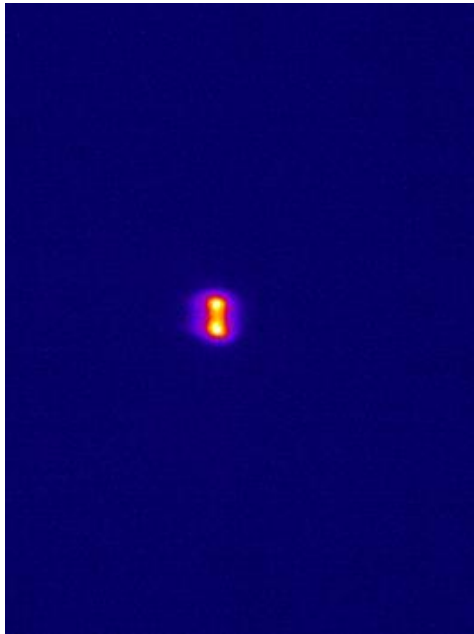


Figure 4.12. XUV beam profile at relative position along beam propagation direction: +2 mm (FWHM size: 67 x 141  $\mu\text{m}$ ).

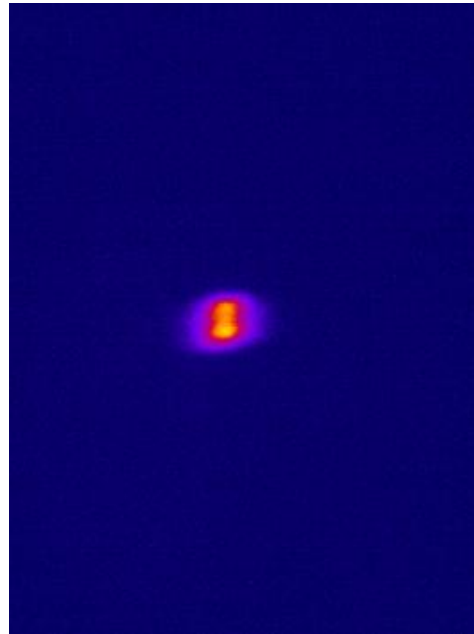


Figure 4.13. XUV beam profile at relative position along beam propagation direction: +4 mm (FWHM size: 107 x 147  $\mu\text{m}$ ).

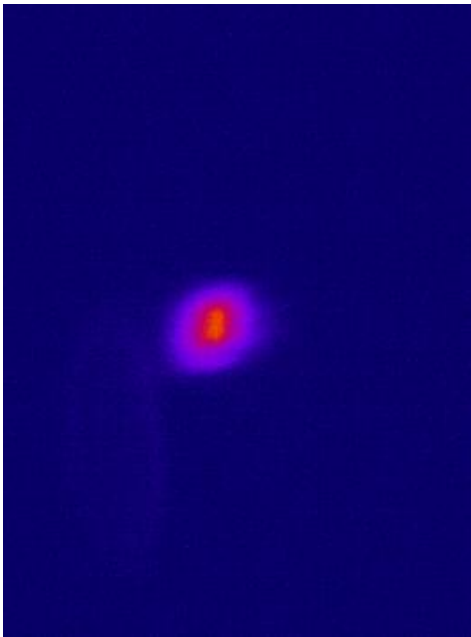


Figure 4.14. XUV beam profile at relative position along beam propagation direction: +6 mm (FWHM size: 194 x 201  $\mu\text{m}$ ).

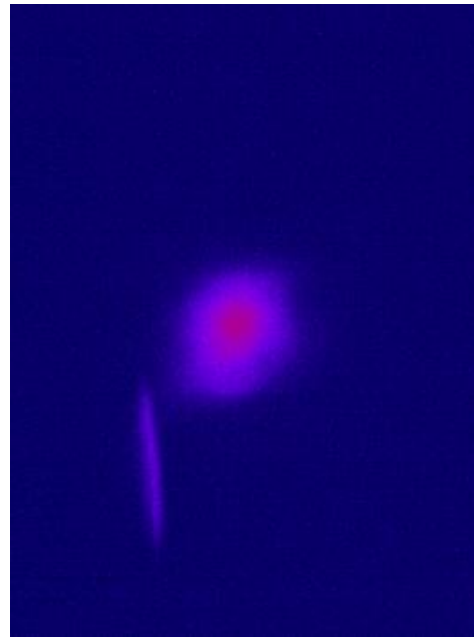
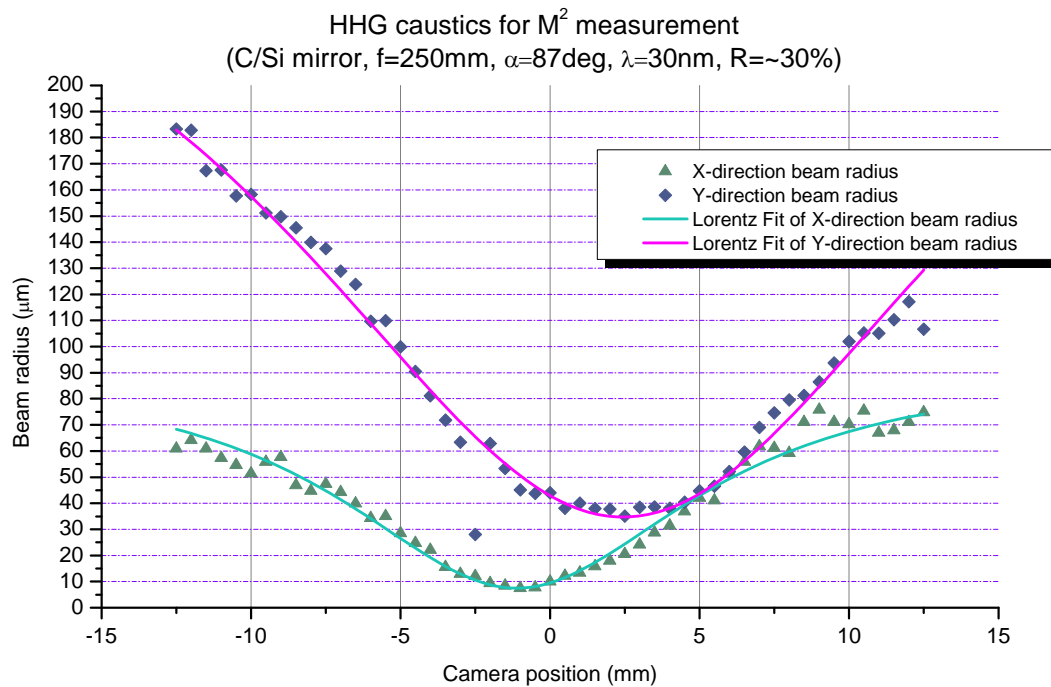


Figure 4.15. XUV beam profile at relative position along beam propagation direction: +9 mm. Visible artifact is probably due to a parasitic reflection (FWHM size: 395 x 415  $\mu\text{m}$ ).

During the scan astigmatism typical for off-axis imaging using spherical mirrors was observed. Transversal asymmetry of the caustics is clearly visible in the presented figures. The beam profiles were taken along minor and major ellipse axes. They were denoted as X and Y, respectively. The profiles were approximated using Gaussian fit and FWHM beam size was estimated based on computed curve. The processing was done in the Origin software [62]. The beam with estimation error never exceeded 2 %. The resulting caustics for both directions are shown in Graph 4.58. The estimated values of beam quality factor for central wavelength of 30 nm were:  $M_x^2 = 4.64$  and  $M_y^2 = 38.45$ . Values of  $M^2$  factor greater than 3 are typical for multimode beams thus recalling the results of the measurements of the beam profile it is assessed that these poor values of  $M_x^2$  and  $M_y^2$  do not reflect the beam quality but rather low grade of the focusing optics which distorts the beam. The claim may be supported by the observation of minor longitudinal asymmetry in the beam caustics in both X and Y directions and a very strong astigmatism effect which is exhibited in Graph 4.59.



Graph 4.58. The caustics scan of the focused HHG beam. The distance between tangential and sagittal foci was  $\sim 3.495$  mm.

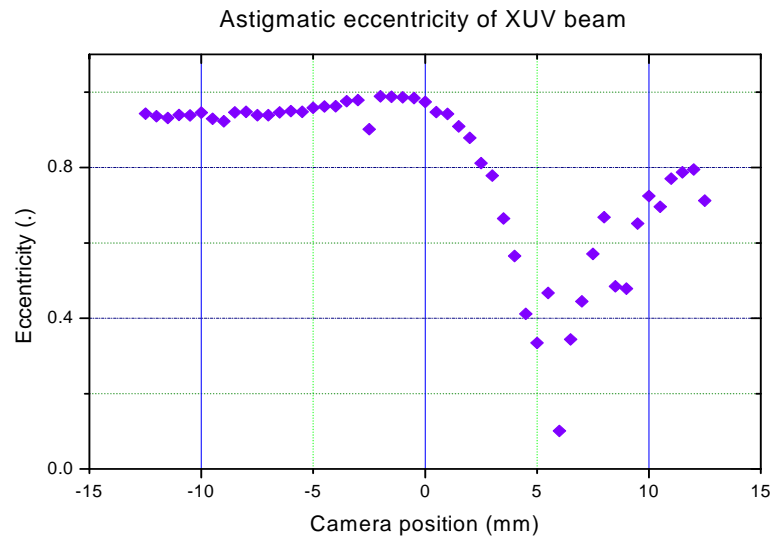
Dependence of eccentricity  $\varepsilon$  defined as:

$$\varepsilon = \sqrt{1 - \left(\frac{\Delta X}{\Delta Y}\right)^2}$$

Eq. 4.4

where:  $\Delta X$  and  $\Delta Y$  is beam width along minor and major axes of the ellipse, respectively, was plotted as a function of the camera position along beam propagation direction.

To estimate intensity of XUV beam in the focal spot let us assume a focus of the shape shown in Figure 4.10 (assessed as smallest observed). The absolute focus area is  $3.412 \cdot 10^{-5} \text{ cm}^2$ . If harmonic beam energy is  $\sim 0.652$  nJ (see Section 4.5) and average reflectivity of the multilayer mirror of 25 % in vicinity of 30 nm the resulting XUV (all harmonic orders) fluence in the focus will be  $4.78 \cdot 10^{-6} \text{ J/cm}^2$ . If EVU pulse is assumed to be of duration of 35 fs the intensity in the focus would be  $1.37 \cdot 10^8 \text{ W/cm}^2$ .



Graph 4.59. Eccentricity of the XUV beam due to focusing by spherical mirror.

The obtained fluence in the focus is not sufficient for numerous practical applications of the source. The increase of the fluence in the focus could be achieved by employment of a multilayer optics of different shape featuring lower aberrations (especially spherical aberration) for off-axis imaging. As an example paraboloidal mirrors could be used since they are capable of creating a perfect on-axis image of an infinitely distant object. For practical reasons off-axis paraboloidal mirrors are used, being, in fact, only a section of a much greater, so called, “parent” on-axis parabola. To increase reflectivity in EUV spectral region of such mirrors and to achieve monochromatization of the harmonic radiation such mirrors are covered with multilayer structures. On the other hand, a very straightforward solution is to use spherical focusing mirror and to place an irradiated sample neither in sagittal nor in tangential focus but at the position of the circle of least confusion. To present this effect qualitative simulation of harmonic beamline was performed in Zemax [63]. Figure 4.16 presents simulations of a focal spot on the plane 280 mm distant from focusing mirror.

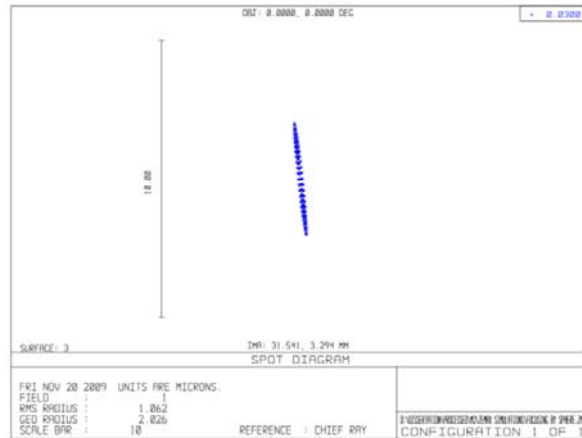


Figure 4.16. Simulation of focal spot of XUV beam focused by a spherical mirror in the exactly same setup as in the experiment. The observation plane is at distance of 280 mm from the mirror (reference to Figure 4.11).

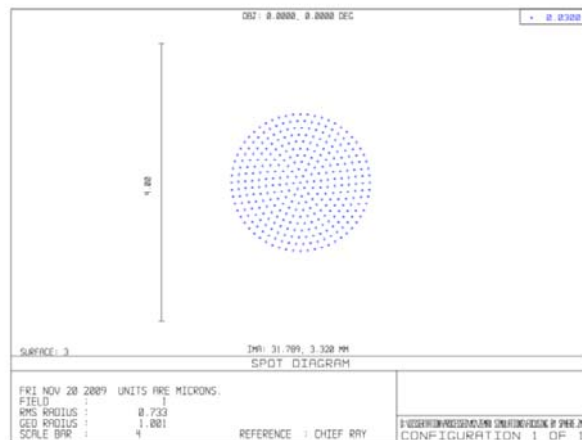


Figure 4.17. Simulation of the circle of least confusion which, in the setup, is located  $\sim 269$  mm from the focusing mirror. Note difference in scale bar between the both figures.

Figure 4.17 presents ray tracing results at the position of a circle of least confusion. The focal spot area in this case is  $3.14 \cdot 10^{-8} \text{cm}^2$ . This will result in fluence of  $5.2 \cdot 10^{-3} \text{J/cm}^2$ . The focal spot in Figure 4.16 has area of  $7.58 \cdot 10^{-8} \text{cm}^2$ , thus fluence in this case would be  $2.2 \cdot 10^{-3} \text{J/cm}^2$ . Hence the increase when moving with observation plane from position 280 mm to 269 mm leads to 2.36-fold increase in fluence. If we assume the same relation in the experiment, moving from sagittal focus to circle of least confusion position would provide with  $1.13 \cdot 10^{-5} \text{J/cm}^2$ . The discrepancy between the

focus size in the experiment and in the simulation is attributed to: 1) imperfections in the manufacturing process, 2) the simulated XUV beam is perfectly collimated while the real beam has slight divergence ( $\sim 0.4$  mrad).

#### 4.4 HHG beam spatial coherence

The estimation of the HHG beam spatial coherence for optimized HHG source was performed in double-slit Young experiment. The experimental setup is shown in Figure 4.19. The NIR beam ( $\lambda_c=810$  nm,  $\Delta t=35$  fs,  $E=1.2$  mJ, 1 kHz and size of 11 mm) was focused by a lens ( $f=750$  mm; not visible in the figure). High-order harmonics were generated in a gas cell (Ar,  $p=45$  mbar,  $L=12$  mm). The longitudinal position of the cell was optimized to maximize XUV total signal (focus in vicinity of the back face of the cell). 400 nm Al filter was used (Luxel) and was proceeded by a Ni foil with a set of pairs of slits. 400 nm Al filter was used (Luxel) and was proceeded by a Ni foil with a set of pairs of

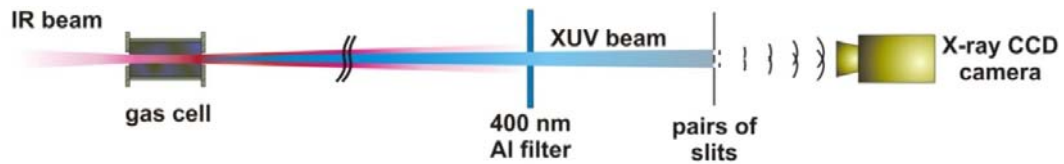


Figure 4.19. Experimental setup for measurement of spatial coherence of high-order harmonic beam.

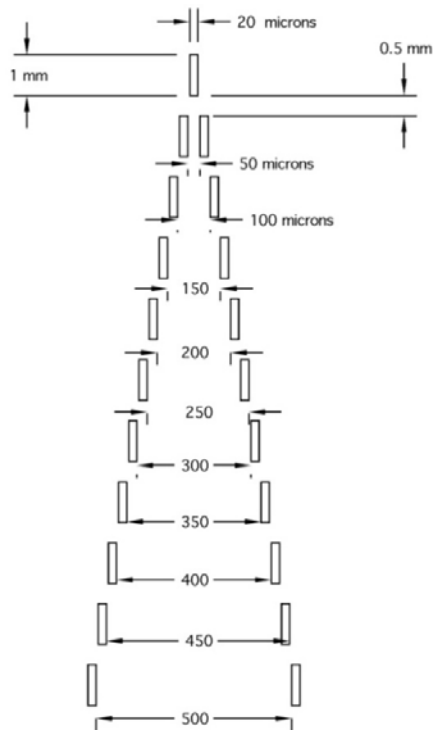


Figure 4.18. Scheme of the slits used in the experiment [64].

slits (Optimask S.A.; Figure 4.18). The pairs were 20  $\mu\text{m}$  wide and 1 mm high. The separation between the slits ranged from 0 (one slit) to 500  $\mu\text{m}$  with a step of 50  $\mu\text{m}$  allowing precise scan all across the XUV beam. The interference fringes were recorded with the Andor X-ray CCD camera (see Section 3.3). The distance between front face of the cell and the slits was 1560 mm, while distance between slits and CCD camera was 597 mm. The position of the HHG beam was centered between a pair of slits actually used in the experiment. The beam size (FWHM) on the camera was  $\sim 2.86$  mm and 2.49 mm in vertical and horizontal directions, respectively.

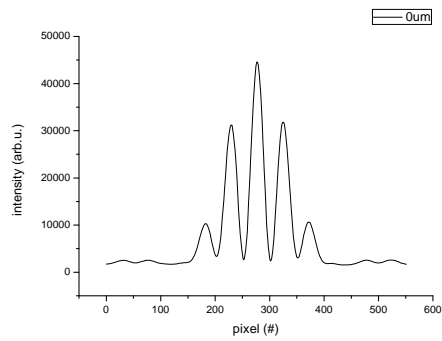
Examples of the interference fringes recorded in the measurement are shown in Graph 4.60 - Graph 4.67.

Fringes visibility defined as:

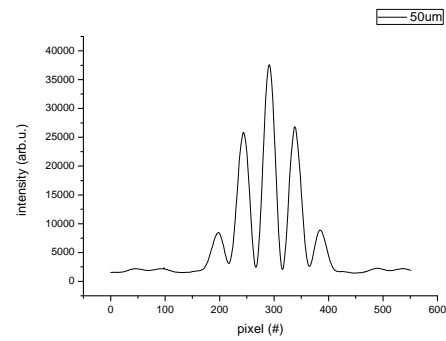
$$\mu = \frac{I_{\max} - I_{\min}}{I_{\max} + I_{\min}}$$

Eq. 4.5

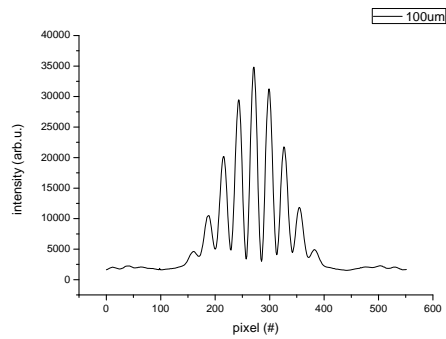
as a function of distance between slits was plotted (Graph 4.68), where,  $I_{\max}$  is a peak intensity and  $I_{\min}$  is a minimum intensity value in the interference pattern. The visibility of the fringes is highest (above 90 %) for inner part of the beam of diameter  $\sim 120$   $\mu\text{m}$ , while 50 % drop of intensity was observed for diameter of  $\sim 200$   $\mu\text{m}$ . Since the maximum slits separation is smaller than the total beam diameter it is only possible to claim that according to commonly used criterion of  $1/e^2$  the harmonic beam is fully coherent for diameter not smaller than 500  $\mu\text{m}$  (for 500  $\mu\text{m}$  distant slits  $\mu=29.4$  %). It was not possible to match the beam size and the maximum slits separation in the setup due to limits of the vacuum system.



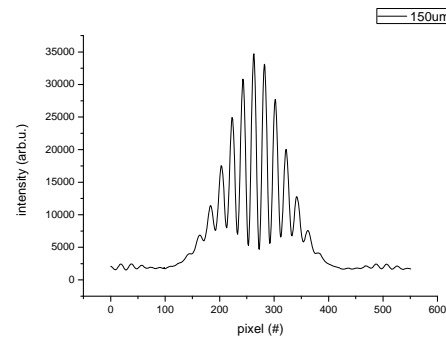
Graph 4.60. Interference fringes in double-slit Young's experiment. Single slit case (diffraction on a slit).



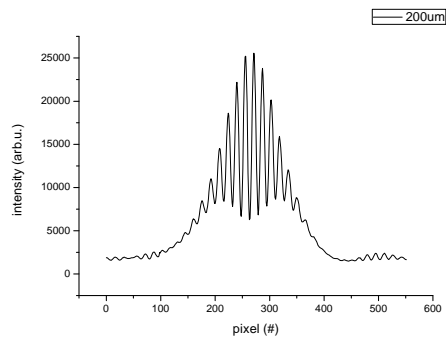
Graph 4.61. Interference fringes from two slits 50 μm apart.



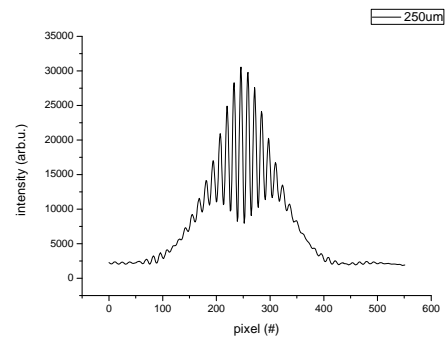
Graph 4.62. Interference fringes from two slits 100 μm away from one another.



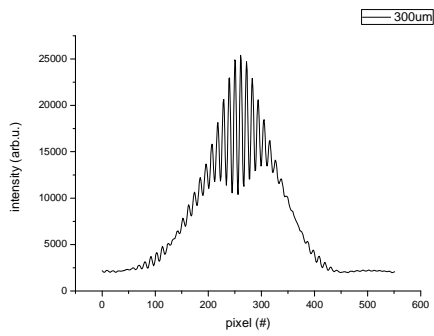
Graph 4.63. Interference fringes from slits 150 μm distant.



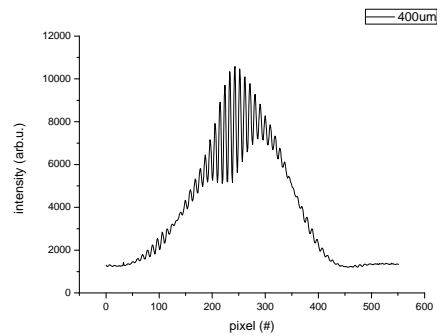
Graph 4.64. Interference fringes from slits spaced by 200 μm.



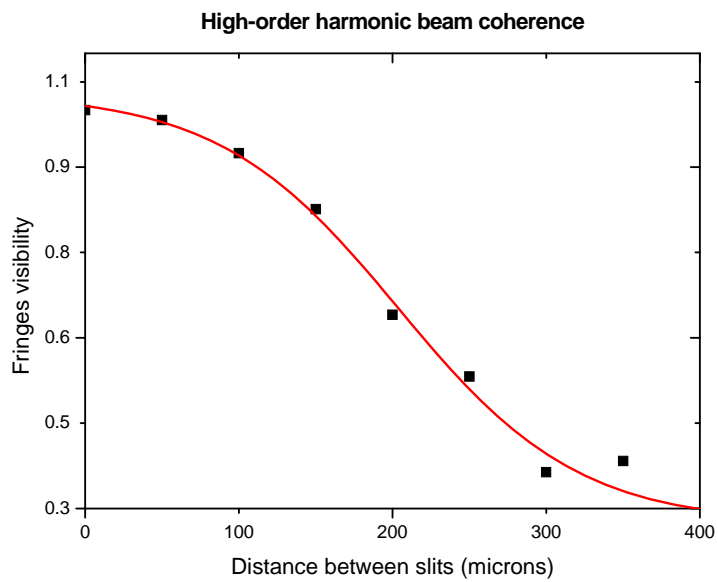
Graph 4.65. Interference pattern from 250 μm-distant slits.



Graph 4.66. Interference fringes using 300  $\mu\text{m}$  away from each other.



Graph 4.67. Interference pattern from 400  $\mu\text{m}$  distant slits.



Graph 4.68. Interference fringes visibility as a function of distance between the pair of slits.

## 4.5 Estimation of absolute HHG signal

The estimation of the absolute signal of the high-order harmonics were performed for experimental conditions of the laser:

- $E=1.2$  mJ,
- central wavelength  $\lambda_c=810$  nm,
- pulse time duration  $\Delta t=35$  fs,
- repetition rate of 91 Hz,
- acquisition time 3 s,
- iris size 11 mm,

and for the harmonic source:

- gas: Ar,
- pressure  $p=45$  mbar,
- cell length  $L=12$  mm,
- optimized longitudinal position (focus in vicinity of back face of the cell).

A 400 nm Al filter (Luxel) and lens of  $f=750$  mm were used. The measurements were performed using an absolutely calibrated X-ray CCD camera (Andor DX440-DN) with known quantum efficiency in spectral range 20-40 nm (Figure 4.20).

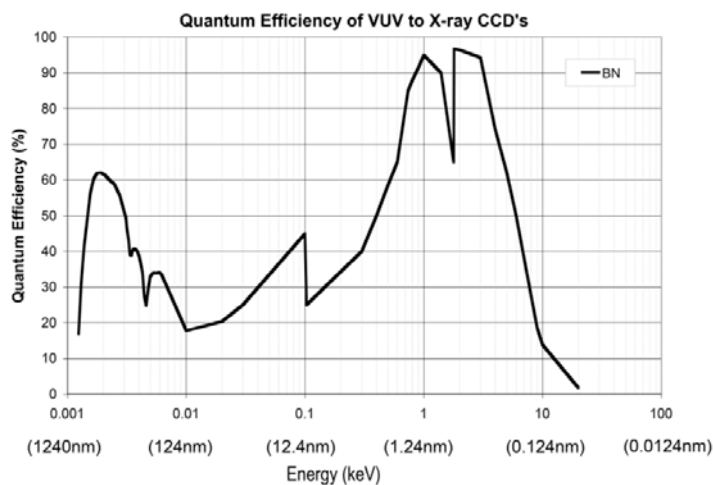


Figure 4.20. Andor DX440-DN quantum efficiency curve [52].

The experimental setup is presented in Figure 4.21. The total signal per single IR pulse in all harmonic orders was estimated to be 0.652 nJ and 0.085 nJ in a spectral line at 30 nm (the strongest harmonic order in the spectrum) resulting in conversion efficiency of  $5.4 \cdot 10^{-7}$  and  $7.1 \cdot 10^{-8}$ , respectively. Obtained CE is lower compared to record published results ( $\sim 10^{-5}$ ) in similar setups probably due to the lower intensity of the driving laser (c.f. scaling law discussion in Section 2.2.3) [56]. Since standard operation regime of the source involves repetition rate of 1 kHz of the driving laser, the integrated signal in all harmonics is 0.652  $\mu\text{J/s}$ .

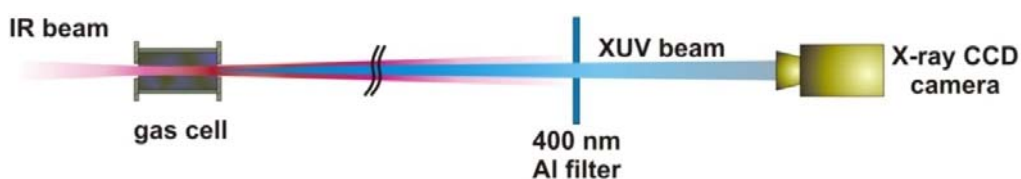


Figure 4.21. Experimental setup for estimation of absolute signal of high-order harmonic beam.

An important note shall be made that since Al filter was involved in the experiment oxidation of Al should be taken into account. It is known from the experiments that after oxidation of the filter involved in the experiment (even short-time exposure to atmospheric air) leads to drop of transmission of the filter in the spectral range by about 30 %! [65].

## Chapter 5. Applications of HHG source

High-order harmonics, due to their high repetition rate operation, tunability and high coherence degree, have already found a number of interesting applications. For instance, they involve material sciences, life sciences and detection technology. As an example high-order harmonics together with femtosecond NIR beam were used to efficiently modify tribological properties of materials. The results from these experiments are presented in the Section 5.1. High-order harmonics are also very practical in metrology of multilayer (ML) optics (Section 5.2). This type of source is also very useful for absolute calibration of EUV detectors (Section 5.3).

### 5.1 Materials surface processing

With the advent of table-top, high repetition rate, femtosecond laser systems great interest has been observed in the field of materials machining by ultrashort laser pulses. The applicability of femtosecond laser pulses to material sciences has been demonstrated in numerous experiments, which involved processing of semiconductors [66], [67], dielectrics [67]-[70], polymers [71] and metals [72]-[74]. However, most of the optically transparent materials, that attract lots of attention due to their perspective industrial applications, are strongly light-resistive. For example, polymers and dielectrics exhibit very low absorption coefficient in the near infrared spectral region. Hence the laser ablation threshold is very high for these materials [71], which results in low machining efficiency [68].

Recently, a new method for materials processing suitable for efficient machining of transparent materials has been demonstrated [75]. The technique utilizes simultaneous interaction of NIR femtosecond laser pulses generated by Ti: Al<sub>2</sub>O<sub>3</sub> laser system ( $\Delta t=32$  fs,  $E=2.8$  mJ,  $\lambda_c=820$  nm) and the second harmonic, combined with extreme ultraviolet (XUV) high-order harmonics with the strongest spectral line at 21.6 nm.

The experimental setup is shown in Figure 5.1 and Figure 5.2. For strong HHG a two-color laser field, consisting of fundamental and second harmonic (SH) of a femtosecond laser pulse, was applied to a gas jet of He [76]. Femtosecond laser pulses at 820 nm with an energy of 2.8 mJ and pulse duration of 32 fs were focused by a spherical mirror ( $f = 600$  mm) into a He gas jet. For SH generation, a 200- $\mu\text{m}$ -thick beta-barium borate (BBO) crystal was placed between the focusing mirror and gas jet so that, after the BBO crystal, the laser field consisted of both the SH and the residual fundamental laser fields. For the optimum SH conversion the BBO crystal was placed  $\sim 400$  mm from the focusing mirror and the energy conversion efficiency was about 27 %. A gas jet with a slit nozzle of 0.5 mm width and length of 6 mm was used [77]. The gas pressure in the interaction region was 150 Torr ( $\sim 0.2$  bar). Generated HHG were first characterized using a flat-field soft X-ray spectrometer equipped with a back-illuminated X-ray charge coupled device (Princeton Instruments). Optimization of the two-color HHG source was performed by selecting the gas jet position while controlling the relative phase between the two fields. The strongest harmonic at the 38<sup>th</sup> order (21.6 nm) reached energy of  $\sim 50$  nJ.

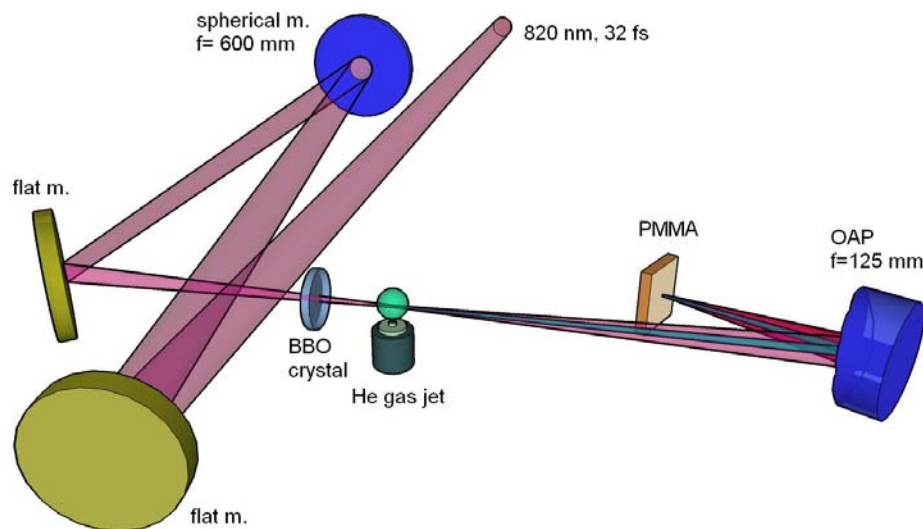


Figure 5.1. Schematic of the experimental setup for surface modification by dual action of XUV and Vis-NIR ultrashort pulses. Experiment was performed at Korean Advanced Institute of Science and Technology (KAIST).

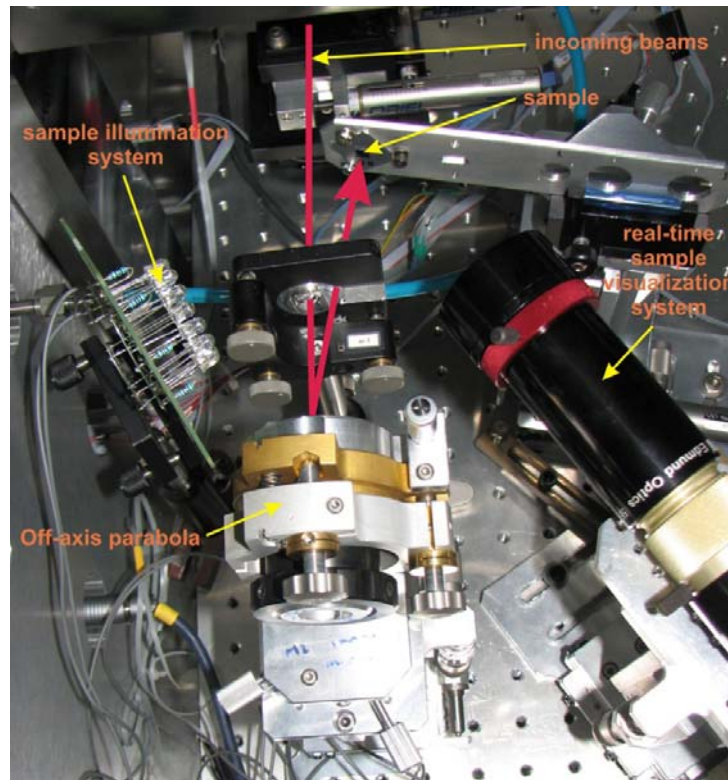


Figure 5.2. Picture of the experimental setup.

Subsequently, the spectrometer was replaced with a 1" diameter off-axis paraboloidal mirror (OAP,  $f = 125$  mm at  $13^\circ$ ) with a Mo:Si multilayer coating ( $R = 30\%$  at 21 nm) placed 245 mm from the HHG source. The sample target (500-nm thin layer of PMMA spin-coated on a 315  $\mu\text{m}$  thick silicon substrate; Silson, UK) was positioned 125 mm from the OAP, perpendicularly to the incident beam. The measured reflectivity of the OAP in the optical region was 37%. The measured diameter (full-width-at-half-maximum) of the HHG beam incident on the OAP was 280  $\mu\text{m}$  while the diameter of the fundamental and SH laser beams was  $\sim 4$  mm. The morphology of irradiated target surface was first investigated by Nomarski differential interference contrast optical microscope, and then with an atomic force microscope (AFM, Dimension 3100 scanning probe microscope driven by a NanoScope IV controller; Veeco, USA) operated in the tapping mode to preserve high resolution.

To estimate the spot size for both XUV and Vis-NIR beams at the target position, we have performed simulations of the employed optical layout using the ZEMAX optical software [63]. The modeling predicted an XUV spot size on PMMA of 140  $\mu\text{m}$ , which is

17 times smaller than that of Vis-NIR beams. The estimated fluence on the surface of the PMMA was  $97 \mu\text{J}/\text{cm}^2$  at 21.6 nm,  $14.7 \text{ mJ}/\text{cm}^2$  at 820 nm, and  $6.3 \text{ mJ}/\text{cm}^2$  at 410 nm per shot, respectively. As all these values lie far below the ablation threshold for PMMA by infrared ( $2.6 \text{ J}/\text{cm}^2$  for single-shot and  $0.6 \text{ J}/\text{cm}^2$  for 100 shots [78]) as well as by XUV ( $2 \text{ mJ}/\text{cm}^2$  [79]) radiation, no damage of target surface was expected.

The PMMA target was irradiated under the following conditions: a) Vis-NIR beams only (no gas jet in operation), b) XUV beam only ( $0.4 \mu\text{m}$  Al filter placed in front of the OAP), and c) mixed XUV/Vis-NIR field (21.6 nm + 820 nm + SH). In cases a) and b) we have not observed any signs of surface damage after irradiation by  $\sim 3000$  shots, although the accumulated dose was significantly higher than in case c). The target surface remained virtually unaffected, preserving its original quality and roughness. In striking contrast, the application of the mixed XUV/Vis-NIR field resulted in clearly visible, irreversible surface modification after irradiation with only a few shots. Figure 5.3 shows AFM images of the PMMA exposed to the simultaneous action of XUV and Vis-NIR ultrashort pulses. The damage is characteristic due to material expansion, quite different from ablation craters observed in experiments with pure XUV pulses [79]-[83]. A very interesting feature in Figure 5.3 is the formation of nano-scale spike(s) in the center of a uniform flat pedestal. The size of pedestal increases with the number of shots applied to the target ( $\sim 20 \mu\text{m}$  for 10 shots,  $\sim 60 \mu\text{m}$  for 50 shots) while the spikes have a radius of the order of few microns down to a few tens of nanometers in length ( $\sim 15 \text{ nm}$  for 30 shots,  $\sim 25 \text{ nm}$  for 40 shots). The target was also analyzed by Fourier-transform infrared spectroscopy, which revealed that the expanded material is exclusively PMMA, not the silicon from substrate.

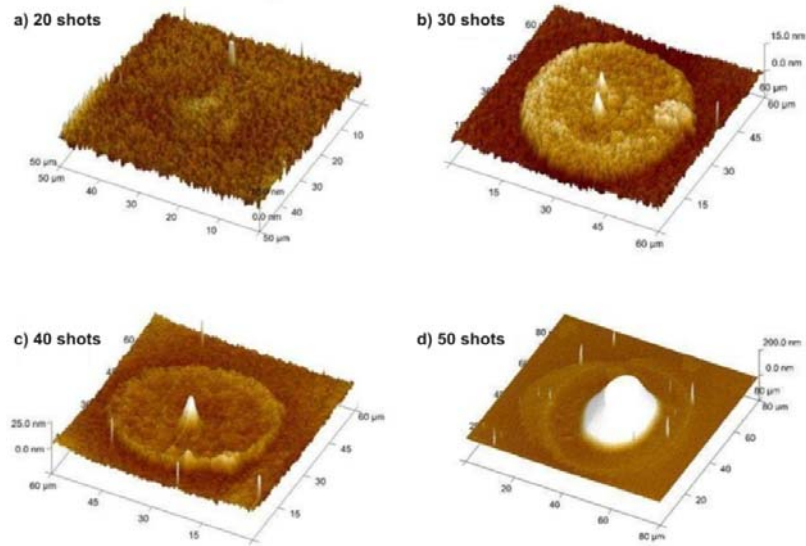


Figure 5.3. AFM images of the PMMA surface simultaneously irradiated with XUV and Vis-NIR ultrashort pulses. Experiment performed at KAIST.

To confirm obtained results and to perform processing of different materials surfaces another experiment was done. The same PMMA sample was used. Additionally, we also irradiated 890 nm layer of amorphous carbon (a-C) deposited by magnetron sputtering on a bulk silicon substrate (GKSS Research Centre, Germany). The experimental setup was as displayed in Figure 5.1. Due to larger laser intensity the single shot fluencies on the sample surface were  $15 \text{ mJ/cm}^2$  at 820 nm,  $6 \text{ mJ/cm}^2$  at 410 nm, and  $0.1 \text{ mJ/cm}^2$  at 21.6 nm.

There are very few data on laser ablation threshold of a-C. For multi-pulse irradiation of polycrystalline carbon by 100 fs laser pulses at 810 nm the ablation threshold is estimated to be of the order of a few  $\text{J/cm}^2$  [84]. For 25 fs, free-electron laser pulses at 32.5 nm, and a-C layer thickness of 46 nm, the single shot ablation threshold is  $\sim 60 \text{ mJ/cm}^2$  (estimation error  $\sim 50\%$ ) [85]. For 1.7 ns, Ne-like Ar capillary discharge laser at 46.9 nm, the ablation threshold has been estimated to be  $\sim 1.1 \text{ J/cm}^2$  in the single pulse regime [86].

The experimental results for PMMA are presented in Figure 5.4. The left part of the picture presents an image from Nomarski microscope of the sample irradiated with optical photons only, whereas the right part shows the sample exposed to optical and XUV beams applied simultaneously.

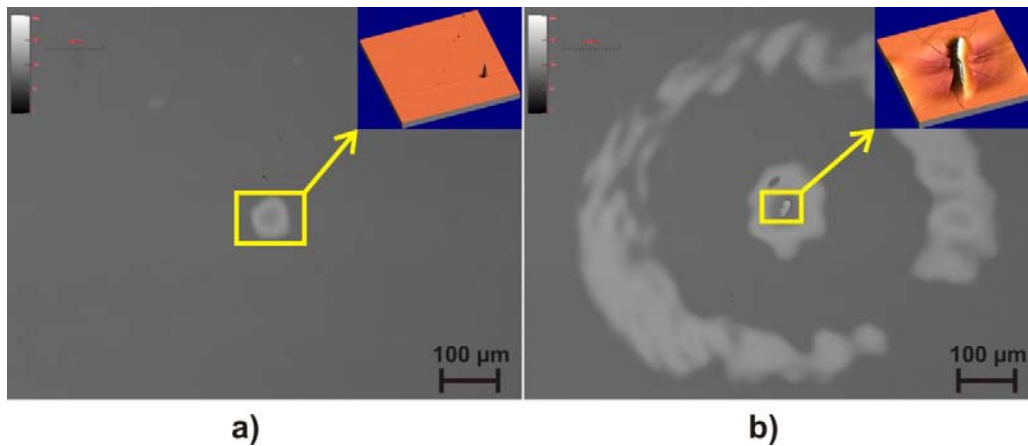


Figure 5.4. Images from Nomarski microscope of PMMA sample exposed to a single shot of (a) NIR-VIS radiation only, and (b) mixed field of XUV/NIR-VIS. Insets show the corresponding AFM images of details.

The sample irradiated solely with NIR-VIS light exhibits only negligible surface changes, whilst in the case of combined fields the area of the modified surface dramatically increases. The insets of AFM scans depict surface changes in the vicinity of the beam center. The damage occurred in a single pulse exposure. RMS microroughness of NIR-VIS and XUV/NIR-VIS illuminated samples was estimated to be 4.7 nm and 176.5 nm, respectively (evaluated only in the interaction region), and 5.7 nm for the unexposed sample [87]. The efficiency of the dual action is much higher than in the previous experiment due to larger fluencies. The difference in the surface changes visible in AFM scans suggests that the structures shapes are fluency-dependent.

Even stronger enhancement of surface processing by the dual action was observed on a-C sample (Figure 5.5). Laser Induced Periodic Surface Structures (LIPSS, or “ripples”) with spatial period of  $\sim 550$  nm were created during 10-shot exposure in the both cases; however, a clear difference in modulation depth was observed: the peak-to-valley depth was  $\sim 130$  nm for NIR-VIS irradiated sample, while  $\sim 200$  nm for combined XUV/NIR-VIS. Moreover, despite its random distribution, the frequency of occurrence of LIPSS is much higher in the case of the mixed fields. RMS microroughness was 13.5 nm for NIR-VIS illumination, 46.2 nm for XUV/NIR-VIS, and 8.3 nm for an unexposed sample, respectively.

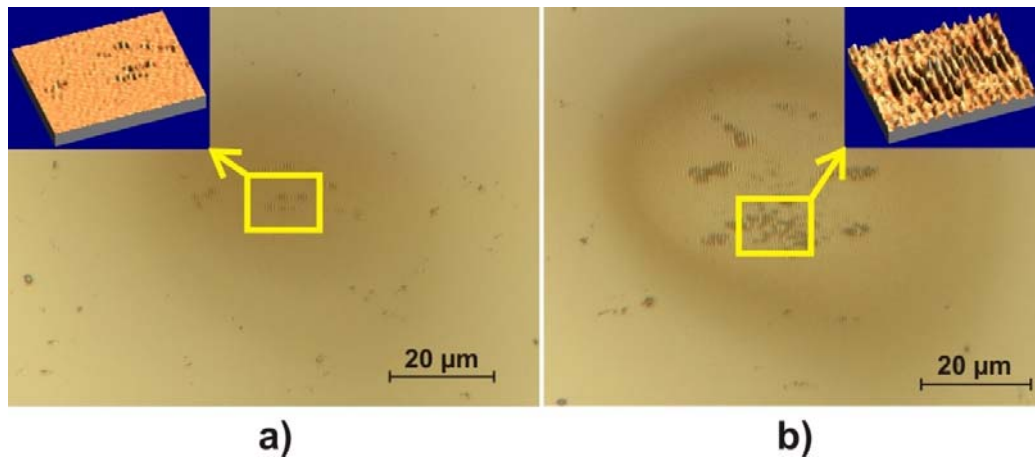


Figure 5.5. Nomarski microscope images of a-C sample exposed to 10 shots of (a) NIR-VIS beam only, and (b) XUV/NIR-VIS. Insets present corresponding AFM scans of details.

Physical mechanisms leading to increase of efficiency of materials processing in our experiments are explained in terms of radiation induced creation of defects in the exposed sample. These defects (e.g. color centers) are created in materials through *incubation effect*. Their appearance results in new electronic states inside the material bandgap leading to enhancement of absorption through these states by several orders of magnitude [70]. Consequently, this significantly lowers the ablation threshold. Moreover, when the sample is illuminated with highly energetic XUV photons the incubation effect takes place much faster compared to the case when only NIR photons excite the sample.

Another phenomenon enhancing the absorption of radiation in the sample is free-carrier absorption. Since very energetic photons have high probability of ionizing the host material (compared to low-energetic IR photons) free electron clouds are created in the material. These free electrons absorb NIR radiation leading to increased absorption coefficient for NIR spectral region. In the presented results this phenomenon is assessed to play a key role.

The physical mechanism of LIPSS formation similar to those observed in our experiments, has been broadly discussed in the literature (e.g. [66]-[74]). A few phenomena, present when LIPSS are created, have been successfully identified (i.e. incubation effect, free-carrier absorption preceded by ionization of surface of a material,

neutral atoms desorption, and positive ion emission due to Coulomb explosion); however, the complete process has not been elucidated yet.

The physical picture of LIPSS formation involves interference of scattered light in surface layer of the material what leads to creation of spatial intensity modulation. It has been proven by ultrafast electron diffraction measurements ([88], [67]) that before the rippled structures are created a very thin layer ( $\sim 30\text{-}40\text{ nm}$ ) on the surface of the sample is molten as a consequence of non-thermal phase transition on the surface of a sample irradiated with femtosecond laser pulses. In the layer convective currents induced by interference fringes arise which transport mass into the vacuum leading to expansion of the material (see Figure 5.6). Detailed discussion of processes involved in the dual action of XUV and optical radiation in processing of materials as well as the physical mechanisms involved in LIPSS creation can be found in [75] and [89].

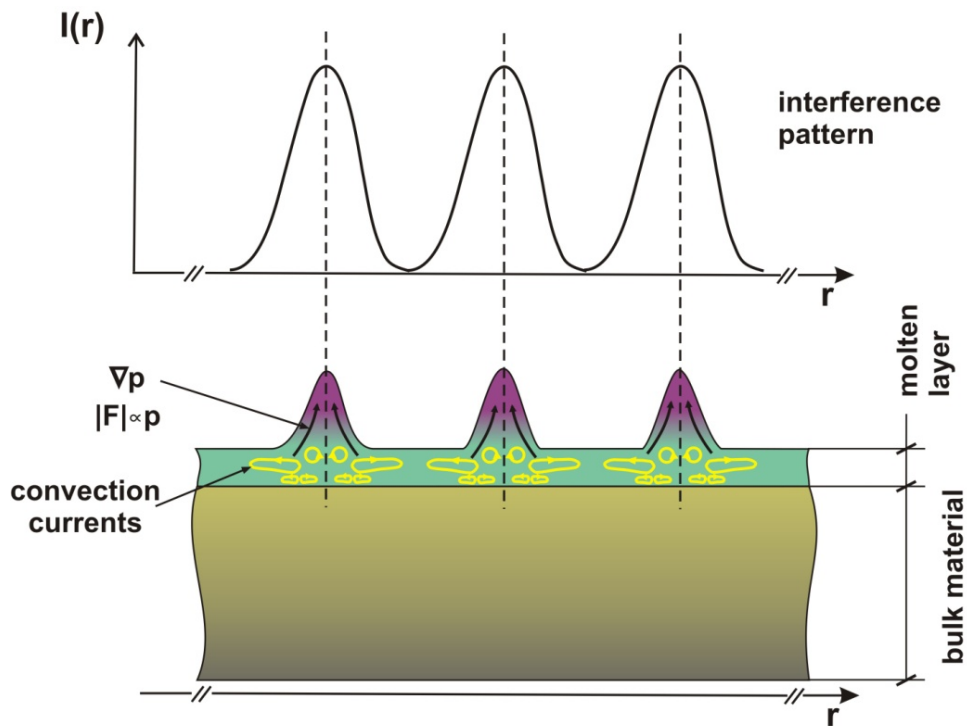


Figure 5.6. Convection currents model. A thin layer of bulk material is molten (thickness  $\sim$  tens of nm) after irradiation by femtosecond NIR laser. When the molten material is subject to interference pattern (upper part of the Figure), spatial modulation of pressure will be established leading to creation of local pressure gradients. In areas where pressure is higher, the “hotter” liquid will expand by means of convection currents (along the pressure gradient).

## 5.2 Multilayer optics metrology

The high-order harmonic source was also used for reflectivity measurements of multilayer mirror (ML) versus incidence angle. The experimental setup is presented in Figure 5.7 and Figure 5.8. The driving laser field featured the parameters:  $\lambda_c=820$  nm,

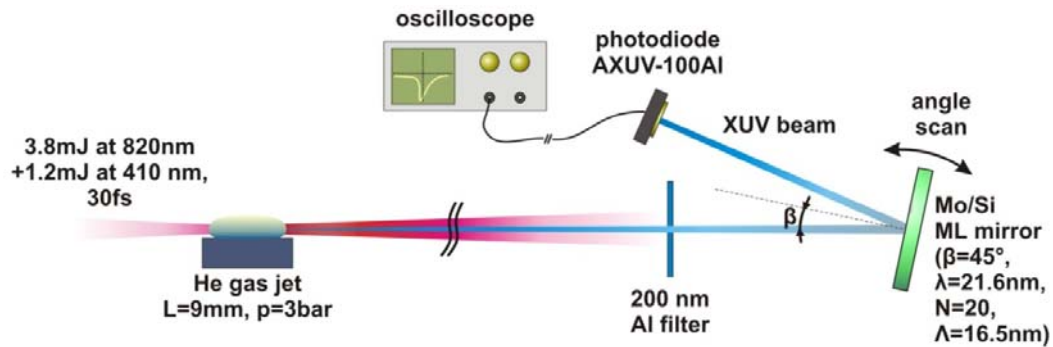


Figure 5.7. Experimental setup of measurement of reflectivity of multilayer mirror versus incidence angle. Experiment was performed at KAIST.

$\Delta t=30$  fs,  $E=4.5$  mJ. For efficient HHG generation the beam was frequency doubled with BBO crystal with conversion efficiency of  $\sim 27\%$ . Subsequently, the two beams were focused by a spherical mirror ( $f=125$  mm) into a gas cloud created by a helium gas jet at 3 bar backing pressure. The gas jet was 9 mm long. To filter out IR laser light 200 nm Al

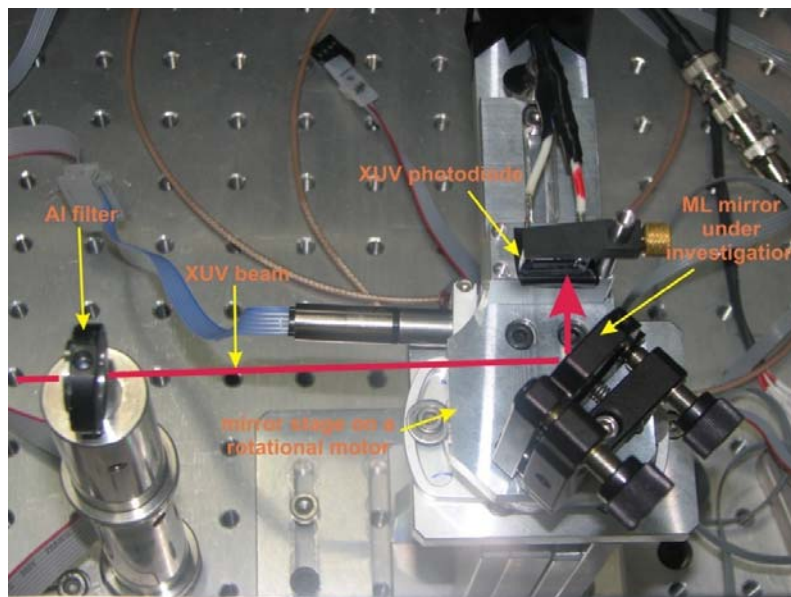
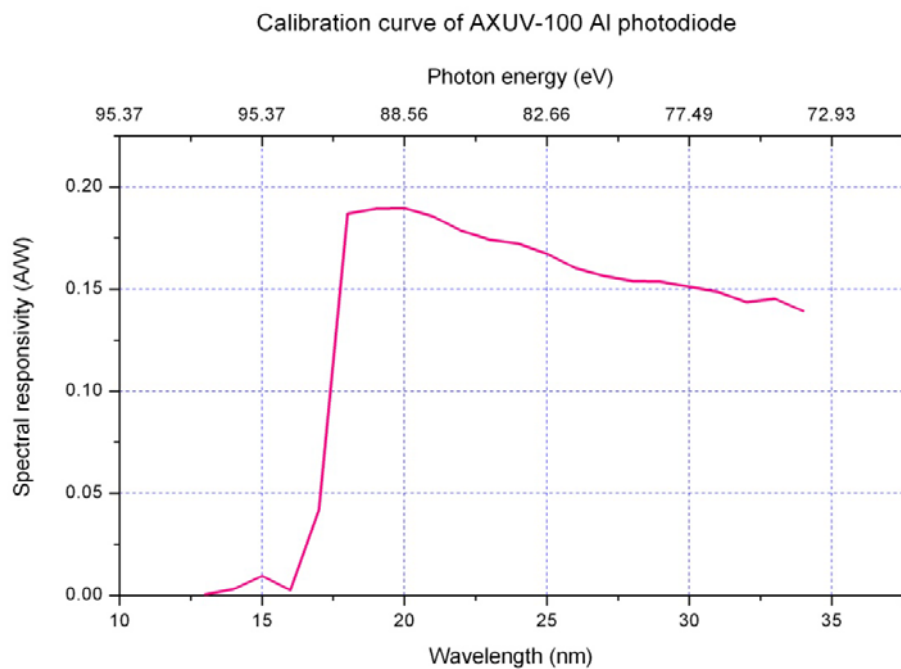


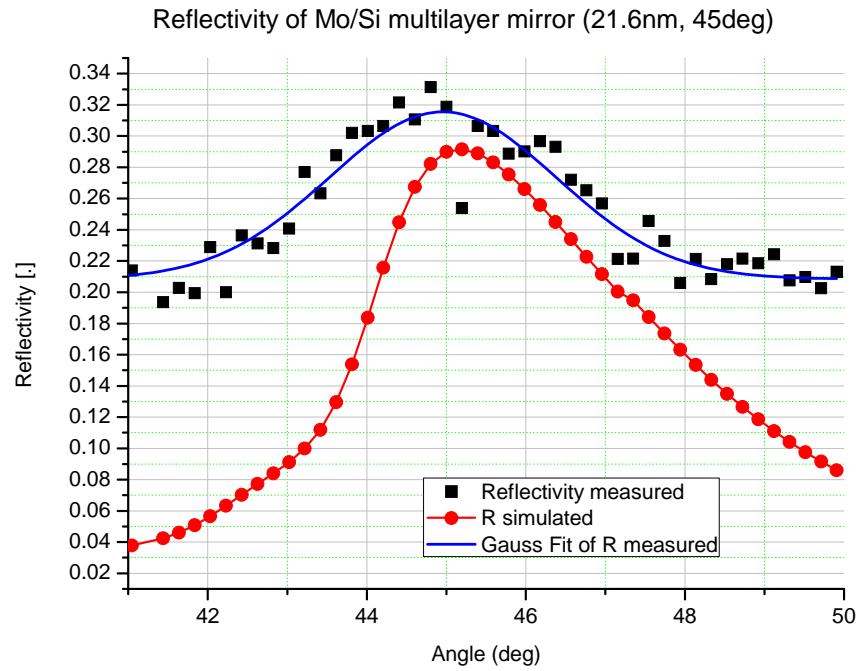
Figure 5.8. Photo of the experimental setup.

filter was used. The high-order harmonic source was optimized for the strongest harmonic line at 21.6 nm. The mirror comprised molybdenum-silicon multilayer structure (number of periods  $N=20$  with multilayer period of 16.5 nm) deposited on BK7 substrate (surface quality  $\lambda/20$ ). It was designed for operation at  $45^\circ$  and 21.6 nm wavelength (Institute of Scientific Instruments, AS CR, Brno, Czech Republic). The mirror was placed on the rotational stage together with the XUV sensitive absolutely calibrated (Graph 5.1) photodiode (type AXUV-100 Al, International Radiation Detectors) allowing change of the incidence angle  $\beta$  under vacuum. The photodiode is additionally covered with 150 nm Al filter. The signal was acquired with a Tektronix TDS 3052 oscilloscope.



Graph 5.1. Calibration curve of AXUV-100 Al photodiode (International Radiation Detectors Inc.).

Experimental results are presented in Graph 5.2. The measured and simulated reflectivities of the mirror are presented. The measured reflectivity was 31.5 % (fitted value) and simulated  $\sim 29\%$ . The insignificant difference could be due to the imperfections of manufacturing process as well as because of the possible additional errors (e.g. source instability or estimation error when taking into account additional input from neighboring harmonics).

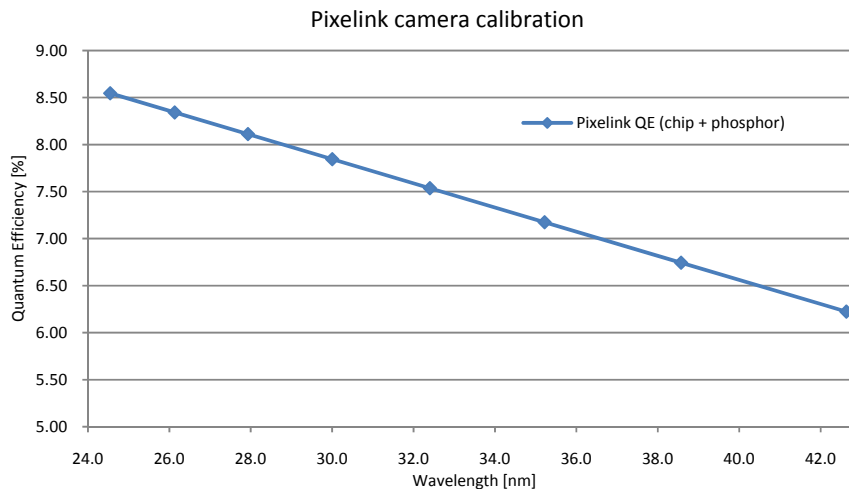


Graph 5.2. Reflectivity measurement of Mo/Si flat multilayer mirror designed for 21.6 nm radiation incident at 45° angle.

### 5.3 Absolute calibration of XUV-sensitive CMOS camera

High-order harmonic source was used to absolutely calibrate Pixelink CMOS camera in 25-42 nm spectral range. The technical details of the camera were described in Section 3.3.

First, the spectral measurements were performed to record the input of particular harmonics into total XUV signal. The measurement was performed with the TGS. The experimental setup is shown in Figure 3.4. Experimental conditions of HHG source were:  $p=50$  mbar, gas cell length 12 mm, IR beam iris size 10 mm, and lens focal length  $f=750$  mm. The driving laser parameters were:  $\lambda_c=810$  nm,  $\Delta t=35$  fs,  $E=1.2$  mJ. Then, the absolute total signal of XUV beam was estimated as described in the Section 4.5. The measurement with CMOS Pixelink camera was performed in the setup shown in Figure 4.21 (Andor camera was replaced by Pixelink camera). Knowing the quantum efficiency (QE) of Andor camera between 25-42 nm and using HHG spectrum it was possible to evaluate the values of XUV signal at different wavelengths. Knowing the percentage of each harmonic signal in total XUV beam energy it was possible to estimate the quantum efficiency of the CMOS chip and P43 phosphor layer versus wavelength.



Graph 5.3. Pixelink CMOS camera calibration curve. The estimated QE takes into account QE of CMOS chip as well as of phosphor layer (P43) deposited onto the chip for radiation conversion.

The calibration curve is shown in Graph 5.3.

The XUV signal level on the Pixelink camera was very low. For this reason it is possible that nonlinear part of the phosphor characteristics was used introducing significant source of calibration error. To tackle this problem higher EUV flux would be required. Another spring of the inaccuracy of the measurement comes from oxidation of the Al filter which is expected to be of the order of  $\sim 30\%$  [65] and is assessed as the upper limit of the calibration error.



## Chapter 6. Development of advanced XUV sources based on HHG

From their practical usefulness point of view high-order harmonic sources of XUV radiation display many interesting features but, on the other hand, they possess also one important disadvantage: they provide low single-pulse energy. Typically energy of the order of nJ (or less) per pulse is obtained for a single harmonic order what is not sufficient for many practical applications. Thus a great interest is observed in the field of the development of HHG to obtain greater single-shot energy of XUV beam. There are two promising approaches being investigated nowadays: *two-color HHG* and *amplification* of harmonic beam in the X-ray laser (XRL) plasma amplifiers. The two techniques have their pros and cons. As for the two-color scheme, more energetic beam of odd- and even-order harmonics is obtained (even by two orders of magnitude). This setup can be implemented with a table-top femtosecond laser systems (providing with a IR pulse energy ~few mJ/shot). On the other hand, amplification of harmonics even though requiring higher IR pulse energies than two-color scheme, it boosts the energy of XUV beam at single harmonic order (while suppressing others) and, additionally, performs spatial filtering of the XUV beam. Both techniques were experimentally investigated and the experimental results are presented below.

### 6.1 Two-color HHG

In the standard arrangement of HHG due to the inversion symmetry of a conversion gas in a single-frequency external electric field only odd-order harmonics can be generated (see discussion in Section 2.2.3). However, if an infrared femtosecond laser pulse is frequency-doubled by a nonlinear crystal and the two-color field interacts with the conversion gas the inversion symmetry is broken and odd- and even-order harmonics are generated [76]. Extensive examination of the HHG source revealed that in the *two-color HHG* XUV signal gain compared to standard setup of HHG is about 100 (Figure 6.1).

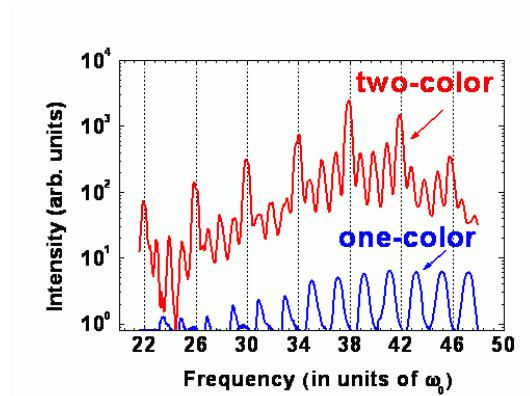


Figure 6.1. Comparison of the two-color HHG yield with 'standard' setup. Experimental conditions were: circular gas jet, He, 950 Torr ( $\sim 1.27$  bar), laser pulse energy: 2.8 mJ, pulse duration 28 fs, beam size 10 mm, BBO 10  $\mu\text{m}$  thick (conv. eff.  $\sim 20\%$ ), filtering: 1.5  $\mu\text{m}$  Al for 2-color case, 0.4  $\mu\text{m}$  Al for 1-color case [90].

The experiment on comprehensive source characterization and its optimization was performed [77]. The experimental setup is presented in Figure 6.2 and its photograph is shown in Figure 6.3. The femtosecond laser pulses (2.8 mJ, 30 fs,  $\lambda_c=820$  nm) were focused by a mirror ( $f=600$  mm) in the helium gas jet. BBO crystal was placed after the mirror for the second harmonic (SH) generation of the fundamental laser field. Two crystals were sequentially used: 100  $\mu\text{m}$  and 200  $\mu\text{m}$  thick resulting in conversion efficiency of 20 % and 28 %, respectively. The crystal was proceeded by half-wave plate to control phase between 820 nm and 410 nm fields. The nozzles used in the experiment were 1) circular with diameter of 0.5 mm, and 2) longitudinal with length of 3, 6 and 9 mm. Generated harmonics were detected using a flat-field extreme ultraviolet (XUV) spectrometer equipped with a back-illuminated X-ray charge coupled device

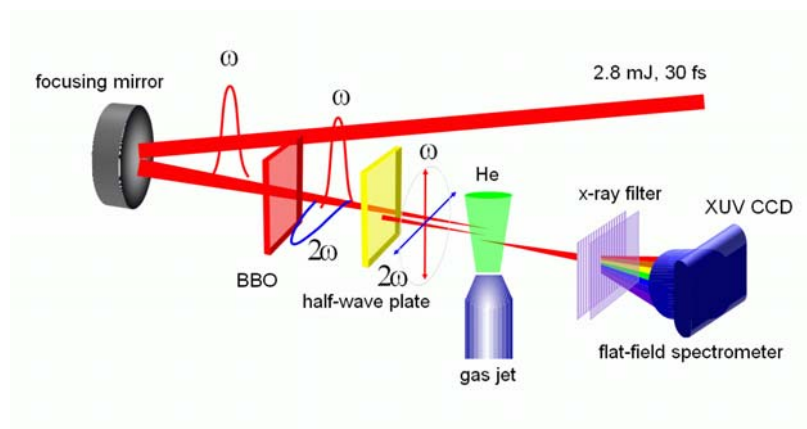


Figure 6.2. Two-color HHG setup. Experiment performed at KAIST.

(CCD; Princeton Instruments). Two aluminum filters of 1  $\mu\text{m}$  thickness were installed to block scattered laser light and to prevent the saturation of the CCD. The optimization of two-color HHG was performed by selecting the target length and the position while controlling the relative phase between the two fields and increasing the SH conversion.

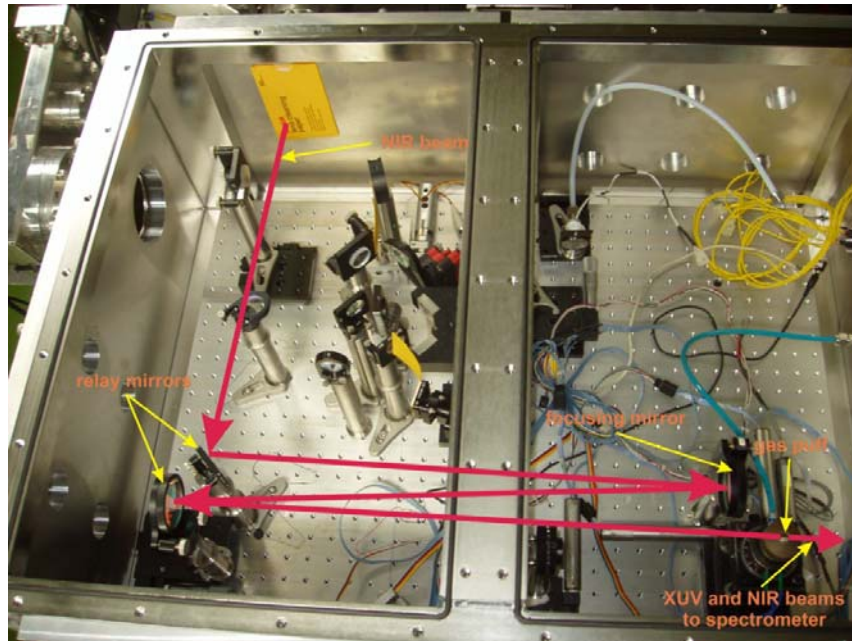


Figure 6.3. Picture of the experimental setup. BBO crystal (not visible in the picture) was placed after second relay mirror downstream and before the gas puff.

The phase between the first and second harmonic fields is a crucial parameter since it determines the electron trajectory after ionization and thus is a direct means to control harmonic signal. The phase between the fields in the experiment was controlled by a 150  $\mu\text{m}$  fused silica plate. Figure 6.4 shows the intensity modulation of the 38<sup>th</sup> harmonic order (21.6 nm) from the 6 mm He gas jet as a function of a relative phase between the two fields. The harmonic intensity modulation shows the periodicity of  $\pi$  in the relative phase change for 100  $\mu\text{m}$  as well as 200  $\mu\text{m}$  BBO crystals. The modulation depth is  $\sim 0.25$  for the 100  $\mu\text{m}$  BBO and  $\sim 0.16$  for the 200  $\mu\text{m}$  BBO crystal. With the control of relative phase, enhancement of 38<sup>th</sup> harmonic of 20 % for 200  $\mu\text{m}$  BBO and 30 % for 100  $\mu\text{m}$  thick BBO crystal was obtained.

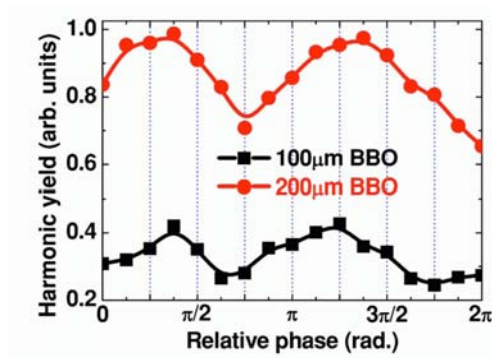


Figure 6.4. Examination of the phase influence between the two fields onto 38th harmonic yield. The two BBO crystals were used for SH generation.

By employing the long gas jet, much stronger HHG was achieved. The experimental results for different jet lengths and the jet position optimization are presented in Figure 6.5. The '0' longitudinal  $z$  position corresponds to the center of the gas jet at the laser beam waist and moving to negative  $z$  values corresponds to positioning of the focus after the jet nozzle. Optimized value of -10 mm from the focus suggests strong self guiding effect in the interaction region. In this case the intensity of fundamental and SH fields were  $9 \cdot 10^{14} \text{ W/cm}^2$  and  $4 \cdot 10^{14} \text{ W/cm}^2$ , respectively. The increase of the signal of the 38<sup>th</sup> harmonic was observed up to 6 mm jet length and was followed by intensity drop for 9 mm jet. Consequently, this means that optimized 6 mm gas jet length is absorption limited configuration. The absorption length  $l_a$  for helium at 100 Torr (0.133 bar) is about 2 mm what confirms theory prediction of  $3 \cdot l_a$  interaction length for absorption limited HHG [91].

High-order harmonic spectrum visible in Figure 6.5b shows that the dominant

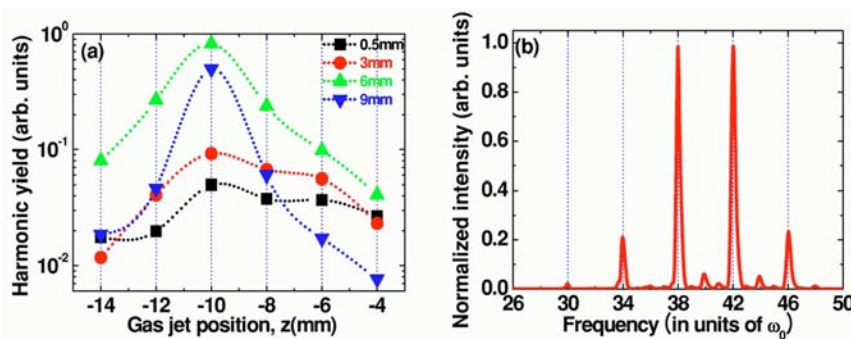


Figure 6.5. Optimization of gas jet length a) and HHG spectrum for optimized 6 mm jet length b).

harmonic orders are  $2(2n+1)$  compared to  $2n$  and  $(2n+1)$ .

The optimized HHG source in this setup provided with  $0.6 \mu\text{J}$  at  $21.6 \text{ nm}$  as well as at  $19.5 \text{ nm}$  per single shot giving world record conversion efficiency of  $2 \cdot 10^{-4}$ .

The setup for HHG in two-color scheme was also implemented at IoP/PALS using a gas cell. The experimental setup is displayed in Figure 6.6. The IR laser pulses ( $\lambda_c=810 \text{ nm}$ ,  $\Delta t=35 \text{ fs}$ ,  $E=1.2 \text{ mJ}$ ,  $1 \text{ kHz}$ ) were focused by a lens ( $f=750 \text{ mm}$ ). The fundamental laser field was then frequency doubled using  $200 \mu\text{m}$  thick BBO crystal with conversion efficiency of  $30 \%$  resulting in the estimated intensity of  $6.11 \cdot 10^{13} \text{ W/cm}^2$  and  $1.43 \cdot 10^{14} \text{ W/cm}^2$  for blue and IR beams, respectively. The two beams were interacting with the conversion gas (Ar at  $40 \text{ mbar}$ ). In case of HHG using only fundamental frequency laser field the gas cell was  $10 \text{ mm}$  and the IR beam size was  $11 \text{ mm}$ , while in case of two-color scheme the gas cell length was  $4 \text{ mm}$  and the beam size was  $12 \text{ mm}$ . The harmonic beam was filtered using  $0.8 \mu\text{m}$ -thick Al filter (Lebow Company). Integration time in the both cases was  $0.5 \text{ s}$ .

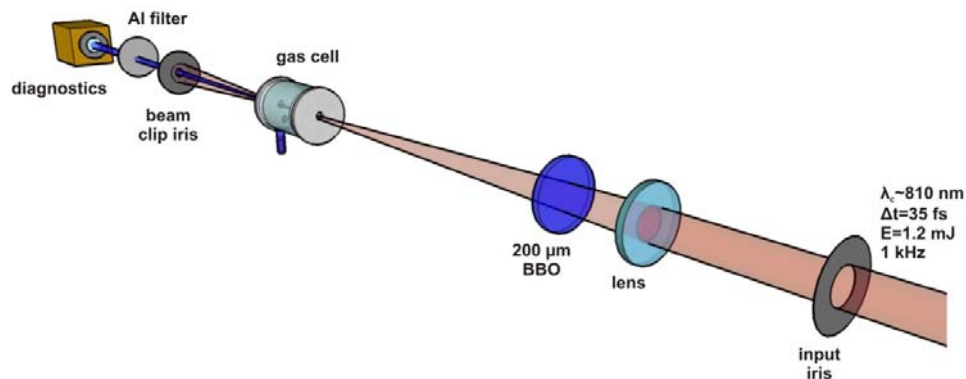


Figure 6.6. HHG in two-color scheme at IoP/PALS.

The experimental results are presented in Figure 6.7. The upper part of the picture presents spectrum from HHG using only fundamental laser light. The odd-order harmonics can be observed ( $30 \text{ nm}$  is  $27^{\text{th}}$  harmonic order). However, in case of two-color HHG (Figure 6.7b) new spectral lines coming from even-order harmonics were observed (e.g.  $45 \text{ nm}$  is  $18^{\text{th}}$  harmonic order of the fundamental laser light).

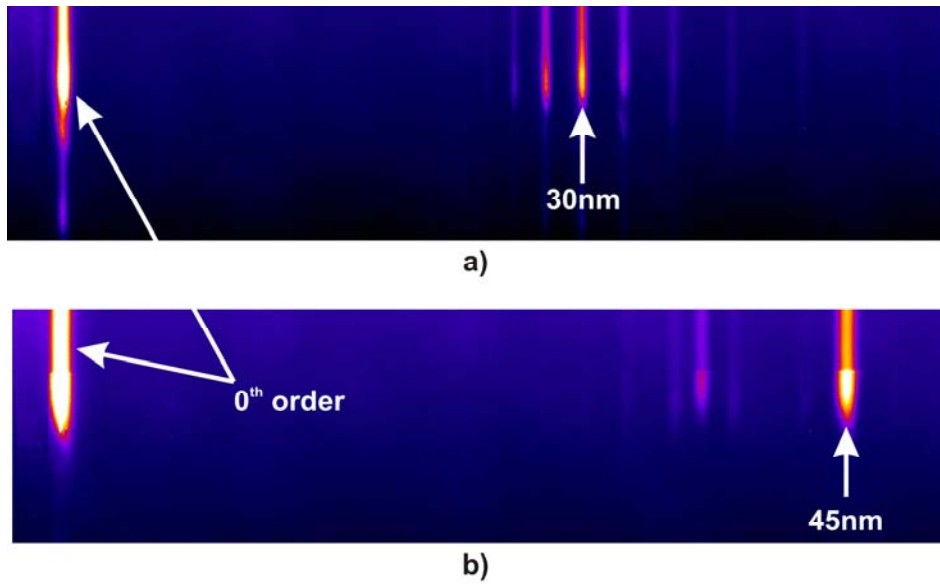
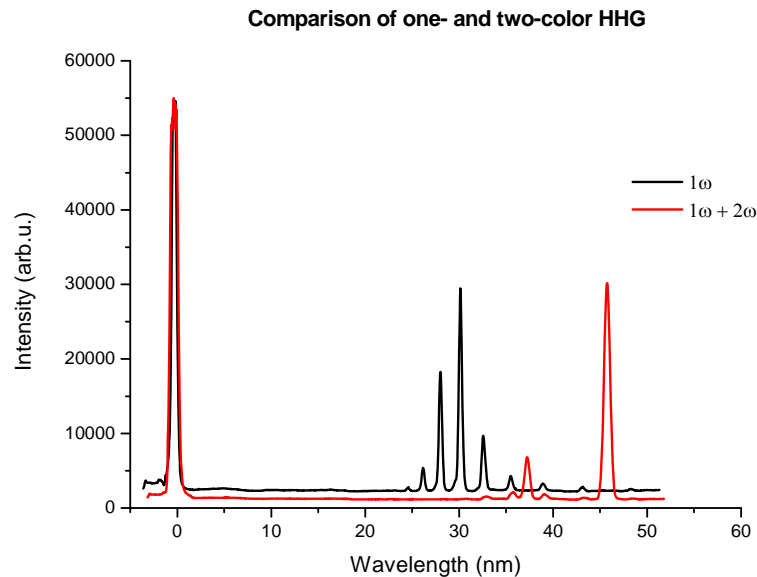


Figure 6.7. Spectra of HHG using only fundamental femtosecond laser field a) and in two-color scheme b).

Wavelength-calibrated spectra of HHG in single- and two-color setups are presented in Graph 6.1 (lineout of spectra from Figure 6.7) clearly showing appearance of new wavelengths being even-order harmonics of 810 nm of type  $2(2n+1)$ .



Graph 6.1. Comparison of single-color and two-color HHG. The occurrence of even harmonic orders is clearly visible.

---

Presented preliminary experimental results obtained at IoP/PALS show for the first time a proof of operation of HHG in two-color scheme in a gas cell. However, in order to obtain higher flux values and shorter wavelengths in even-order harmonics higher intensity of the driving laser field is required.

## 6.2 Amplification of high-order harmonics in OFI laser amplifier

The first demonstration of the high-order harmonics amplification in XRL plasma amplifier was reported by Ditmire *et al.* in 1995 [92]. In the experiment frequency-doubled pulses from Nd:glass CPA laser system ( $\Delta t=1.3$  ps,  $\lambda=527$  nm,  $E=5$  J) were focused by with an  $f=3.5$  m lens ( $f/50$ ) in the helium supersonic gas jet (1 mm long). The intensity in the focus of the lens was  $5 \cdot 10^{15}$  W/cm<sup>2</sup>. The atomic gas density in the interaction region was  $1 \cdot 10^{19}$  cm<sup>-3</sup>. The XRL collisionally pumped plasma amplifier was created using three 1054 nm beams, each providing  $E=200$  J. Gallium was chosen as an amplifying medium due to very good match between 21<sup>st</sup> harmonic order at 25.11 nm and one of the J=2-1 transition lines of Ga. Ga target was 600 nm thick, 200  $\mu$ m wide and 18 mm long stripe deposited on a glass substrate. The seeded 21<sup>st</sup> harmonic energy was between 0.5 and 2 nJ. The gain observed in the experiment was about 3.

Later, high-order harmonics were successfully amplified in optical field ionized (OFI) laser plasma amplifier by Zeitoun *et al.* [93]. Since this setup involves using gas targets as plasma amplifier material self-emission of the amplifier is significantly reduced (compared to collisionally pumped solid-state based XRL). In the arrangement seed is created using linearly polarized titanium sapphire laser pulses ( $E=20$  mJ,  $\Delta t=30$  fs,  $\lambda_c=815$  nm, repetition rate 10 Hz) focused with a spherical lens ( $f=1.5$  m) in a gas cell (10 mm long) filled with argon ( $p=25$  mbar). The focus was located 40 mm after the cell. The intensity in the focal spot was  $\sim 10^{15}$  W/cm<sup>2</sup>. The HHG source was optimized for 25<sup>th</sup> harmonic order at 32.8 nm to match Kr<sup>8+</sup> soft XRL transition line between the levels  $3d^9 4d(1^1S_0) - 3d^9 4p(1^1P_1)$ . The plasma amplifier was created using circularly polarized titanium-sapphire laser pulses focused by a spherical mirror ( $f=0.85$  m) in a gas cell filled with Kr. Intensity of  $5 \cdot 10^{17}$  W/cm<sup>2</sup> was obtained in the focal spot. The estimated small-signal gain coefficient was 80 cm<sup>-1</sup>. The HHG source was imaged with a grazing incidence (grazing incidence angle 4°) gold-coated toroidal mirror ( $R \sim 80\%$ ) at the input of the plasma amplifier. The delay between seed arrival at plasma amplifier and XRL pumping beam was optimized with respect to temporal gain profile. When the seed intensity at

32.8 nm was 1/50 XRL amplifier saturation level the selected HHG spectral line intensity was amplified 200 times (Figure 6.8). Since the gain life-time is about 8 ps and seed pulse duration is about 20 fs the amplified pulse duration is Fourier-limited. In the experiment  $\Delta\lambda \sim 2$  pm implying amplified pulse duration of 500 fs.

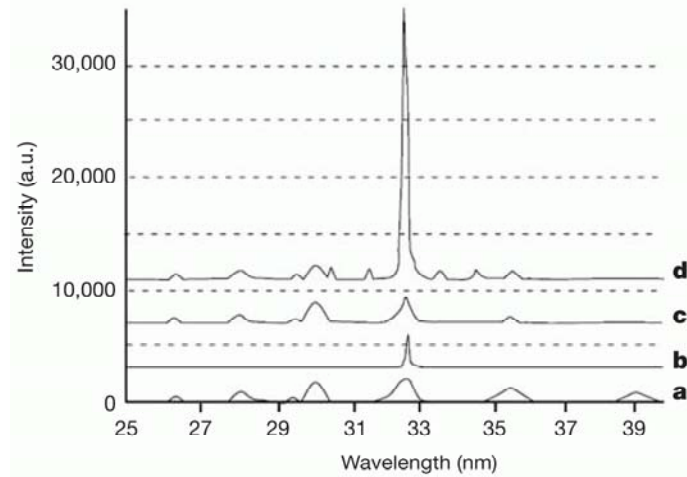


Figure 6.8. HHG amplification in OFI laser plasma amplifier. a) is harmonic seed, b) is ASE of SXRL only, c) is seeded SXRL with detuned timing between amplifier formation pulse and seed arrival, d) time-optimized seeded SXRL [93].

Additionally, it has been demonstrated theoretically and experimentally that when a seed beam spectrum is much wider than width of the amplification bandwidth.

The experimental results presented in Ref. [93] suggested that during amplification additionally beam quality is being improved (reduction of XUV beam divergence was observed). This became a stimulus for a joint experiment (Figure 6.9) performed at Laboratoire d'Optique Appliquée (LOA), France. Two independent IR beams were used. Both were running at 10 Hz. Their pulse time duration was 34 fs and central wavelength 815 nm. One, circularly polarized beam of energy  $\sim 575$  mJ was used to produce active medium of the OFI laser. It was focused with on-axis, spherical mirror of 1 m focal length in the gas cell of length of 7.5 mm filled with Kr. The other, linearly polarized beam (not presented in the figure) of energy of 10 mJ was focused with spherical lens of 1.5 m focal length in another gas cell (7 mm long) filled with Ar at 30 mbar pressure. The second cell served as a HHG seed. Grazing incidence toroidal mirror was used to image HHG source output onto the OFI laser amplifier gas cell with

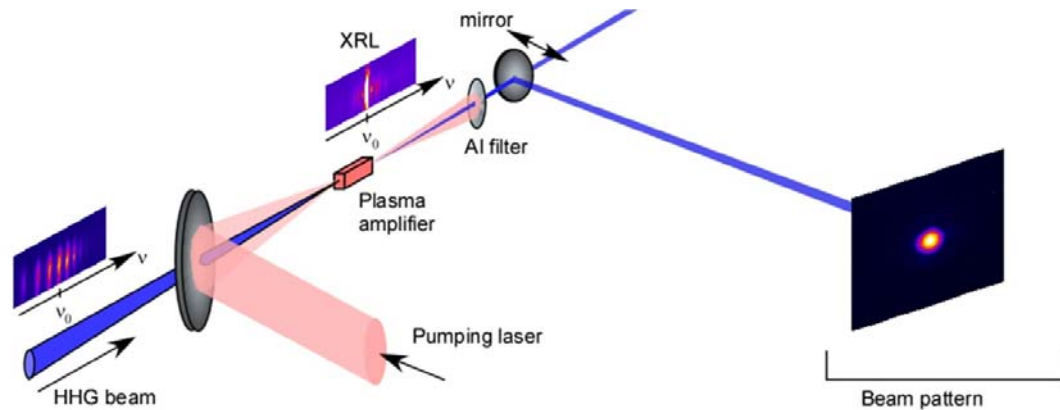


Figure 6.9. HHG-seeded SXRL experimental setup providing improved XUV beam quality [94]. Experiment performed at Laboratoire d'Optique Appliquée.

magnification of 1.5. Spatial (transversal) coherence was measured by placing a pair of Young's slits into the x-ray beam  $\sim 700$  mm away from the plasma amplifier. Each slit was  $23 \mu\text{m}$  wide, and slit pairs with spacing of 115, 226, and  $323 \mu\text{m}$  were used for the measurements. The interference pattern and far field were measured by using a 16-bit CCD camera.

The experimental results are displayed in Figure 6.10. The coherence radius, defined as slits separation for which fringes visibility is higher than 0.61, of unseeded beam was  $102 \mu\text{m}$  corresponding to 25 % of the HHG beam diameter, and  $232 \mu\text{m}$  which is 60 % of the amplified beam diameter. This clearly proves transversal coherence improvement of the seeded beam (by a factor of  $\sim 2.3$ ). It is attributed to XUV beam spatial filtering by gain region of OFI laser plasma amplifier. The measurements using Hartmann wavefront sensor revealed wavefront distortion of  $\lambda/17$  (1.9 nm). According to Marechal criterion (RMS deviation from reference sphere at the diffraction focus should not be smaller than  $\lambda/14$  [96]) this is aberration-free XUV laser beam. The beam divergence of amplified 25<sup>th</sup> harmonic order at 32.8 nm was estimated to be 1.34 mrad [97].

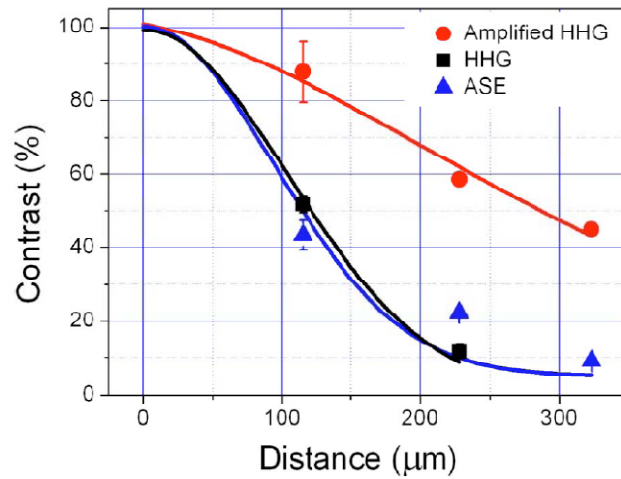


Figure 6.10. Improvement of HHG beam seeded into SXRL OFI laser plasma amplifier [95].

Comparing the two presented techniques it should be recognized that a great advantage of two-color scheme is its relatively low setup complexity. Additionally, amplification of harmonics due to available bandwidth of the OFI laser amplifier leads to prolongation of the time duration of the XUV pulse to  $\sim\text{ps}$  (compared to seed pulse). On the other hand the multi-stage amplification scheme offers a way to obtain bright, table-top (compared to free electron lasers - FEL) source of coherent XUV and X-ray radiation with a perfect beam shape and stability highly exceeding properties of FEL beams with a great additional advantage of easily-solvable problem of synchronous operation by the use of any arbitrary master clock in the system.



## Chapter 7. Conclusion

High-order harmonics from their first observation have been extensively investigated resulting in a good understanding of physical processes involved in their generation. The main physical processes can be now well understood on the basis of the three step model proposed by P. B. Corkum [10]. Due to the great advent in the ultrafast laser technology, impressive progress has been recently observed in the efficiency of HHG, cut-off extension to shorter-wavelength region (even to hard X-rays) and generation of attosecond pulses. This also allowed improvement in energy of XUV pulses obtained from HHG by means of two-color HHG as well as amplification of HHG in XRL plasma amplifiers. Having at hand sub- $\mu\text{J}$  pulses of coherent pico- and femtosecond XUV pulses it became feasible to find practical applications of the source. Some of them cover investigation of ultrafast processes in atoms, others; however, are of very practical use in, e.g., structuring of surface of the materials or multilayer optics metrology. Future perspectives for HHG sources are very promising. Mostly amplifications of harmonics attract lots of attention of the scientific community. Additionally, there is lots of activity observed in the generation of harmonics from vacuum-solid interface. Both techniques require; however, further improvements in femtosecond laser technology - especially in terms of pulse intensity and pulse contrast. For instance, efficient HHG from plasma at the interface of the vacuum and solid target intensities higher than  $10^{17} \text{ W/cm}^2$  are required with the pulse contrast greater than  $10^6$ . Moreover, generation of single attosecond pulses requires carrier-envelope stabilization of the driving laser field. Finally, in order to extend cut-off in HHG from gases there are built femtosecond laser systems in the mid-infrared spectral region what found its motivation from the fact that cut-off spectral position is proportional to  $E \propto I \cdot \lambda^2$  (Eq. 2.3).

The HHG source is assessed to be a very promising for needs of the future ultra compact sources of coherent radiation in XUV, soft X-ray and even X-ray spectral regions. It should be stressed that at the moment there is no other source of short-wavelength coherent radiation and of ultrashort pulse duration at the same time - the

source that would also be available at laboratory scale providing an unprecedented tool for investigation of the ultrashort physical processes. It should be stated; however, that high-order harmonics cannot substitute every kind of XUV radiation source. As an example, this type of the source is not of practical use in plasma backlighting.

The results presented in Chapter 3 and Chapter 4 show that source of high-order harmonics based on a gas cell arrangement was successfully implemented, optimized and extensively characterized at IoP/PALS. The HHG beamline is now ready for use by scientific community. First promising results on structuring of surface of the materials with the use of HHG and NIR laser pulses were presented in Chapter 5. The source was also successfully used for characterization of multilayer X-ray optics and cost-efficient absolute calibration of XUV-sensitive CMOS camera. Moreover, the results presented in the Chapter 6 clearly show that the intense beams of the coherent XUV radiation can now be obtained in the laboratory scale either in two-color scheme or by seeding high-order harmonics into laser plasma amplifier which additionally leads to beam quality improvement and its monochromaticity.

During the doctoral study the following tasks have been successfully completed:

- harmonic source was successfully built at IoP/PALS,
- the source was fully optimized and extensively characterized,
- versatile novel application experiments were performed,
- additionally, two experiments on further development of ultrafast coherent soft x-ray sources (two-color HHG and HHG amplification) were performed.

The work presented in this dissertation clearly shows the great scientific potential of the harmonic source. Most promising future perspective of the developed beamline covers harmonic amplification in XRL plasma amplifier (at IoP/PALS). Moreover, generation of harmonics in a hollow fiber is concerned as a very interesting field of study to be undertaken. Finally, a number of application experiments which also include two-color materials surface structuring aimed at detailed understanding of the physical processes involved in the *two-color action* is under preparation. A possible field

for further work is building attosecond beamline which would require construction of the time-of-flight spectrometer.

The Author of this dissertation has participated in physical installation of the laser system and in the development as well as installation of the vacuum systems in the laboratory. He is the author of the conceptual design of the gas cell and was the person responsible for tests of the device. The work on the implementation, characterization and optimization of the harmonic source was performed in self-reliant manner with help of supervisor-specialist. The Author also performed testing, improvements and coded calibration software for transmission grating spectrometer used in the experiment as a part of development of the instrumentation. He is the main person responsible for proposal, preparation and performance of the application experiment related to metrology of multilayer optics, absolute calibration of XUV-sensitive CMOS camera, and  $M^2$  factor measurements. He was a member of the experimental team in the experiments related to two-color harmonic generation (at KAIST), amplification of harmonics, and application of harmonics in the surface structuring of the materials using dual action of harmonics and IR pulses.

Brand new or valuable results related to characterization of the harmonic source, its applications and further developments are:

- materials surface structuring using harmonics and IR laser pulses in, so called, dual action (discovery of a new physical phenomenon),
- multilayer optics metrology,
- absolute calibration of the XUV-sensitive camera,
- world record single-pulse harmonic energy in the two-color scheme and conversion efficiency record,
- observation of XUV beam spatial filtering during amplification of harmonics,
- coherence measurements of the beam,
- observation of Maker fringes during optimization experiment,
- $M^2$  measurements of the harmonic beam in the focusing scheme.



## Chapter 8. References

- [1] W. C. Roentgen "On a new kind of rays", *Nature* **53**, 274-276 (1896).
- [2] [http://en.wikipedia.org/wiki/Wilhelm\\_Conrad\\_R%C3%B6ntgen](http://en.wikipedia.org/wiki/Wilhelm_Conrad_R%C3%B6ntgen)
- [3] B. Schenkel, J. Biegert, U. Keller, C. Vozzi, M. Nisoli, G. Sansone, S. Stagira, S. De Silvestri, and O. Svelto "Generation of 3.8-fs pulses from adaptive compression of a cascaded hollow fiber supercontinuum", *Opt. Lett.* **28**, 1987-1989 (2003).
- [4] K. Yamane, Z. Zhang, K. Oka, R. Morita, M. Yamashita, and A. Suguro "Optical pulse compression to 3.4 fs in the monocycle region by feedback phase compensation", *Opt. Lett.* **28**, 2258-2260 (2003).
- [5] T. Brabec and F. Krausz "Intense few-cycle laser fields: Frontiers of nonlinear optics", *Rev. Mod. Phys.* **72**, 545-591 (2000).
- [6] P. M. Paul, E. S. Toma, P. Breger, G. Mullot, F. Augé, Ph. Balcou, H. G. Muller, P. Agostini "Observation of a Train of Attosecond Pulses from High Harmonic Generation", *Science* **292**, 5522, 1689-1692 (2001).
- [7] R. Kienberger, E. Goulielmakis, M. Uiberacker, A. Baltuska, V. Yakovlev, F. Bammer, A. Scrinzi, Th. Westerwalbesloh, U. Kleineberg, U. Heinzmann, M. Drescher & F. Krausz "Atomic transient recorder", *Nature* **427**, 817-821 (2004).
- [8] M. Schultze, E. Goulielmakis, M. Uiberacker, M. Hofstetter, J. Kim, D. Kim "Powerful 170-attosecond XUV pulses generated with few-cycle laser pulses", *New Journal of Physics* **9**, 243 (2007).
- [9] P. B. Corkum, N. H. Burnett, and F. Brunel "Above-threshold ionization in the long-wavelength limit", *Phys. Rev. Lett.* **62**, 1259 - 1262 (1989).
- [10] P. B. Corkum "Plasma perspective on strong field multiphoton ionization", *Phys. Rev. Lett.* **71**, 1994-1997 (1993).
- [11] J. J. Macklin J. D. Kmetec, C. L. Gordon "High-order harmonic generation using intense femtosecond pulses", *Phys. Rev. Lett.* **70**, 766-769 (1993).

- [12] N. A. Papadogiannis, B. Witzel, C. Kalpouzos, and D. Charalambidis "Observation of Attosecond Light Localization in Higher Order Harmonic Generation", *Phys. Rev. Lett.* **83**, 4289 - 4292 (1999).
- [13] P. Christov, M. M. Murnane, and H. C. Kapteyn "High-Harmonic Generation of Attosecond Pulses in the "Single-Cycle" Regime", *Phys. Rev. Lett.* **78**, 1251 - 1254 (1997).
- [14] A. Baltuska, Th. Udem, M. Uiberacker, M. Hentschel, E. Goulielmakis, Ch. Gohle, R. Holzwarth, V. S. Yakovlev, A. Scrinzi, T. W. Hänsch & F. Krausz "Attosecond control of electronic processes by intense light fields", *Nature* **421**, 611-615 (2003).
- [15] J. Sola, E. Mével, L. Elouga, E. Constant, V. Strelkov, L. Poletto, P. Villoresi, E. Benedetti, J.-P. Caumes, S. Stagira, C. Vozzi, G. Sansone and M. Nisoli "Controlling attosecond electron dynamics by phase-stabilized polarization gating", *Nature Physics* **2**, 319 - 322 (2006).
- [16] V. Vénierard, R. Taïeb, and A. Maquet "Phase dependence of (N+1)-color (N > 1) ir-uv photoionization of atoms with higher harmonics", *Phys. Rev. A* **54**, 721-728 (1996).
- [17] M. Drescher, M. Hentschel, R. Kienberger, M. Uiberacker, V. Yakovlev, A. Scrinzi, Th. Westerwalbesloh, U. Kleineberg, U. Heinzmann & F. Krausz "Time-resolved atomic inner-shell spectroscopy", *Nature* **419**, 803-807 (24 October 2002).
- [18] R. Kienberger, M. Hentschel, M. Uiberacker, Ch. Spielmann, M. Kitzler, A. Scrinzi, M. Wieland, Th. Westerwalbesloh, U. Kleineberg, U. Heinzmann, M. Drescher, F. Krausz "Steering Attosecond Electron Wave Packets with Light", *Science* **297**, 1144-1148 (2002).
- [19] Y. Mairesse and F. Quéré "Frequency-resolved optical gating for complete reconstruction of attosecond bursts", *Phys Rev. A* **71**, 011401 (2005).
- [20] J. Itatani, F. Quéré, G. L. Yudin, M. Yu. Ivanov, F. Krausz, and P. B. Corkum "Attosecond Streak Camera", *Phys. Rev. Lett.* **88**, No. 17, 173903-1 (2002).
- [21] G. Sansone, E. Benetti, C. Vozzi, S. Stagira and M. Nisoli "Attosecond metrology in the few-optical-cycle regime", *New Journal of Physics* **10**, 025006 (2008).

- [22] R. Kienberger, M. Uiberacker, M. F. Kling, F. Krausz "Attosecond physics comes of age: from tracing to steering electrons at sub-atomic scales", *J. Modern Optics* **54**, 13-15, 1985-1998 (2007).
- [23] U. Becker and D. A. Shirley "VUV and Soft X-Ray Photoionization", 152, Plenum, New York (1996).
- [24] M. Hentschel, R. Kienberger, Ch. Spielmann, G. A. Reider, N. Milosevic, T. Brabec, P. Corkum, U. Heinzmann, M. Drescher, F. Krausz "Attosecond metrology", *Nature* **414**, 509-513 (2001).
- [25] T. Remetter, P. Johnsson, J. Mauritsson, K. Varjú, Y. Ni, F. Lépine, E. Gustafsson, M. Kling, J. Khan, R. López-Martens, K. J. Schafer, M. J. J. Vrakking and A. L'Huillier "Attosecond electron wave packet interferometry", *Nature Physics* **2**, 323 - 326 (2006).
- [26] H. Niikura, F. Légaré, R. Hasbani, A. D. Bandrauk, M. Yu. Ivanov, D. M. Villeneuve and P. B. Corkum "Sub-laser-cycle electron pulses for probing molecular dynamics", *Nature* **417**, 917-922 (2002).
- [27] J. Itatani, J. Levesque, D. Zeidler, H. Niikura, H. Pépin, J. C. Kieffer, P. B. Corkum and D. M. Villeneuve "Tomographic imaging of molecular orbitals", *Nature* **432**, 867-871 (2004).
- [28] F. Quéré, C. Thaur, P. Monot, S. Doboş, and Ph. Martin "Coherent Wake Emission of High-Order Harmonics from Overdense Plasmas", *Phys. Rev. Lett.* **96**, 125004 (2006).
- [29] E. Lorin, S. Chelkowski and A. D. Bandrauk "Attosecond pulse generation from aligned molecules - dynamics and propagation in  $H^{2+}$ ", *New Journal of Physics* **10**, 025033 (2008).
- [30] R. W. Boyd "Nonlinear Optics", Second Edition, Academic Press (2003).
- [31] L. V. Keldysh, *Sov. Phys. - JETP* **20**, 1307 (1965).
- [32] M. V. Ammosov, N. B. Delone, V. P. Krainov, *Sov. Phys. - JETP* **64**, 1191 (1986).
- [33] T. Pfeifer, C. Spielmann and G. Gerber "Femtosecond x-ray science", *Rep. Prog. Phys.* **69** 443-505 (2006).
- [34] P. Jaeglé "Coherent Sources of XUV Radiation. Soft X-Ray Lasers and High-Order Harmonic Generation", Springer 2006.

- [35] A. L'Huillier and Ph. Balcou "High-order harmonic generation in rare gases with a 1-ps 1053-nm laser", *Phys. Rev. Lett.* **70**, 774 - 777 (1993).
- [36] A. Rundquist, Ch. G. Durfee, Z. Chang, C. Herne, S. Backus, M. M. Murnane, H. C Kapteyn "Phase-Matched Generation of Coherent Soft X-rays", *Science* **280**, 1412 - 1415 (1998).
- [37] H. Sakai, K. Miyazaki "High-order harmonic generation in nitrogen molecules with subpicosecond visible dye-laser pulses", *Appl. Phys. B* **61**, 493-498 (1995).
- [38] R. Velotta, N. Hay, M. B. Mason, M. Castillejo, and J. P. Marangos "High-Order Harmonic Generation in Aligned Molecules", *Phys. Rev. Lett.* **87**, 183901 (2001).
- [39] T. Kanai, S. Minemoto, and H. Sakai "Ellipticity Dependence of High-Order Harmonic Generation from Aligned Molecules", *Phys. Rev. Lett.* **98**, 053002 (2007).
- [40] N. Hay, R. Velotta, M. Lein, R. de Nalda, E. Heesel, M. Castillejo, and J. P. Marangos "High-order harmonic generation in laser-aligned molecules", *Phys. Rev. A* **65**, 053805 (2002).
- [41] R. L. Carman, D. W. Forslund, and J. M. Kindel "Visible Harmonic Emission as a Way of Measuring Profile Steepening", *Phys. Rev. Lett.* **46**, 29 - 32 (1981).
- [42] B. Bezzerides, R. D. Jones, and D. W. Forslund "Plasma Mechanism for Ultraviolet Harmonic Radiation Due to Intense CO<sub>2</sub> Light", *Phys. Rev. Lett.* **49**, 202 - 205 (1982).
- [43] B. Dromey, M. Zepf, A. Gopal, K. Lancaster, M. S. Wei, K. Krushelnick, M. Tatarakis, N. Vakakis, S. Moustazis, R. Kodama, M. Tampo, C. Stoeckl, R. Clarke, H. Habara, D. Neely, S. Karsch and P. Norreys "High harmonic generation in the relativistic limit", *Nature Physics* **2**, 456 - 459 (2006).
- [44] P. Balcou, R. Haroutunian, S. Sebban, G. Grillon, A. Rousse, G. Mullot, J.-P. Chambaret, G. Rey, A. Antonetti, D. Hulin, L. Roos, D. Descamps, M. B. Gaarde, A. L'Huillier, E. Constant, E. Mevel, D. von der Linde, A. Orisch, A. Tarasevitch, U. Teubner, D. Klöpfel and W. Theobald "High-order-harmonic generation: towards laser-induced phase-matching control and relativistic effects", *Appl. Phys. B* **74**, 509-515 (2002).

- [45] A. Tarasevitch, K. Lobov, C. Wünsche, and D. von der Linde "Transition to the Relativistic Regime in High Order Harmonic Generation", *Phys. Rev. Lett.* **98**, 103902 (2007).
- [46] F. Quéré, C. Thaury, J-P. Geindre, and Ph. Martin "Comment on "Transition to the Relativistic Regime in High Order Harmonic Generation"", *Phys. Rev. Lett.* **100**, 089401 (2008).
- [47] C. Thaury, F. Quéré, J.-P. Geindre, A. Levy, T. Ceccotti, P. Monot, M. Bougeard, F. Réau, P. d'Oliveira, P. Audebert, R. Marjoribanks & Ph. Martin "Plasma mirrors for ultrahigh-intensity optics", *Nature Physics* **3**, 424 - 429 (2007).
- [48] B. Rus, T. Mocek, A. R. Präg, M. Kozlová, G. Jamelot, A. Carillon, D. Ros, D. Joyeux, and D. Phalippou "Multimillijoule, highly coherent x-ray laser at 21 nm operating in deep saturation through double-pass amplification", *Phys. Rev. A* **66**, art. no. 063806 (2002).
- [49] Primary design and prototype realization by P. Homer.
- [50] Primary design and prototype realization by B. Rus.
- [51] Company nm<sup>2</sup> LLC.
- [52] Andor Technology <http://www.andor.com/>
- [53] X. F. Li, A. L'Huillier, M. Ferray, L. A. Lompré, and G. Mainfray "Multiple-harmonic generation in rare gases at high laser intensity", *Phys. Rev. A* **39**, 5751 - 5761 (1989).
- [54] P. D. Maker, R. W. Terhune, M. Nisenoff, C. M. Savage "Effects of dispersion and focusing on the production of optical harmonics", *Phys. Rev. Lett.* **8**, 21-23 (1962).
- [55] A. L'Huillier, P. Balcou, L. A. Lompre "Coherence and Resonance Effects in High-Order Harmonic Generation", *Phys. Rev. Lett.* **68**, 166-170 (1992).
- [56] S. Kazamias, D. Douillet, F. Weihe, C. Valentin, A. Rousse, S. Sebban, G. Grillon, F. Auge, D. Hulin, and Ph. Balcou "Global Optimization of High Harmonic Generation", *Phys. Rev. Lett.* **90**, 193901-1 (2003).
- [57] S. Kazamias, D. Douillet, C. Valentin, F. Weihe, F. Auge, Th. Lefrou, G. Grillon, S. Sebban, and Ph. Balcou "Observation of high-contrast coherence fringes in high-order harmonic generation", *Phys. Rev. A* **68**, 033819 (2003).

- [58] J. J. Rocca "Table-top soft x-ray lasers", *Rev. Sci. Instr.* **70**, 3799 (1999).
- [59] ISO Standard 11146 "Lasers and laser-related equipment – Test methods for laser beam widths, divergence angles and beam propagation ratios" (2005).
- [60] B. E. A. Saleh, M. C. Teich "Fundamentals of Photonics". Second Edition, Wiley & Sons, 2007.
- [61] Center for X-ray Optics, <http://www-cxro.lbl.gov/>
- [62] OriginLab <http://www.originlab.com/>
- [63] ZEMAX Development Corporation, <http://www.zemax.com/>.
- [64] OPTIMASK S.A. <http://www.optimask.fr/>
- [65] M. Kozlova – personal contact. Measurement performed using Ne-like Zn XRL.
- [66] F. Costache, S. Kouteva-Arguirova, J. Reif "Sub-damage-threshold femtosecond laser ablation from crystalline Si: surface nanostructures and phase transformation", *Appl. Phys. A* **79**, 1429-1432 (2004).
- [67] O. Varlamova, F. Costache, J. Reif, M. Bestehorn "Self-organized pattern formation upon femtosecond laser ablation by circularly polarized light", *Appl. Surf. Sci.* **252**, 4702-4706 (2006).
- [68] J. Krüger, W. Kautek "Femtosecond-pulse visible laser processing of transparent materials", *Appl. Surf. Sci.* **96-98**, 430-438 (1996).
- [69] R. Stoian, H. Varel, A. Rosenfeld, D. Ashkenasi, R. Kelly, E. E. B. Campbell "Ion time-of-flight analysis of ultrashort pulsed laser-induced processing of  $A_2O_3$ ", *Appl. Surf. Sci.* **165**, 44-55 (2000).
- [70] M. Henyk, F. Costache, J. Reif "Ultra short laser pulse ablation from sodium chloride – the role of laser induced color centers", *Appl. Surf. Sci.* **197-198**, 90-95 (2002).
- [71] J. Krüger, W. Kautek "Ultrashort Pulse Laser Interaction with Dielectrics and Polymers", *Adv. Polym. Sci.* **168**, 247-289 (2004).
- [72] S. Sakabe, M. Hashida, S. Tokita, S. Namba, and K. Okamuro "Mechanism for self-formation of periodic grating structures on a metal surface by a femtosecond laser pulse", *Phys. Rev. B* **79**, 033409 (2009).

- [73] M. Tsukamoto, K. Asuka, H. Nakano, M. Hashida, M. Katto, N. Abe, M. Fujita "Periodic microstructures produced by femtosecond laser irradiation on titanium plate", *Vacuum* **80**, 1346-1350 (2006).
- [74] N. Yasumaru, K. Miyazaki, J. Kiuchi "Fluence dependence of femtosecond-laser-induced nanostructure formed on TiN and CrN", *Appl. Phys. A* **81**, 933-937 (2005).
- [75] T. Mocek, J. Polan, P. Homer, K. Jakubczak, B. Rus, I.J. Kim, C. M. Kim, G. H. Lee, Ch. H. Nam, V. Hajkova, J. Chalupsky, and L. Juha "Surface modification of organic polymer by dual action of extreme ultraviolet/visible-near infrared ultrashort laser pulses", *J. Appl. Phys.* **105**, 026105 (2009).
- [76] I.J. Kim, C. M. Kim, H. T. Kim, G. H. Lee, Y. S. Lee, J. Y. Park, D. J. Cho, and Ch. H. Nam "Highly Efficient High-Harmonic Generation in an Orthogonally Polarized Two-Color Laser Field," *Phys. Rev. Lett.* **94**, 243901 (2005).
- [77] I.J. Kim, G. H. Lee, S. B. Park, Y. S. Lee, T. K. Kim, Ch. H. Nam, T. Mocek, and K. Jakubczak "Generation of submicrojoule high harmonics using a long gas jet in a two-color laser field," *Appl. Phys. Lett.* **92**, 021125 (2008).
- [78] S. Baudach, J. Bonse, J. Krüger, W. Kautek "Ultrashort pulse laser ablation of polycarbonate and polymethylmethacrylate", *Appl. Surf. Sci.* 154-155, 555-560 (2000).
- [79] J. Chalupsky, L. Juha, J. Kuba, J. Cihelka, V. Hakova, S. Koptyaev, J. Krasa, A. Velyhan, M. Bergh, C. Coleman, J. Hajdu, R. M. Bionta, H. Chapman, S. P. Hau-Riege, R. A. London, M. Jurek, J. Krzywinski, R. Nietubyc, J. B. Pelka, R. Sobierajski, J. Meyer-ter-Vehn, A. Krenz-Tronnier, K. Sokolowski-Tinten, N. Stojanovic, K. Tiedtke, S. Toileikis, T. Tschentscher, H. Wabnitz, and U. Zastra "Characteristics of focused soft X-ray free-electron laser beam determined by ablation of organic molecular solids," *Opt. Express* **15**, 6036 (2007).
- [80] L. Juha, M. Bittner, D. Chvostova, J. Krasa, M. Kozlova, M. Pfeifer, J. Polan, A. R. Präg, B. Rus, M. Stupka, J. Feldhaus, V. Letal, Z. Otcenasek, J. Krzywinski, R. Nietubyc, J. B. Pelka, A. Andrejczuk, R. Sobierajski, L. Ryc, F. P. Boody, H. Fiedorowicz, A. Bartnik, J. Mikolajczyk, R. Rakowski, P. Kubat, L. Pina,

- M. Horvath, M. E. Grisham, G. O. Vaschenko, C. S. Menoni, and J. J. Rocca "Short-wavelength ablation of molecular solids: pulse duration and wavelength effects," *J. Microlith. Microfab. Microsyst.* **4**, 033007 (2005).
- [81] G. Vaschenko, A. G. Etxarri, C. S. Menoni, J. J. Rocca, O. Hemberg, S. Bloom, W. Chao, E. H. Anderson, D. T. Attwood, Y. Lu, and B. Parkinson "Nanometer-scale ablation with a table-top soft x-ray laser," *Opt. Lett.* **31**, 3615 (2006).
- [82] J. Krzywinski, R. Sobierajski, M. Jurek, R. Nietubyc, J. B. Pelka, L. Juha, M. Bittner, V. Letal, V. Vorlicek, A. Andrejczuk, J. Feldhaus, B. Keitel, E. Saldin, E. Schneidmiller, R. Treusch, and M. Yurkov "Conductors, semiconductors, and insulators irradiated with short-wavelength free-electron laser," *J. Appl. Phys.* **101**, 043107 (2007).
- [83] T. Mocek, B. Rus, M. Kozlová, M. Stupka, A. R. Präg, J. Polan, M. Bittner, R. Sobierajski, and L. Juha "Focusing a multimillijoule soft x-ray laser at 21 nm," *Appl. Phys. Lett.* **89**, 051501 (2006).
- [84] V. V. Kononenko, T. V. Kononenko, S. M. Pimenov, M. N. Sinyavskii, V. I. Konov, F. Dausinger "Effect of the pulse duration on graphitisation of diamond during laser ablation", *Quantum Electronics* **35** (3) 252-256 (2005).
- [85] S. P. Hau-Riege, R. A. London, R. M. Bionta, M. A. McKernan, S. L. Baker, J. Krzywinski, R. Sobierajski, R. Nietubyc, J. B. Pelka, M. Jurek, L. Juha, J. Chalupský, J. Cihelka, V. Hájková, A. Velyhan, J. Krása, J. Kuba, K. Tiedtke, S. Toleikis, Th. Tschentscher, H. Wabnic, M. Bergh, C. Coleman, K. Sokolowski-Tinten, N. Stojanovic, U. Zastra "Damage threshold of inorganic solids under free-electron-laser irradiation at 32.5 nm wavelength", *Appl. Phys. Lett.* **90**, 173128 (2007).
- [86] L. Juha, V. Hajkova, J. Chalupsky, V. Vorlicek, A. Ritucci, A. Reale, P. Zuppella, and M. Stoermer "Radiation damage to amorphous carbon thin films irradiated by multiple 46.9 laser shots below the single-shot ablation threshold", *J. Appl. Phys.* **105**, 093117 (2009).
- [87] I. Horcas, R. Fernandez, J. M. Gomez-Rodriguez, J. Colchero, J. Gomez-Herrero and A. M. Baro, *Rev. Sci. Instrum.* **78**, 013705 (2007).

- [88] B. J. Siwick, J. R. Dwyer, R. E. Jordan, R. J. D. Miller "An Atomic Level View of Melting Using Femtosecond Electron Diffraction", *Science* **302**, 1382-1385 (2003).
- [89] K. Jakubczak, T. Mocek, J. Chalupsky, G. H. Lee, T. K. Kim, S. B. Park, Ch. H. Nam, V. Hajkova, L. Juha, and B. Rus "Enhanced surface structuring by XUV/NIR ultrafast dual action " – in preparation.
- [90] I J. Kim - personal contact.
- [91] E. Constant, D. Garzella, P. Breger, E. Mével, Ch. Dorrer, C. Le Blanc, F. Salin, and P. Agostini "Optimizing High Harmonic Generation in Absorbing Gases: Model and Experiment", *Phys. Rev. Lett.* **82**, 1668 - 1671 (1999).
- [92] T. Ditmire, M. H. R. Hutchinson, M. H. Key, C. L. S. Lewis, A. MacPhee, I. Mercer, D. Neely, M. D. Perry, R. A. Smith, J. S. Wark and M. Zepf "Amplification of xuv harmonic radiation in a gallium amplifier", *Phys. Rev. A* **51**, R4337 - R4340 (1995).
- [93] Ph. Zeitoun, G. Faivre, S. Sebban, T. Mocek, A. Hallou, M. Fajardo, D. Aubert, Ph. Balcou, F. Burgy, D. Douillet, S. Kazamias, G. de Lachèze-Murel, T. Lefrou, S. le Pape, P. Mercère, H. Merdji, A. S. Morlens, J. P. Rousseau & C. Valentin "A high-intensity highly coherent soft X-ray femtosecond laser seeded by a high harmonic beam", *Nature* **431**, 426-429 (2004).
- [94] J. Ph. Goddet - personal contact.
- [95] J. Ph. Goddet, S. Sebban, A. S. Morlens, J. Gautier, J. Ph. Rousseau, F. Burgy, Ph. Zeitoun, C. Valentin, C. Hauri, G. Maynard, A. Boudaa, J. P. Caumes, H. Merdji, T. Mocek, M. Kozlova, and K. Jakubczak "Demonstration of a spatial filtering amplifier for high-order harmonics", *Opt. Lett.* **32**, 1498-1500 (2007).
- [96] M. Born and E. Wolf "Principles of Optics", 6th edition, Pergamon Press, 1986.
- [97] J. Ph. Goddet, S. Sebban, J. Gautier, Ph. Zeitoun, C. Valentin, F. Tissandier, T. Marchenko, G. Lambert, M. Ribières, D. Douillet, T. Lefrou, G. Iaquaniello, F. Burgy, G. Maynard, B. Cros, B. Robillard, T. Mocek, J. Nejd, M. Kozlova, and K. Jakubczak "Aberration-free laser beam in the soft x-ray range", *Opt. Lett.* **34**, 2438-2440 (2009).



## Chapter 9. Index

above barrier ionization.....	8	Keldysh theory .....	11
Absolute calibration of XUV camera ...	98	$M^2$ factor .....	72
ADK theory .....	11	$M^2$ of HHG beam.....	72
attosecond .....	4	Maker fringes.....	68
beam profile.....	69	materials surface processing .....	87
Bohr radius.....	7	multilayer optics metrology.....	95
coherence		natural dispersion .....	16
spatial.....	81	nonlinear polarization.....	7, 19
coherence length .....	68	perturbative regime.....	7
confocal parameter.....	17	phase matching factor .....	57
convection currents model .....	94	phase-matching .....	15
cut-off law .....	14	plateau .....	18
extreme ultraviolet .....	4	ponderomotive potential .....	9
femtosecond .....	3	regimes of nonlinear optics .....	11
footprint camera.....	31	relativistic regime .....	9
free electrons dispersion .....	16	resonant absorption .....	24
fringes visibility .....	82	soft X-rays .....	4
Gouy phase shift .....	17	spatial filtering.....	109
HHG		spectrum of high-order harmonics.....	18
amplification of.....	108	Stark effect.....	7
energy .....	85	strong field regime.....	7, 8
gaseous media, in .....	12, 20	three-step model .....	12
molecules, in .....	22	transmission grating spectrometer .....	31
solid targets, from.....	24	tunability of HHG .....	35
two-color .....	101	tunnel ionization .....	8
incubation effect.....	93	two-color HHG .....	101
intermediate regime .....	8	X-ray radiation .....	4
Keldysh parameter.....	9, 35		



## Chapter 10. List of figures

Figure 1.1. Ms. Röntgen's hand. First medical imaging with X-rays (December 22 1895) [2].	3
Figure 1.2. Typical spectrum of high-order harmonic XUV source developed at IoP/PALS (conversion medium: argon).	4
Figure 2.1. Tunnel ionization. The atomic potential affected by the external electric field which the field strength is comparable to the atomic fields. It is plausible that the electrons from the most-outer atomic shell will be unbound. This transition is often referred as Optical Field Ionization (OFI).	8
Figure 2.2. In this case, the applied electric field is even higher than the atomic field strength. The atomic potential barrier is suppressed and electrons from most-outer shells are liberated through above barrier ionization.	8
Figure 2.3. Multiphoton ionization process: $n$ -photons is absorbed. The total energy of absorbed photons ( $n \cdot h\nu$ ; $n$ - number of absorbed photons, $h$ - Planck's constant, $\nu$ - light frequency) exceeds ionization potential.	9
Figure 2.4. Regimes of nonlinear optics.	11
Figure 2.5. Summary of the 3-step model of HHG. The first step is tunnel-ionization of an atom. Next, an electron is driven away from its parent ion in the external electric field of an intense laser pulse. When the oscillating laser field reverses its sign the particle is re-accelerated back towards the atom and, finally, recombines. The last step leads to emission of a photon.	14
Figure 2.6. Dependence of HHG in molecules from the ellipticity and orientation of the molecular axis with the respect to laser polarization orientation. The molecule of interest is $\text{CO}_2$ and curve on the right is a signal yield for 25 <sup>th</sup> harmonic order [39].	22
Figure 2.7. HHG from solid target surface geometry.	24
Figure 3.1. Laser system used for HHG at IoP/PALS.	27
Figure 3.2. Picture showing the table-top femtosecond laser system deployed in the HHG source. The system comprises Micra oscillator and Legend regenerative amplifier pumped by Evolution laser (visible in Figure 3.3).	28

Figure 3.3. Evolution Nd:YVO laser system provides pumping energy at its second harmonic for regenerative amplifier (Legend). The system is controlled using a notebook through two control boxes visible in the upper part of the picture.....	28
Figure 3.4. Schematic experimental drawing of HHG source at the IoP/PALS.....	29
Figure 3.5. HHG experimental beamline at IoP/PALS. The beamline comprises titanium-doped sapphire laser system, HHG source placed in the source vacuum chamber (the blue in the picture) and application chamber (grey in the picture, downstream beam propagation direction).....	30
Figure 3.6. Conceptual design of a gas cell.....	31
Figure 3.7. Picture of the gas cell used in the experiments.....	31
Figure 3.8. Pixelink XUV CMOS camera. ....	31
Figure 3.9. Schematic of the transmission grating spectrometer. ....	32
Figure 3.10. Real photo of TGS (the CCD portal is at the right hand side of the spectrometer in the photo). ....	32
Figure 3.11. Schematic drawing of the SiN <sub>x</sub> grating used in TGS [51]. ....	33
Figure 3.12. SEM image of a the grating. The grating period was 400 nm and the linewidth was 205 nm. The window size (the size of the grating) was 3 x 3 mm [51]......	33
Figure 3.13. TGS calibration software.....	34
Figure 4.1. Geometry of optimization of the position of the gas cell along beam propagation path. "0" position of the motorized stage corresponds to the beam waist location close to entrance to the cell. ....	63
Figure 4.2. Experimental setup of the harmonic beam profile measurements. ....	69
Figure 4.3. High-order harmonic beam profile.....	69
Figure 4.4. 3D beam profile plot.....	70
Figure 4.5. Experimental setup for measurement of M <sup>2</sup> parameter of high-order harmonic beam.....	72
Figure 4.6. XUV beam profile at relative position along beam propagation direction: -12 mm (FWHM size: 281 x 871 μm).....	74
Figure 4.7. XUV beam profile at relative position along beam propagation direction: -9 mm (FWHM size: 288 x 703 μm).....	74

---

Figure 4.8. XUV beam profile at relative position along beam propagation direction: - 5 mm (FWHM size: 100 x 382 $\mu\text{m}$ ).....	74
Figure 4.9. XUV beam profile at relative position along beam propagation direction: - 2 mm (FWHM size: 34 x 221 $\mu\text{m}$ ).....	74
Figure 4.10. XUV beam profile at relative position along beam propagation direction: - 1 mm (FWHM size: 27 x 161 $\mu\text{m}$ ). Sagittal focus position. ....	75
Figure 4.11. XUV beam profile at relative position along beam propagation direction: 0 mm (FWHM size: 40 x 154 $\mu\text{m}$ ).....	75
Figure 4.12. XUV beam profile at relative position along beam propagation direction: +2 mm (FWHM size: 67 x 141 $\mu\text{m}$ ).....	75
Figure 4.13. XUV beam profile at relative position along beam propagation direction: +4 mm (FWHM size: 107 x 147 $\mu\text{m}$ ).....	75
Figure 4.14. XUV beam profile at relative position along beam propagation direction: +6 mm (FWHM size: 194 x 201 $\mu\text{m}$ ).....	76
Figure 4.15. XUV beam profile at relative position along beam propagation direction: +9 mm. Visible artifact is probably due to a parasitic reflection (FWHM size: 395 x 415 $\mu\text{m}$ ). ....	76
Figure 4.16. Simulation of focal spot of XUV beam focused by a spherical mirror in the exactly same setup as in the experiment. The observation plane is at distance of 280 mm from the mirror (reference to Figure 4.11).....	79
Figure 4.17. Simulation of the circle of least confusion which, in the setup, is located ~269 mm from the focusing mirror. Note difference in scale bar between the both figures. ....	79
Figure 4.18. Scheme of the slits used in the experiment [64]. ....	81
Figure 4.19. Experimental setup for measurement of spatial coherence of high-order harmonic beam. ....	81
Figure 4.20. Andor DX440-DN quantum efficiency curve [52]. ....	85
Figure 4.21. Experimental setup for estimation of absolute signal of high-order harmonic beam. ....	86

Figure 5.1. Schematic of the experimental setup for surface modification by dual action of XUV and Vis-NIR ultrashort pulses. Experiment was performed at Korean Advanced Institute of Science and Technology (KAIST). .....	88
Figure 5.2. Picture of the experimental setup. ....	89
Figure 5.3. AFM images of the PMMA surface simultaneously irradiated with XUV and Vis-NIR ultrashort pulses. Experiment performed at KAIST. ....	91
Figure 5.4. Images from Nomarski microscope of PMMA sample exposed to a single shot of (a) NIR-VIS radiation only, and (b) mixed field of XUV/NIR-VIS. Insets show the corresponding AFM images of details. ....	92
Figure 5.5. Nomarski microscope images of a-C sample exposed to 10 shots of (a) NIR-VIS beam only, and (b) XUV/NIR-VIS. Insets present corresponding AFM scans of details. ...	93
Figure 5.6. Convection currents model. A thin layer of bulk material is molten (thickness $\sim$ tens of nm) after irradiation by femtosecond NIR laser. When the molten material is subject to interference pattern (upper part of the Figure), spatial modulation of pressure will be established leading to creation of local pressure gradients. In areas where pressure is higher, the "hotter" liquid will expand by means of convection currents (along the pressure gradient). ....	94
Figure 5.7. Experimental setup of measurement of reflectivity of multilayer mirror versus incidence angle. Experiment was performed at KAIST. ....	95
Figure 5.8. Photo of the experimental setup. ....	95
Figure 6.1. Comparison of the two-color HHG yield with 'standard' setup. Experimental conditions were: circular gas jet, He, 950 Torr ( $\sim$ 1.27 bar), laser pulse energy: 2.8 mJ, pulse duration 28 fs, beam size 10 mm, BBO 10 $\mu$ m thick (conv. eff. $\sim$ 20 %), filtering: 1.5 $\mu$ m Al for 2-color case, 0.4 $\mu$ m Al for 1-color case [90]. ....	102
Figure 6.2. Two-color HHG setup. Experiment performed at KAIST. ....	102
Figure 6.3. Picture of the experimental setup. BBO crystal (not visible in the picture) was placed after second relay mirror downstream and before the gas puff. ....	103
Figure 6.4. Examination of the phase influence between the two fields onto 38th harmonic yield. The two BBO crystals were used for SH generation. ....	104
Figure 6.5. Optimization of gas jet length a) and HHG spectrum for optimized 6 mm jet length b). ....	104

---

Figure 6.6. HHG in two-color scheme at IoP/PALS. ....	105
Figure 6.7. Spectra of HHG using only fundamental femtosecond laser field a) and in two-color scheme b). ....	106
Figure 6.8. HHG amplification in OFI laser plasma amplifier. a) is harmonic seed, b) is ASE of SXRL only, c) is seeded SXRL with detuned timing between amplifier formation pulse and seed arrival, d) time-optimized seeded SXRL [93]. ....	109
Figure 6.9. HHG-seeded SXRL experimental setup providing improved XUV beam quality [94]. Experiment performed at Laboratoire d'Optique Appliquée.....	110
Figure 6.10. Improvement of HHG beam seeded into SXRL OFI laser plasma amplifier [95]. ....	111



## Chapter 11. List of graphs

Graph 4.1. Tunability of HHG.....	37
Graph 4.2. Optimization of chirp of NIR laser pulse.....	37
Graph 4.3. Tunability of HHG.....	38
Graph 4.4. Optimization of chirp of NIR laser pulse.....	38
Graph 4.5. Tunability of HHG.....	39
Graph 4.6. Optimization of chirp of NIR laser pulse.....	39
Graph 4.7. Tunability of HHG.....	40
Graph 4.8. Optimization of chirp of NIR laser pulse.....	40
Graph 4.9. Tunability of HHG.....	41
Graph 4.10. Optimization of chirp of NIR laser pulse.....	41
Graph 4.11. Tunability of HHG.....	42
Graph 4.12. Optimization of chirp of NIR laser pulse.....	42
Graph 4.13. Tunability of HHG.....	43
Graph 4.14. Optimization of chirp of NIR laser pulse.....	43
Graph 4.15. Tunability of HHG.....	44
Graph 4.16. Optimization of chirp of NIR laser pulse.....	44
Graph 4.17. Tunability of HHG.....	45
Graph 4.18. Optimization of chirp of NIR laser pulse.....	45
Graph 4.19. Tunability of HHG.....	46
Graph 4.20. Optimization of chirp of NIR laser pulse.....	46
Graph 4.21. Tunability of HHG.....	47
Graph 4.22. Optimization of chirp of NIR laser pulse.....	47
Graph 4.23. Intensity drop during wavelength tuning of 27 <sup>th</sup> harmonic order.....	48
Graph 4.24. Optimization of NIR beam size.....	50
Graph 4.25. Optimization of NIR beam size.....	50
Graph 4.26. Optimization of NIR beam size.....	51
Graph 4.27. Optimization of NIR beam size.....	51
Graph 4.28. Optimization of NIR beam size.....	52

---

Graph 4.29. Optimization of NIR beam size.....	52
Graph 4.30. Optimization of NIR beam size.....	53
Graph 4.31. Optimization of NIR beam size.....	53
Graph 4.32. Optimization of NIR beam size.....	54
Graph 4.33. Optimization of the focal length of the lens in the HHG setup. The optimization has been performed for 27 <sup>th</sup> harmonic order.....	55
Graph 4.34. Optimization of gas cell length (f=750 mm). ....	56
Graph 4.35. Optimization of gas cell length (f=1000 mm). ....	56
Graph 4.36. Optimization of gas pressure (Ar).....	58
Graph 4.37. Optimization of gas pressure (Ar).....	58
Graph 4.38. Optimization of gas pressure (Ar).....	59
Graph 4.39. Optimization of gas pressure (Ar).....	59
Graph 4.40. Optimization of gas pressure (Ar).....	60
Graph 4.41. Optimization of gas pressure (Ar).....	60
Graph 4.42. Optimization of gas pressure (Ar).....	61
Graph 4.43. Optimization of gas pressure (Ar).....	61
Graph 4.44. Optimization of gas pressure (Ar).....	62
Graph 4.45. Optimization of gas pressure (Ar).....	62
Graph 4.46. Optimization of longitudinal gas cell position. ....	64
Graph 4.47. Optimization of longitudinal gas cell position. ....	64
Graph 4.48. Optimization of longitudinal gas cell position. ....	65
Graph 4.49. Optimization of longitudinal gas cell position. ....	65
Graph 4.50. Optimization of longitudinal gas cell position. ....	66
Graph 4.51. Optimization of longitudinal gas cell position. ....	66
Graph 4.52. Optimization of longitudinal gas cell position. ....	67
Graph 4.53. Optimization of longitudinal gas cell position. ....	67
Graph 4.54. Optimization of longitudinal gas cell position. ....	68
Graph 4.55. Harmonic beam profile in the horizontal direction together with its Gaussian fit. The beam width (FWHM) is 2.86 mm. ....	71
Graph 4.56. Harmonic beam profile in the vertical direction together with its Gaussian fit. The beam width (FWHM) is 2.49 mm. ....	71

---

Graph 4.57. Simulated reflectivity of the multilayer mirror used in the experiment [61]. .....	73
Graph 4.58. The caustics scan of the focused HHG beam. The distance between tangential and sagittal foci was $\sim 3.495$ mm. ....	77
Graph 4.59. Eccentricity of the XUV beam due to focusing by spherical mirror.....	78
Graph 4.60. Interference fringes in double-slit Young's experiment. Single slit case (diffraction on a slit).....	83
Graph 4.61. Interference fringes from two slits $50 \mu\text{m}$ apart. ....	83
Graph 4.62. Interference fringes from two slits $100 \mu\text{m}$ away from one another.....	83
Graph 4.63. Interference fringes from slits $150 \mu\text{m}$ distant.....	83
Graph 4.64. Interference fringes from slits spaced by $200 \mu\text{m}$ . ....	83
Graph 4.65. Interference pattern from $250 \mu\text{m}$ -distant slits. ....	83
Graph 4.66. Interference fringes using $300 \mu\text{m}$ away from each other. ....	84
Graph 4.67. Interference pattern from $400 \mu\text{m}$ distant slits.....	84
Graph 4.68. Interference fringes visibility as a function of distance between the pair of slits. ....	84
Graph 5.1. Calibration curve of AXUV-100 Al photodiode (International Radiation Detectors Inc.) .....	96
Graph 5.2. Reflectivity measurement of Mo/Si flat multilayer mirror designed for $21.6 \text{ nm}$ radiation incident at $45^\circ$ angle. ....	97
Graph 5.3. Pixelink CMOS camera calibration curve. The estimated QE takes into account QE of CMOS chip as well as of phosphor layer (P43) deposited onto the chip for radiation conversion.....	98
Graph 6.1. Comparison of single-color and two-color HHG. The occurrence of even harmonic orders is clearly visible.....	106



---

## Chapter 12. List of tables

Table 4.1. Estimation of the experimental conditions in the interaction region. ....35